Protoclusters of Galaxies in Cosmological Zoom Simulations

Elena Hernández Martínez

München 2021

Proto-Galaxienhaufen in Kosmologischen Zoom-Simulationen

Elena Hernández Martínez

Masterarbeit
an der Facultät für Physik
der Ludwig–Maximilians–Universität
München

vorgelegt von
Elena Hernández Martínez
aus Bilbao, Spain

Betreut von
Dr. Rhea-Silvia Remus
PD Dr. Klaus Dolag

München, den 02.11.2021

Contents

List of Figures

List of Tables

Abstract

From individual galaxies to the largest megaclusters, the universe today shows a very rich structure at all scales. However, observations of the earliest stages of the Universe show that it was much smoother than it is now. As a result, understanding the evolution of large-scale structures like dark matter haloes and clusters of galaxies is of great interest for modern cosmologists and astrophysicists. In particular, protoclusters of galaxies are an active line of research as their study can provide us with key insights into cosmological star formation, galaxy formation and evolution and the working principle of the most energetic processes in the Universe, like cosmic rays, SN explosions and AGN feedback.

As a consequence of the ever-increasing computational power available to researchers, the last few decades have seen hydrodynamical simulations emerge as an essential tool for understanding the physical processes that influence the evolution of protoclusters. Scientific consensus has emerged around the influence of baryonic processes in protocluster evolution. Still, many questions remain open about the exact way and the extent to which energetic processes, like star formation, stellar feedback and AGN feedback, influence the evolution of galaxies and galaxy clusters; and thus, also about the correct implementation of these processes in the subgrid physics prescriptions of hydrodynamical cosmological simulations.

In this work, we start by discussing the main search techniques and the characteristic properties of protoclusters in observations, followed by a detailed overview of the current state-of-the-art techniques for numerical simulation, including baryonic processes, such as star formation, stellar evolution, SN driven winds, BH growth and AGN feedback. We then present a new set of hydrodynamical cosmological zoom simulations, called Compass, which contains 24 Lagrangian regions, resulting in 73 massive clusters, 24 having final masses $M_{vir} \geq 10^{15}\mathrm{M}_{\odot}$ and 49 clusters with final masses $M_{vir} \geq 10^{14}\mathrm{M}_{\odot}$.

We run the complete sample with a simple subgrid model that has prescriptions for star-formation, simple cooling and a simple stellar feedback in the form of SN driven winds. We study the different types of morphologies and formation histories of our clusters, as well as the correlation between their total masses, stellar masses, SFRs and substructure content at high and low redshifts. By doing this we are able to show that, contrary to the common belief, the high redshift total protocluster mass is not a good proxy of final

cluster masses.

In order to better comprehend the effects of SN feedback and AGN feedback on our protocluster sample, we choose the Lagrangian region g1212639 and rerun it twice. The first time we run it with a more complete prescription of stellar evolution, including metals, AGB yields and SN type Ia and II. In the second run we add a prescription for BH seeding, growth and AGN feedback. By doing this we find that AGN feedback had a strong effect in the gas dynamics inside the cluster, heating it and quenching star formation earlier than in the rest of the runs. However, even if the AGN run performs better in reproducing observations of SFRs and baryon fraction masses at $z \sim 0$, the stellar fraction and cold fractions remain too high for our clusters at the high mass end. Although, the final stellar masses of our clusters and cluster galaxies are in concordance with observations, the high redshift ($z \sim 4$) SFR profiles are for the three runs lower than the ones observed for the protocluster SPT2349-56, without any obvious improvement in the AGN run. Based on our work we end with a discussion of the possible sources of this disagreement and we propose some possible future studies that could help unravelling the origin of this discrepancy.

Chapter 1

Introduction

Galaxy clusters are the largest and most massive virialized objects in the Universe and thus a fundamental part of the cosmological large-scale structure (LSS). Given their deep potential wells, the high number of galaxies they contain, approximately 10^2 to 10^3 (see Sarazin, 1988), and their large extensions of a few Mpc, these structures are an ideal transition between cosmological and galactic scales. Therefore, the study of galaxy clusters is vital for the development of pivotal topics in astrophysics and cosmology like galaxy formation models, or the tracing of the formation of massive dark matter halos and super massive black holes (SMBHs) (e.g., Springel et al., 2005b; De Lucia, 2007).

The importance of galaxy clusters transfers also to their high redshift progenitors, called protoclusters. These are featured in many discussions related to cosmological models, dark matter models and structure formation scenarios (see Zwicky, 1939; Sunyaev and Zeldovich, 1972; Press and Schechter, 1974; White and Rees, 1978; Efstathiou and Eastwood, 1981; Davis et al., 1985; Pizzuti et al., 2020). However, the exact definition of a protocluster is far from trivial and an important matter of debate. This will be discussed in detail in section 1.2 of this work.

The evolution of protoclusters is a phenomenon that involves processes at many different scales. While on cosmological scales the growth of perturbations is driven by the effects of gravity on the dark matter component, when we look into galactic scales, we find also many other gas dynamical and astrophysical effects in addition to gravity. Particularly, the hot intra-cluster medium (ICM) harbors many fascinating dynamical processes that interconnect gravity with baryonic physics. Some of them are gravitational shock waves, gas radiative cooling, star formation (SF), feedback from supernovae (SNe) , gas accretion onto SMBHs and their associated feedback, gas turbulence, ram–pressure stripping of galaxies, thermal conduction processes, energetic inputs associated to the populations of cosmic ray (CR) electrons and protons, and many more.

However, even if we know that these processes take place inside protoclusters, we do not know precisely to what extent they influence the formation and evolution of galaxies and

the final cluster itself. Phenomena like, SNe and AGN feedback are expected to leave an imprint in the star formation rates, the stellar to halo mass relations, the baryon, gas and stellar fractions and many more important quantities in clusters. Throughout this work, we will study the effect of these processes in cluster quantities like the ones mentioned before, using cosmological simulations with different subgrid physics. Our final objective will be understanding better the influence of these processes in structure evolution in the protocluster and cluster regime. Moreover, we will also consider what improvements may be needed in our simulated models in order to reproduce observations better.

Before we embark in this study, we will first navigate briefly through the current understanding of structure formation and evolution. Chapter 1 touches the topics of to the evolution of Large-Scale-Structure (LSS) from primordial fluctuations, the definition of a cluster and a protocluster, observations of such structures and their importance in astrophysical and cosmological scales. In chapter 2 we present the state-of-the-art techniques for numerical simulation, including prescriptions for baryonic physics in unresolved scales. Here, we also present our cosmological hydrodynamical zoom simulations set, Compass. In chapter 3, we carry out a study of the formation and evolution of our cluster sample. Moreover, we analyze the effects of stellar evolution, SN feedback, BH growth and AGN feedback on protocluster properties. Finally, we conclude this work in chapter 4, by summarising and discussing our most outstanding results.

1.1 General Theory of Structure Formation

In the current scenario of structure formation within the spatially flat Λ-Cold Dark Mater model (ΛCDM; Blumenthal et al., 1984) with cosmological constant, all objects are originated hierarchically from small instabilities in the initial primordial density field. These initial perturbations or overdensities grow many orders of magnitude in an expanding Universe, first increasing in size as they expand with the rest of the Universe, then contracting due to the effect of gravity and finally virializing. We characterize these overdensities by means of the density contrast $\delta(\mathbf{x}) = (\rho(\mathbf{x}) - \overline{\rho})/\overline{\rho}$, where $\overline{\rho}$ is the mean mass of the Universe.

The primordial properties of this field are determined during the inflationary epoch. In general, inflationary models predict an homogeneous and isotropic Gaussian random fluctuation field (e.g. Guth and Pi, 1982). This proposal appears to be confirmed by observed fluctuations in the electromagnetic radiation remnant from the decoupling of photons in an early stage of the Universe, the Cosmic Microwave Background (CMB; e.g. Planck Collaboration et al., 2014). On the other side, predictions coming from N-body simulations (e.g. Klypin and Shandarin, 1983) have confirmed that the growth of these perturbations gives rise to the formation of a complex network of cosmic structures interconnected along walls and filaments, as we see in figure 1.1.

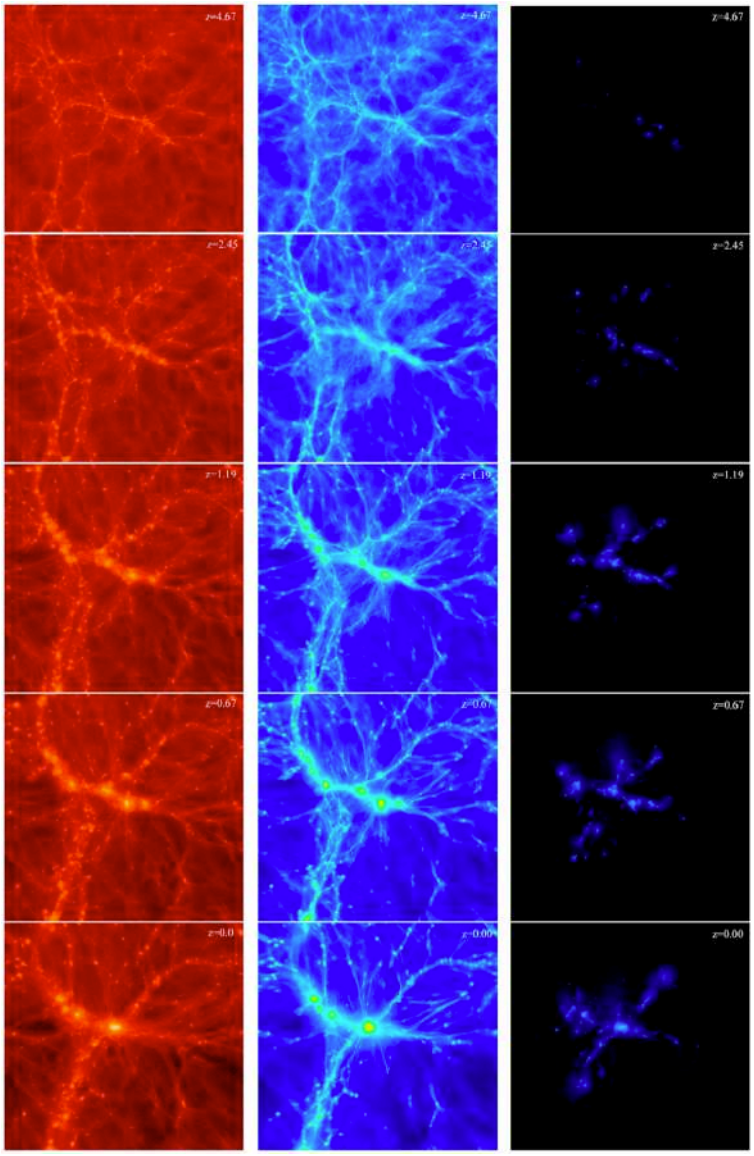

Figure 1.1: Formation and evolution of galaxy clusters viewed in a cosmological hydrodynamical simulation. Left,central and right columns show, respectively, the evolution of the dark matter, gas and stellar densities from $z \approx 4$ (top panels) until z = 0 (bottom panels). At $z = 0$, the biggest cluster formed has a virial mass of $\approx 10^{15}\mathrm{M}_{\odot}$ and a radius of $\sim$ 3Mpc. The simulation was performed with the Eulerian AMR cosmological code MASCLET (Quilis, 2004). Each panel is 64 co-moving Mpc length per edge and 5 comoving Mpc depth (Planelles et al., 2014)

.

The first structures in the Universe are expected to form at $z \sim 10 - 30$ in dark matter (DM) halos of $10^5 - 10^8 M_{\odot}$ (Tegmark et al., 1997; Barkana and Loeb, 2001; Bromm et al., 2002). These low mass halos are usually called minihalos and are assumed to harbor the

first primordial stars in the Universe. In the hierarchical context of structure evolution these minihalos are the first blocks upon subsequent structures will be built. Through continuous accretion and mergers of these smaller halos, we end up with a cosmic hierarchy in terms of mass and formation time. On the one side, we have the first galaxies in the early Universe and on the other side the most massive galaxy clusters that we find at present day (e.g. Somerville et al., 2012).

The highly non-linear processes that lead to structure formation generated turbulence during collapse at a wide range of scales, affected cooling as well as several feedback processes inside galaxies and clusters, thus making the study of these object extremely complex and multidisciplinary (Silk and Mamon, 2012, for a review on galaxy formation theory). Indeed, approaching the growth of density perturbations into cosmological size structures is a colossal task due to the high number of processes involved and their inherent complexities. However, this problem could be tackled first using some assumptions that may simplify it enough to work it out analytically. Hopefully, this will provide an idea of what the true solution to the problem is in all its magnitude. The most simple and commonly used route to understand the development of structures in an analytical way is the so called top-hat collapse model. An overview of this method will be presented in the following section.

1.1.1 The Spherical Top-Hat Collapse Model

The simplest case in which the non-linear evolution of collapsing structures can be precisely calculated is the one addressed by the simple spherically symmetric collapse model (e.g. Gunn and Gott III, 1972; Bertschinger, 1985). This model resolves the evolution of a spherical density perturbation of radius R that evolves under the effects of gravity into a virialized halo.

To exemplify the working principle of this model lets consider that we are dealing with a background Universe described by the Einstein de Sitter (EdS) model ($\Omega_m = 1$ and $\Omega_\Lambda = 0$; Einstein and De Sitter, 1932). Now, we assume that we have a spherical perturbation of radius $R(t)$, which behaves in the same as the expansion factor. In the initial stages, the spherical perturbation has a constant overdensity and, as it is expanding with the background Universe, the velocity at the border is zero. The density of the perturbation can be expressed in terms of the background Universe as $\Omega_p = \Omega(t_i)(a + \delta_i)$. The perturbation will grow until it reaches its maximum expansion at a given turn-around time t_{ta} and radius R_{ta}. It is at this exact moment that gravity dominates over the the spherical perturbation, so that it stops expanding with the background Universe, i.e. it detaches from the expansion of the background, and initiates the collapse.

Given the spherical symmetry that we imposed in our model, the collapse of such perturbation is a one-dimensional problem and is fully specified by the top-hat radius

$R(t)$. Once the perturbation is detached from the background Universe we can treat it as an isolated "pseudo-universe" with spherical geometry, meaning that we can describe the perturbation as a Friedmann–Lemaître–Robertson–Walker (FLRW) universe using the Friedmann's equation of cosmology (Lahav et al., 1991). After a given time t_{vir} of collapse, the overdensity reaches an equilibrium state, at which the virial condition $U = -2K$, where U is the potential and K the kinetic energy, is fulfilled. At this moment, the formation process of the overdensity is finished, the collapse of matter has come to an end and the halo is virialized.

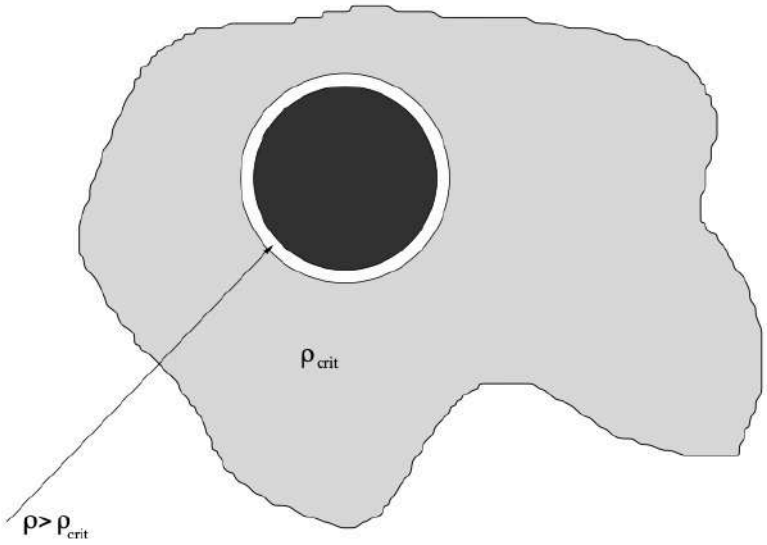

Figure 1.2: Schematic representation of a spherical overdensity decoupled from the background universe.

1.1.2 Non-linear Evolution of Real Overdensities

The spherical collapse model explored in the previous section provides a useful guideline for the approximate time scale of halo collapse and has proven to be useful in statistical models for the study of formation and evolution of halo populations. This simple model and its extensions (e.g., ellipsoidal collapse model) do unfortunately miss many important details of the collapse of real overdensity peaks. Such complexities can only be explored using three-dimensional numerical cosmological simulations (Bertschinger, 1998; Dolag et al., 2008; Norman, 2010; Borgani and Kravtsov, 2011a).

As an example the left sequence of images in figure 1.1 shows the evolution of the DM density field from $z = 4.67$ to $z = 0$. The overall picture is far from an spherical top-hat collapse. At early epochs, collapsed objects with low masses populate the proto-cluster region. As the evolution proceeds, these objects merge into larger structures that will

accrete matter from the filaments in the surroundings. Thus, the collapse departs severely from spherical symmetry and constant density edges. Rather, we encounter a filamentary matter accretion, and small overdensities within larger overdense collapsing regions.

Due to the fact that different overdense regions have also different spatial extensions and time evolutions, the collapse of a cluster-scale overdensity is a processes that does not have a single collapse epoch but is prolonged in time and embedded in merging processes. Indeed, the peaks in the density field are not isolated, but are surrounded by other peaks. These will suffer tidal forces from their density peak neighbours forming a filamentary web that connects them, establishing a preferable matter accretion direction (Bond et al., 1996; Pogosyan et al., 1998).

Besides, the density distribution within the peaks in the actual density field is not smooth, as in the smoothed field $\delta_R(x)$ of the spherical collapse model, but contains fluctuations on all scales. As a consequence, we encounter merging events and interactions between overdensities at different scales, leading to energy exchange, relaxation processes, and an important matter redistribution within the considered regions. Thus, the distribution of matter around the collapsed peak can smoothly extend to several virial radii for late epochs and small masses (Prada et al., 2006; Cuesta et al., 2008). This hinders a clear definition of halo boundaries and total masses and results in a variety of mass definitions adopted in practice, as we will discuss in the next section.

1.2 What is a (Proto)cluster of Galaxies?

The study of clusters and protocluster of galaxies has been plagued by the fact that those terms are used differently in different studies. The term "cluster" is reserved by many authors for the most virialized systems with masses around $10^{14} M_\odot$, while systems over $10^{13} M_\odot$ are referred just as "groups". In reality this distinction is rather arbitrary as there is no profound physical distinction between both types of structures. Thus, other studies refer to both equally as "group" or "cluster".

Even more relevant is the concept of *virialization* in galaxy clusters. The virialized state of galaxy clusters is an approximation used in order to extract data from observations. The possible missleading effects of this approximation are still a matter of debate. The truth is that clusters are structures in continuous evolution, where merging events and shocks happen even at the lower redshifts. A good example of how virialization is an approximation for galaxy clusters, are the core regions of some of our nearby clusters, like Virgo (Ferrarese et al., 2020) and Coma (Bonafede et al., 2021). The first one contains a chain of galaxies falling into the center of the cluster potential well, showing that even at low redshifts, matter is still infalling and collapsing (see figure 1.3a). The Coma cluster contains two BCGs in its center, which are expected to merge in the future (see figure 1.3b).

In this work we will follow the popular convention that clusters are virialized objects with masses around $10^{14} M_{\odot}$ or higher (e.g., see Bower et al., 2004), but without forgetting that their virialization is in reality true only as a first order approximation. Adopting this definition of a cluster, the term "protocluster" is from a semantics straightforward: a protocluster is a structure that will eventually collapse and form a virialized object of $10^{14} M_{\odot}$ or higher.

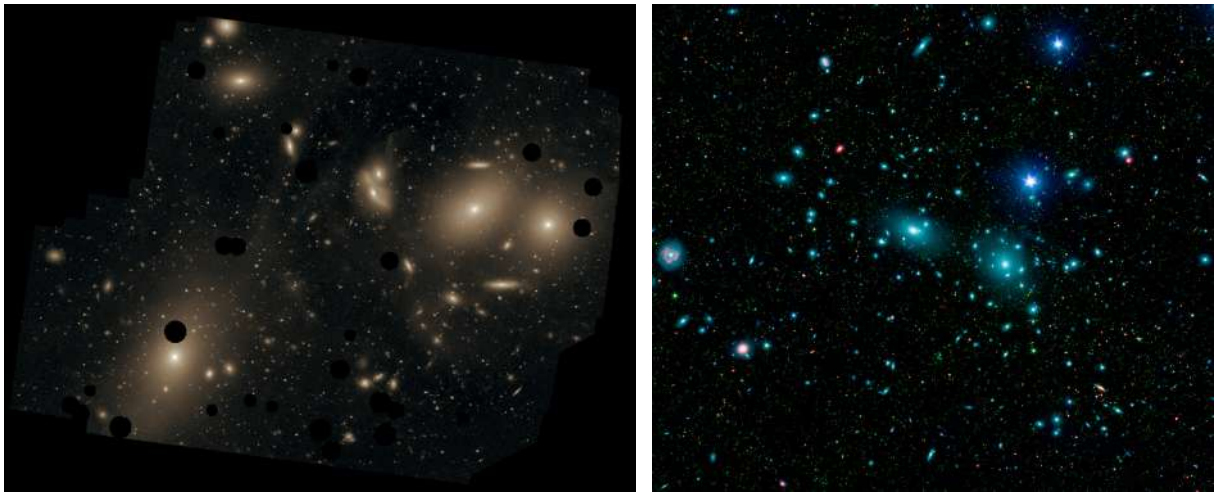

Figure 1.3: Left: Optical image of the central region of the Virgo cluster taken by the Palomar Observatory on Mount Palomar in California (Credit: NASA, ESA, and the Digitized Sky Survey; acknowledgment: Z. Levay (STScI) and D. De Martin (ESA/Hubble)). Right: Coma cluster observation performed with the Spitzer Space Telescope in long-wavelength infrared (red), short-wavelength infrared (green), and visible light. The many faint green smudges are dwarf galaxies in the cluster (Credit: NASA/JPL-Caltech/L. Jenkins (GSFC)).

Even if that definition seems very simple, other definitions could be as valid. For example, if we call a massive high redshift structure a cluster only when it meets a set of conditions typical of clusters, like detection of thermal ICM in the X-rays or a well-defined cluster red sequence, then a protocluster would be any massive structure that does not meet these requirements yet. Other definitions could be constructed based on the redshift at which half of the present-day mass of a cluster is assembled, or on the redshift where environmental effects from a dense gaseous medium or galaxy interactions, like ram-pressure stripping, dynamical friction or quenching, begin to alter significantly the properties of the infalling and orbiting cluster galaxies.

A big advantage of using the first definition that we proposed first, is that the combined space number density of clusters and protoclusters is, at any redshift, equal to the abundance of clusters today. This definition turns out to be very useful in simulations, as we can track back any galaxy cluster from redshift 0 to the protocluster stage at higher redshifts.

We should keep in mind that strict definitions of what a protocluster is, are truly valid only in theory and simulations. When it comes to observations, it is difficult to decide with certainty if what we are observing is indeed a protocluster. As the areas covered by protoclusters are of the orders of tens of Mpc, observations usually are only able to capture the cores of such structures. Thus, in order to classify an object in the sky as a protocluster, observational information about the object itself is insufficient, we also need information about its descendant at present day. The latter is a serious challenge that cannot be done on an object-by-object bases but only statistically.

For lower redshift galaxy clusters the situation is less difficult, as there is a larger variety of data that can be extracted from observations and used for their identification: the presence of the cluster red sequence, gravitational lensing mass profiles, the velocity dispersion of the galaxies, or the X-ray or the Sunyaev–Zel'dovich (SZ) effect. These measurements usually provide constrains which are accurate enough to infer the system mass and evolutionary stage.

When it comes to observations, authors usually refer to a protocluster candidate as a structure that is overdense enough compared to its surroundings such that it can be recognized observationally. In principle, this definition is reasonably compatible with the definition that we proposed above for all cluster progenitors. Nevertheless, as observations only detect the cores of protoclusters, they are prone to miss structures with less developed cores. The number of protoclusters with non-developed cores is expected to increase with redshift, making high redshift detections more difficult. Thus, it is highly probable that for every cluster detected, there are many others with a lower density contrast, that have not been detected.

In reality, cluster formation is a process that is taking place at all redshifts. Many 'virialized' clusters are surrounded by other material that will eventually fall or merge, becoming part of the cluster (Chiang et al., 2013; Muldrew et al., 2015). Thus, we could argue that the cluster encompasses a much larger region that includes the entire structure, i.e. also the part that has yet to fall into the cluster. However, we will leave this subtlety aside and follow the current literature convention calling a collapsed object of $10^{14} M_{\odot}$ a cluster and call structures where that massive core is not yet present a protocluster.

1.3 Protoclusters as Laboratories for Cosmology and Astrophysics

The relevance of clusters and protoclusters of galaxies in cosmology and astrophysics dates back to the 1920s, when Edwin Hubble proved that spiral and elliptical nebulae were bona-fide galaxies like the Milky Way but located at large distances form us (Hubble, 1925, 1926). This implied that clusters of galaxies where systems of immense size. A decade later, thanks to measurements of galaxy velocities in regions of clusters and by assuming virial equilibrium, it was discovered that the total gravitating cluster masses for the Coma (Zwicky, 1933, 1937) and Virgo clusters (Smith, 1936) were so high that exceeded the combined mass of all stars in clusters by factors of 200 - 400. This fact encouraged the postulation of large amounts of "dark matter". After decades of debate dark matter was finally confirmed by the discovery of the hot plasma in clusters, the ICM, emitting at X–ray energies. Measurements of the hot plasma temperature provided confirmation that the depth of the gravitational potential of clusters could only be explained by the existence of an additional non radiative component (Cavaliere et al., 1971; Forman et al., 1972; Gursky et al., 1971; Meekins et al., 1971).

A good example of how clusters of galaxies are a pillar in the discovery and the consecutive study of dark matter is given by the bullet cluster (see figure 1.4). The bullet cluster is in reality composed of a pair of colliding clusters of galaxies. The major components of the cluster pair, which are stars, gas and the dark matter, behave differently during collision, allowing us to study them separately. The stars, observable in visible light, where not greatly affected by the collision and passed through only slightly slowed down by gravitation. The hot gas of the two colliding clusters (colored in red) was detected by its X-ray emission. Different to the stars, the gas interacts electromagnetically causing shocks and a drag that makes it slow much more than the rest of the components. Meanwhile, DM (detected with gravitational lensing of the background objects and colored in blue) does not feel this drag and thus bypassed the gas region during collision. Studies of the bullet cluster-pair provide one of the best evidence to date for the existence of dark matter. And even more, simulations of the bullet cluster have been used to discard ideas about the nature of dark matter and some versions of Modified Newtonian Dynamics (MOND; Robertson et al., 2016).

The level of evolution of large scale structures like galaxy clusters detected observationally provides significant constrains on cosmological models and parameters. If our Universe would be a flat matter-dominated Einstein-de-Sitter universe, cosmic expansion and gravitational instability would proceed at the same rate. However, in a universe with $\Omega_m < 1$ as ours, there is an epoch, when the cosmological constant begins to be significant and the cosmic expansion progresses faster than gravitational collapse, quenching structure collapse at lower redshifts (e.g. Borgani and Guzzo, 2001).

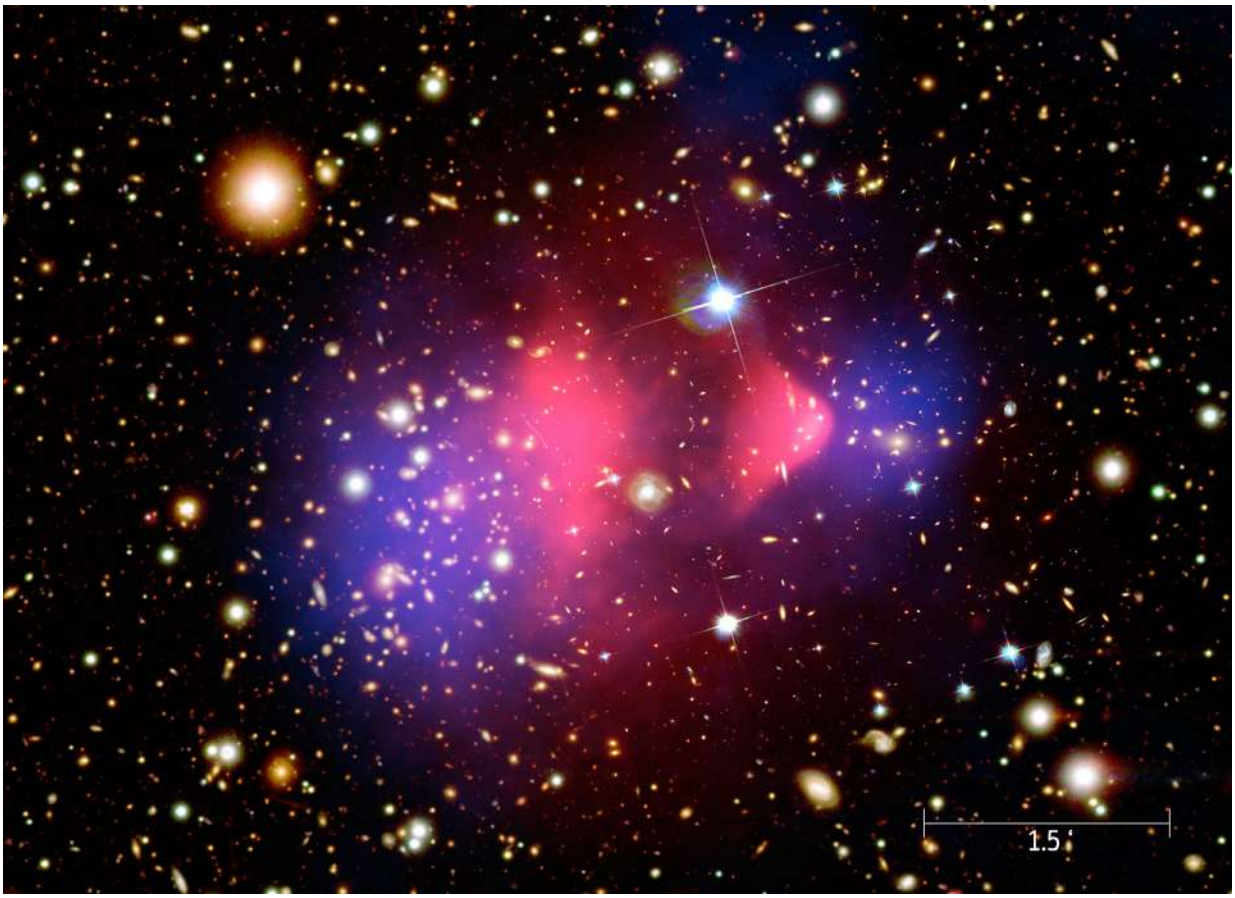

Figure 1.4: Composite image of the galaxy cluster 1E 0657-56, fondly known as the "bullet cluster". The optical image from the Magellan and the Hubble Space Telescope shows galaxies in orange and white in the background (credit: NASA/STScI; Magellan/U.Arizona/D.Clowe et al.) . Hot gas, which contains the bulk of the normal matter in the cluster, is shown by the Chandra X-ray image, which shows the hot intracluster gas (pink; credit: NASA/CXC/CfA/ M.Markevitch et al.). Gravitational lensing reveals the dark matter (blue; credit: NASA/STScI; ESO WFI; Magellan/U.Arizona/ D.Clowe et al.), which represents the dominant mass component of the structure.

(Proto)clusters of galaxies are also the perfect place to study some of the most energetic phenomena in out Universe. A complete representation of the formation of clusters of galaxies needs the inclusion of an accurate description of the dissipative baryon physics. Inside clusters the gas is heated to high temperatures due to shocks and adiabatic compression occurring throughout the collapse. At some point, the gas reaches hydrostatic equilibrium inside the cluster gravitational potential well, it gets dense and cools. This process invigorates star formation and the accretion of matter onto SMBHs, which in turn results in a boost of SN feedback and AGN feedback, which inject heat into the hot plasma component spreading heavy elements through the cluster. Thus, galaxy clusters are the

perfect laboratory to study the formation of stars, the evolution of massive black holes and the spread of heavy elements though the cosmos.

Certainly, galaxy clusters and protoclusters are genuine crossroads of astrophysics and cosmology. Thus, it comes as no surprise that the evolution of protoclusters and clusters of galaxies has become a paramount research area in both fields over the past decades.

1.4 The Interior of Galaxy (Proto)clusters

1.4.1 Galaxy Evolution in Protoclusters

It is well established that galaxies do not evolve as isolated systems but are influenced significantly by the environment they grow in, meaning that galaxies growing in dense environments may diverge from those galaxies growing in less dense regions of the Universe. For example, galaxies growing in dense and gas-rich regions like protoclusters, are expected to form earlier than those in the field and to suffer more mergers that stimulate star formation and AGN activity, which affect galactic morphology and kinematics, enhancing outflow patterns of warm gas and redistributing metals on large scales (Gottlöber et al., 2001; Thomas et al., 2005; Fakhouri and Ma, 2009).

Among the galaxies residing inside clusters there is one type which is particularly remarkable, the Brightest Cluster Galaxies (BCGs). These galaxies reside close to the center of the cluster and their mass is tightly related to the cluster mass, being more massive in clusters with higher masses. BCGs have several structural and chemical properties that distinguishes them from other cluster galaxies and galaxies in the field. For example, having evolved in a dense environment they are known to accumulate a high percentage of their mass through mergers, so that they often contain secondary nuclei (Tonry, 1987). Thus, BCG formation in protoclusters is though to be accompanied by high merging rates, high star formation rates and abundant AGN activity enhanced by merging events (Von Der Linden et al., 2007; Best et al., 2007). High redshift radio galaxies found in protocluster regions have many properties that suggest them as progenitors of local BCGs (Best et al., 2007; Zirm et al., 2005; Hatch et al., 2009; Overzier et al., 2009; Collet et al., 2015)

While the contribution of clusters of galaxies to the present cosmic star formation rate in the local universe is very low (Madau and Dickinson, 2014), the contribution of protoclusters might represent up to $\sim 25\%$ at $z \sim 4$ and $\sim 50\%$ at $z \sim 10$. Dusty Star Forming Galaxies (DSFG) residing in protocluster regions contribute in a high percentage to this total SFR. They represent the most intense starburst in the Universe with infrared luminosities of $10^{13} L_{\odot}$, implying SFRs of thousands of solar masses per year (Casey et al., 2014). Moreover, the fraction of cosmic volume occupied by protoclusters is three times higher at $z \sim 7$ than it is for clusters at $z \sim 0$ (Oteo et al., 2018). The central role of BCGs and DSFGs in protoclusters makes the comparative study of simulated (proto)cluster galaxies

and observations an appealing route for studying the process of star formation, galaxy assembly and large-scale cluster assembly through cosmic history (De Lucia and Blaizot, 2007; Lin et al., 2013; Zhao et al., 2015).

1.4.2 Non-Gravitational Processes

We have already mentioned in previous sections that our physical description of protoclusters would be flawed without the addition of baryons to the equation. We tend to forget about baryons when we talk about structure growth mainly because we know that they fall already at early epochs in the potential wells of DM, so that the gas distribution of the cosmic web follows closely the DM distribution (see figure 1.1).

If we would zoom in into clusters we would see that, baryons in clusters are not only concentrated in galaxies, but can also be found in the intermediate regions between galaxies. Indeed, in the region between galaxies inside clusters resides the hot and diffuse plasma, the ICM, where thermal plasma coexists with magnetic fields and relativistic particles, holding the major part of the baryonic matter in clusters. The ICM has temperatures of $T \sim 10^7 - 10^8 K$ and is quite tenuous, with electron number densities of $n_e \sim 10^{-4} - 10^{-2}\mathrm{cm}^{-3}$. Although it is formed mainly of hydrogen and helium, it also holds a mean abundance of heavier elements of about 1/3 of the solar abundance. This intra-cluster plasma emits strong X-ray radiation causing luminosities of $L_X \sim 10^{43}$ - 10^{45} ergs/s that can be detected observationally.

Major mergers are common events in the hierarchical process of structure formation. These collisions of protoclusters at velocities of several thousands of kilometers per second, are one of the most energetic phenomena in the Universe (Sarazin, 1988). They generate 'Gravitational feedback', composed by shocks and compression waves in the ICM, releasing important amounts of energy ($\sim 10^{62}$ 10^{65} ergs) and increasing its entropy (Quilis et al., 1998; Miniati et al., 2000; Ricker and Sarazin, 2001; Nagai et al., 2003; Dolag et al., 2005). This translates also to smaller scales within the already collapsed structure, where subhalo mergers and random gas flows produce weaker shocks, that contribute to the virialization of halos via thermalization of the intra-cluster gas. (McCarthy et al., 2007).

If only gravitational feedback was present, we could explain the evolution of protoclusters as a self-similar process. However, observational data drifts away the self-similar model strongly enough to make us suspicious that other non-gravitationally induced cooling and heating processes are also having a strong influence in the behaviour and evolution of galaxy clusters. Certainly, on galactic scales gravity operates in connection with a number of gas dynamical and astrophysical phenomena, some of which will be reviewed in the following sections.

1.4.2.1 Gas Radiative Cooling

The cooling of gas through radiation plays an important role in gas dynamics in clusters, ICM emissivity and self-similarity breaking. The cooling time of gas can be expressed in a first approximation in terms of its entropy and temperature in the Bremssstrahlung regime as follows:

$$t_{cool} \approx 17 \left(\frac{K}{130 keV cm^{-2}} \right)^{3/2} \left(\frac{k_B T}{2 keV} \right)^{-1} Gyrs \tag{1.1}$$

Following equation 1.1, if we have a galaxy cluster with $k_B T \sim 2.5$ keV, the corresponding cooling time for regions with entropies $K \sim 130$ keV or lower, is less than the Hubble time, which means that gas in these regions will cool and be evacuated earlier from the hot gas in the cluster core (Voit and Bryan, 2001). This low entropy gas will be substituted by higher entropy gas coming from outer regions, and thus the average gas entropy inside the cluster will increase.

This prediction has been confirmed repeatedly by hydrodynamical simulations. Non-radiative simulations fail reproducing the ICM profiles observed, while simulations including radiative cooling produce a better match specially outside cluster core regions (see e.g. Pearce et al., 2000; Muanwong et al., 2001; Dave et al., 2002; Kay et al., 2004; Nagai et al., 2007). Unfortunately, simulations considering only radiative cooling have some undesirable effects in the cluster centric regions, like an unobserved increase of temperature towards the cluster core or overcooling leading to a too large star production (see e.g. Balogh et al., 2001; Lin et al., 2003; Diaferio, 2004; Gonzalez et al., 2007).

These two flaws of radiative cooling hint towards the need of a gas heating mechanism that counteracts cooling and controls star formation. Discovering all the processes capable of doing this is a complicated matter, and poses a challenge in numerical prescriptions. In the following we will discuss the two mechanisms that are undoubtedly involved in counterbalancing the deficiencies of radiative cooling, and in the regulation of star formation.

1.4.2.2 Supernova Feedback

Supernova (SN) explosions and SN-driven winds are a direct product of the star formation process and are thought to help producing a self-regulated cosmic star formation rate (e.g. Springel and Hernquist, 2003). SNe not only do heat the surrounding medium but also enrich the inter-galactic medium (IGM) by distributing metals from star-forming regions to the rest of the galaxy.

As cosmological simulations cannot resolve stellar physics, the physics of the interstellar medium (ISM) like star formation and SN feedback is implemented via phenomenological prescriptions (e.g. Braun and Schmidt, 2012). Doing so, it has been shown that SN feedback helps reducing stellar mass fractions produced by radiative cooling in simulations and

flattens the temperature profile matching it better to observations (Borgani and Kravtsov, 2011b). However, SN feedback alone with radiative cooling cannot reproduce the thermal structure of galaxy clusters or the correct core entropy level reported by observations. Moreover, in simulations with radiative cooling and SN feedback, BCGs tend to have larger stellar masses than the ones observed, even if at high redshifts their star formation is lower than the one inferred from observations (Bassini et al., 2020). This will be further explored in section 3 of this work.

1.4.2.3 AGN Feedback

It is impossible to make an accurate model of protocluster evolution without the inclusion of AGN feedback. We know that a great part of the heating of the ICM plasma is due to BH feedback. Furthermore, observations suggest a correlation between the BH masses and the halo and bulge properties of the galaxies they are hosted in (e.g. Ferrarese and Merritt, 2000; McNamara and Nulsen, 2007; Chandran et al., 2009). In fact, almost all dynamically relaxed cool core clusters have an active central radio emitting source (e.g. Burns, 1990; Ball et al., 1993; Bîrzan et al., 2004; Sanderson et al., 2006).

BHs heat the ICM by the generation of relativistic jets that shock the ICM. This feedback is proportional to the rate at which the BH accretes mass from the surrounding intracluster gas. Through radiative cooling, gas cools and falls into the center of the cluster. The BH accretes the gas and in turn produces the jets that inject energy into the ICM, compensating radiative cooling and slowing down the accretion rate. When the accretion rate slows down, the injection of energy due to feedback decreases and thus the cooling of gas increases again, creating a self regulated cycle (e.g. Rosner and Tucker, 1989).

AGN feedback in cosmological simulations has proven to be able to reduce star formation in BCGs, matching better current observations. Nevertheless, implementing AGN feedback in simulations is a challenging task and thus many different subgrid-physics implementations have been tried out during the last years (e.g. Springel et al., 2005; Sijacki et al., 2007; Puchwein et al., 2008; McCarthy et al., 2010; Puchwein et al., 2010; Martizzi et al., 2012; Ragone-Figueroa et al., 2013; Battaglia et al., 2013).

Even if there is no consensus in which implementation describes better the effect of AGNs in (proto)clusters of galaxies, results from simulations show that AGN feedback is efficient in reducing star formation, in lowering the amount of hot gas in small clusters and groups, and also in spreading heavy elements through the ICM, thus reproducing better observational results (Sijacki et al., 2007; Puchwein et al., 2008; Fabjan et al., 2010a; Martizzi et al., 2012; Planelles et al., 2013; Le Brun et al., 2015).

Current simulations suggest that in order to describe observational properties better, AGN and SN feedback may be complemented by additional physical processes. Some pos-

sible candidates are cosmic rays (CRs), thermal conduction, heating induced by galaxy motions or AGN-induced bubbles (e.g. Zakamska and Narayan, 2003; Kim et al., 2005; Sijacki et al., 2008). What is clear is, that further research is needed if we want to understand the sources of discrepancies between observations and simulations and to find the correct interplay between the different baryonic processes.

1.5 Detection Methods for Clusters and Protoclusters of Galaxies

1.5.1 Searching for Galaxy Clusters

Surveys focused on the search for galaxy clusters and their progenitors have developed into a multi-faceted and multi-wavelength discipline, with success in detecting clusters at increasingly high redshifts. Generally, observational studies of clusters search for concentrations of massive galaxies, like red sequence galaxies, or for distinctive features of the hot ICM in the X-ray emission or by using the Sunyaev–Zeldovich effect.

An example of multiwavelength observations of clusters can be seen in figure 1.5. In this example it is easy to discern the different components of a cluster. In the optical we see the luminous stars that reside inside galaxies and also those stars outside galaxies that conform the intracluster light (ICL). In X-rays (colored in purple) we can see the hot gas belonging to galaxies and also diffuse plasma, that not being directly associated to galaxies contains the bulk of baryonic matter in clusters and conforms the ICM. Dark matter can be detected via gravitational lensing of the galaxies lying in the background of the cluster, as seen in the right panel of the image.

Performing the kind of detections shown in figure 1.5 is a complicated matter in continuous development. As clusters are composed of galaxies, one could think that finding those clusters is as simple as searching for the galaxies that compose them. Even if this is a valid approach, the reader needs to take into account that galaxies turn faint rapidly with redshift, making their detection more difficult at higher redshifts. As an example, galaxies at $z \approx 2$ are approximately 2 magnitudes fainter than those at $z \approx 1$, so to detect them we need imaging depths that pose a significant challenge (Muzzin et al., 2013). This has led to the exploration of other methods for cluster detection.

We know that galaxy clusters have a hot gaseous component that emits largely in X-rays. CMB photons transversing the ICM suffer an inverse Compton scattering by the high-energy electrons inside this gaseous component, receiving an energy boost during collision. This process, called Sunyaev–Zeldovich effect (SZ effect), causes spectral distortions in the CMB spectrum, which together with X-ray surveys can be used to identify clusters of galaxies. As an example, Bleem et al. (2015) found hundreds of new cluster candidates in the 2500 deg2 South Pole Telescope SZ survey (SPT-SZ) with a median redshift of

$z \approx 0.55$ and a tail extending to $z \approx 1.478$. However, even this detection method has a limited sensitivity that lies at $z \approx 1.5$ making it a complementary but not substitute approach to the galaxy detection method.

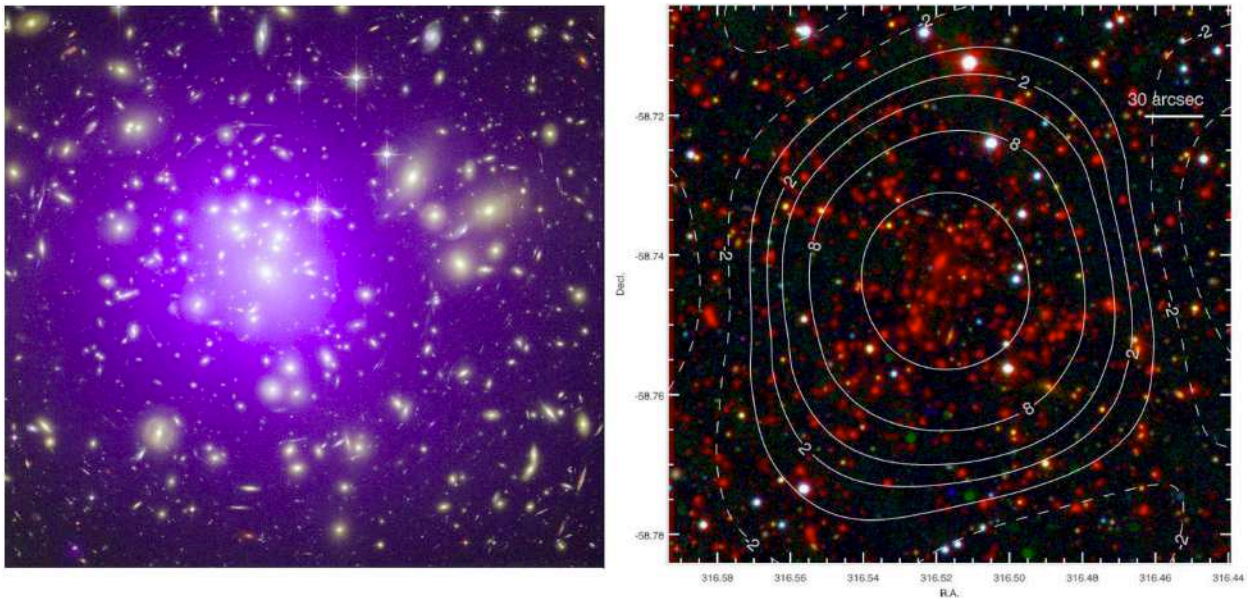

Figure 1.5: Left panel: the composite X-ray/optical image (556 kpc on a side) of the galaxy cluster Abell 1689 at redshift z = 0.18. The purple haze shows X-ray emission of the $T \sim 108K$ gas, obtained by the Chandra X-ray Observatory. Images of galaxies in the optical band, colored in yellow, are from observations performed with the Hubble Space Telescope. The long arcs in the optical image are caused by the gravitational lensing of background galaxies by matter in the galaxy cluster, the largest system of such arcs ever found (Credit:X-ray: NASA/CXC/MIT; Optical: NASA/STScI). Right panel: the galaxy cluster SPT-CL J2106-5844 at $z = 1.133$, the most massive cluster known at $z >$ 1 discovered via its Sunyaev–Sel'dovich (SZ) signal (M200 1.3 × 1015 M). The color image shows the Magellan/LDSS3 optical and Spitzer/IRAC mid-infrared measurements (corresponding to the blue-green-red color channels). The frame subtends 4.8 × 4.8 arcmin, which corresponds to 2.4 × 2.4 Mpc at the redshift of the cluster. The white contours correspond to the South Pole Telescope SZ significance values, as labeled, where dashed contours are used for the negative significance values (Foley et al., 2011).

A more exhaustive discovery of high redshift clusters may be done by turning to the fundamental cosmological definition of a cluster and thus searching for overdensities in redshift space. The advantage of this approach is that it does not depend on the type of stellar population present in the galaxies conforming the cluster, which varies with redshift. An example of the use of this technique was presented by Strazzullo et al. (2015), where the authors where able to find promising cluster candidates in the range $1.5 < z < 2.5$.

Hopefully the rapid development of observational techniques and instruments will enable the discovery of many more clusters at increasing redshifts.

1.5.2 Searching for High Redshift Protoclusters

In the protocluster realm we lack a well-defined red sequence or a hot ICM, which makes the unambiguous detection of these structures exponentially difficult with increasing redshift. The most clear hint towards the presence of a protocluster is a high concentration of galaxies and gas clustered together in angular and redshift space in comparison to the field. Thus, the main techniques for finding protocluster candidates are constructed around this observational signature.

Protoclusters lie in the nodes of the filamentary cosmic web, therefore surveys that trace the formation of this cosmic web are directly surveys of cluster formation. Unfortunately, the detection of protoclusters with standard galaxy surveys is extraordinarily difficult because of two main reasons. First, clusters of galaxies are already found rarely, which means that large cosmic volumes have to be covered if we want to find the progenitors of this uncommon structures. Second, the higher we go in redshift the less time did the structures have to collapse, and thus the smaller is the density contrast. Highly sensitive surveys and good spectroscopic coverage are indispensable if we want to differentiate real structures from projection effects and confirm candidates with reasonable confidence.

Despite the difficulties surrounding the detection of protoclusters some of them have been detected incidentally as by-product of large spectroscopic surveys. Some examples are the protoclusters discovered by Steidel et al. (1998, 2000, 2005) at $z = 2.30$ and $z = 3.09$, which were found in a survey using rest-frame UV spectroscopy of candidate high redshift galaxies.

Even though this kind of accidental findings may happen, the truth is that the size of the cosmological volumes that can be covered at high redshifts using rest-frame UV spectroscopy alone are relatively small, thus other authors have chosen to perform first a preselection of the most overdense regions from a wide field photometric survey and then followed up those regions spectroscopically. Doing so Toshikawa et al. (2016) performed a protocluster survey in the Canada–France–Hawaii Telescope Legacy Survey (CFHTLS) deep fields, finding several new systems in the redshift range at $z \sim 3 - 6$. This two step approach is significantly faster than performing a spectroscopically complete survey. The disadvantage is that there is no complete spectroscopic sampling of the cosmic web and one is inevitably most sensitive to structures that are relatively compact in the sky plane.

Another way of bypassing the drawbacks of performing a very deep and wide galaxy survey is to target directly the surroundings of previously identified galaxies that are though to be tracers of massive forming systems. A meaningful amount of protoclusters have been

found by targeting the environment of previously known high redshift radio galaxies that have many properties that indicate they may be progenitors of the brightest local galaxies (e.g. Kurk et al., 2000, 2004; Miley and De Breuck, 2008; Mawatari et al., 2012; Wylezalek et al., 2013; Collet et al., 2015).

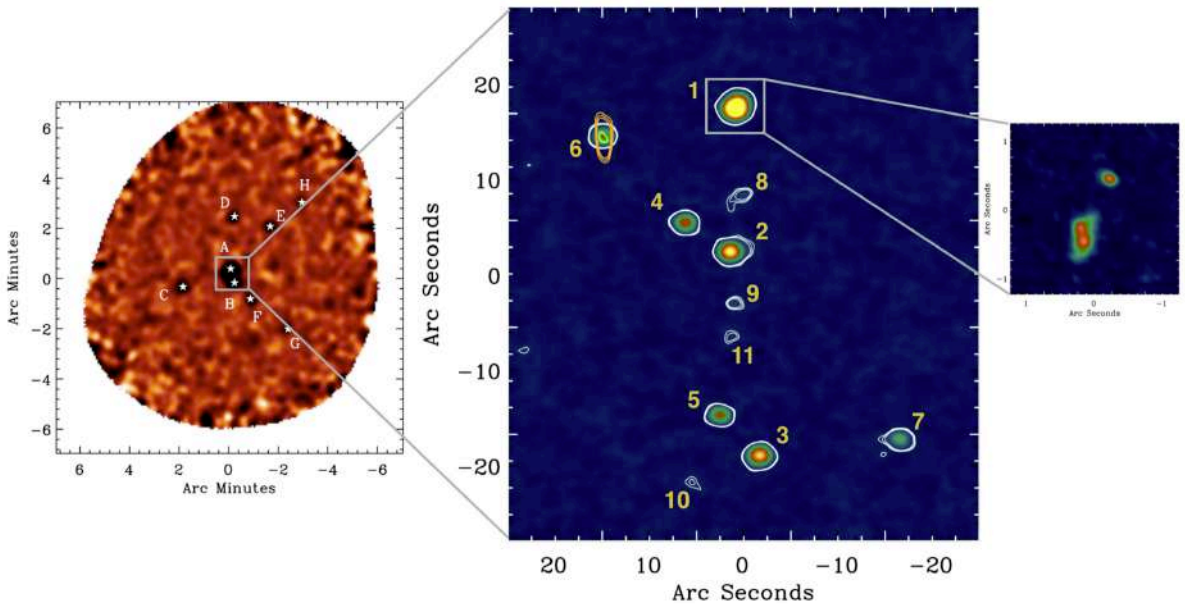

Figure 1.6: DRC from large to small scales – the core of an extreme proto-cluster of galaxies at zspec = 4.002. The left panel shows a wide-field LABOCA map at 870m of the environment of DRC, smoothed to a resolution of 27. The eight DSFGs suggest an 2 times over-dense region compared ot the field (Geach et al., 2017). The middle panel shows the ultra-deep ALMA 2 mm continuum map of DRC. Green and orange contours (from 5) represent the radio continuum emission observed by the Jansky VLA and ATCA, respectively. DRC is resolved into at least 11 components, which is also a significant over-density of DSFGs according to the most recent ALMA number counts (Oteo et al. 2016b; Aravena et al. 2016; Dunlop et al. 2017). The right panel shows a high-resolution ALMA continuum map at 870 m of the brightest DSFG in the proto-cluster, referred to here as DRC-1. This component is resolved into at least three star-forming clumps (Oteo et al., 2018).

DSFGs are also believed to be good tracers of protoclusters. Even if many of them are completely optically obscured, they can be detected at far-infrared and submillimeter wavelengths due to the dust heated by ultraviolet radiation of newly forming stars **?**. DSFGs are though to be the progenitors of present-day ellipticals and thus an overdensity of these galaxies could indicate the presence of a protocluster at an early stage where future elliptical galaxies are still going through their formation phase (Oteo et al., 2018). The main problem of targeting protoclusters in this way is that we can expect our sample to be

biased towards the most bright sources, which may lead us to wrong conclusions about the history of star formation in clusters and the evolution of the ICM. An observation DSFGs in a protocluster region is presented in figure 1.6.

Albeit all the obstacles surrounding the detection of protoclusters, the techniques described above have made possible the gathering of a considerable number of structures that point out distinct features of (proto)cluster evolution. A compilation of most of the objects confirmed as protoclusters found to date is displayed in figure 1.7. Looking at this figure we see that protoclusters have been detected in a wide range of redshifts. About half of the protoclusters detected lie in the epoch between $z = 2$ and $z = 3$, while the other half is around $z = 3$ and $z = 8$. Even so, the diversity in the available protocluster sample makes it currently difficult to establish a complete picture of protocluster formation and evolution with observational data alone.

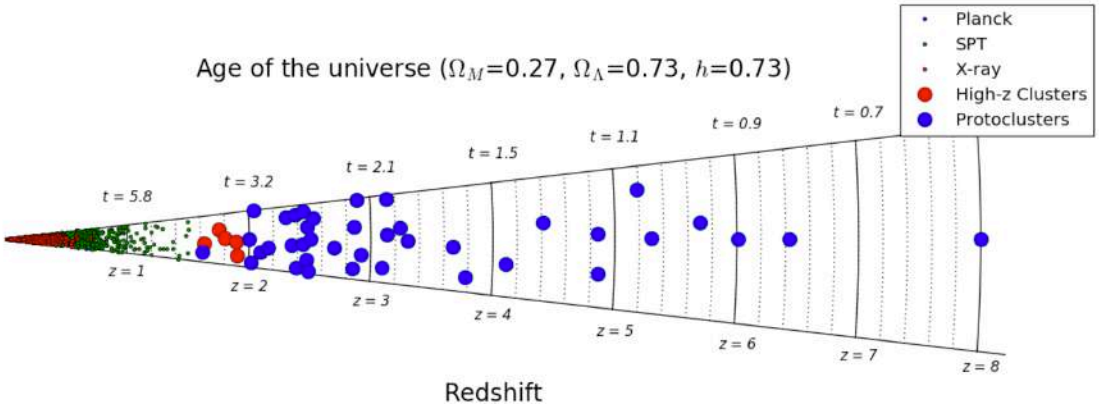

Figure 1.7: The distribution of redshifts of protoclusters selected from the literature (large blue symbols). The data for clusters below $z = 1.5$ were taken from the compilation of clusters detected in X-ray and SZ surveys of Bleem et al. (2015). Large red symbols are high redshift clusters at $z > 1.6$. The polar axis holds no information and is used for visibility purposes only. Redshifts and ages (in Gyr) are indicated along the radial axes (Overzier, 2016).

1.6 Objective of This Work

In our hope of understanding structure formation in the Universe, we try to overcome current difficulties encountered in theory and observations by developing new technologies and carrying out new theoretical models. As we have seen, an analytical approach to the problem is unsatisfactory as it misses many of the complex but fundamental processes affecting structure growth. Also, observations face many uncertainties and possibly also significant biases.

Luckily, the recent improvements of high performance computers and the establishment of supercomputing centers like the Leibniz Supercomputing Centre (LRZ) enables us the modelling of these complex non-linear processes in a consistent way. Using hydrodynamic codes applied to cosmological dark matter simulations, we are capable of reproducing structure growth at different scales with increasing resolutions. Simulations also allow us varying the physical processes involved in the evolution of structures, which helps us understand better the relevance of each of the added phenomena at different redshifts. Even if simulations can not be considered substitutes of observations, they are a powerful tool to understand cosmological structures beyond what observation can capture today.

With the aim of understanding better the effects of baryonic physics in the evolution of massive galaxy clusters, we perform hydrodynamical cosmological simulations of massive galaxy clusters with varying subgrid prescriptions. We study important protocluster properties like stellar and gas mass contents, temperature histories and temperature vs density relations, SFRs at high and low redshifts of the galaxies inside the protocluster and of the complete protocluster region and SHMRs for sattelite and central galaxies. Finally, we discuss the possible sources of generalized disagreement between observations and simulations and propose future studies for the improvement in the consensus between observations and simulations.

Chapter 2

Methods

As has been extensively discussed previously, observing clusters and extracting data from observations is a complicated task that may be subject to strong constraints and biases. Therefore, confronting observational data with theoretical models, and in particular with numerical simulations, has been a key factor enabling the accelerated progress of recent cosmological research. Indeed, simulations are the method of choice to predict the full non-linear development of the initial conditions in the standard ΛCDM cosmology. With them we can also link initial conditions of Cold Dark Matter (CDM) cosmologies to observations of galaxies at the present day. Without simulations we would have not arrived at the current structure formation paradigm, which as technology advances and simulations improve, is being subject to further and more detailed scrutiny. Simulations enable astronomers to test hypotheses, much as experimental physicists do in the laboratory. By doing so, they help with the interpretation of observations and also guide the design of new observational campaigns and instruments.

As dark matter is the dominant mass component, the primary route to understanding how galaxies form and evolve in their cosmological context, is to comprehend the properties of their dark matter haloes over a wide range of physical scales and across all of cosmic history. Dark matter is assumed to consist of elementary particles that interact only gravitationally. To reproduce the properties of DM, simulations use a set of discrete point particles that represent a discrete lump of the collisionless dark matter fluid. This representation as an N-body system is obviously only an approximation, that improves the more particles we use. This is, in turn, limited by the available computational power.

Because the accuracy of results in simulations depends so heavily on the particle resolution and cosmological box size, simulation teams try to take advantage of every advance in numerical algorithms and computer hardware to be able to simulate bigger boxes with increasing resolution. Doing so, the current generation of cosmological codes has reached a high degree of accuracy, such that we can resolve without major problems DM clustering of halos and their internal structure over cosmological volumes of hundreds of cubic cMpc using billions of DM particles.

Nowadays, we have reached such a resolution in DM simulations that we believe to have a very complete picture of the clustering of matter in the non-linear regime from halo to subhalo scales. (Moore et al., 1999; Springel et al., 2001; De Lucia et al., 2004; Gao et al., 2004; Kravtsov et al., 2004). We have also a strong consensus related to important questions like the shape of the central dark matter density profile of collapsed halos (Navarro et al., 1997; Navarro et al., 2004; Stadel et al., 2009). This advancements have been possible partly because we treat DM as a collisionless fluid and we know what are the key ingredients in order to have high accuracy in colissionles situations, i.e. an accurate gravitational force calculation, accurate time integration and a large enough number of particles so that we can resolve smaller scales.

The problem of DM-only simluations is that even if we know how to implement them correctly to get a detailed description of DM structures, they lack the information on all the baryonic processes that affect the formation and evolution of large scale structures and their observables at very different scales. Even if DM is believed to be the dominant component in the mass of the cosmological density field, at the scales of galaxy clusters the introduction of baryons in forms of gas and stars is completely unavoidable. Many X-ray and Sunayev-Zeldovich effect related observations of the hot ICM are used to place constrains on the structure of galaxy clusters. Baryons may alter clusters of galaxies in outstanding ways, affecting their survival, abundance, radial distribution and mas-loss rates. Thus, ignoring baryons in clusters would be negligent.

2.0.1 Seminanalytical Models and Hydrodynamical Simulations

For many years cosmological hydrodynamical simulations have been unable to reproduce key observational features related to galaxies, like the shape and normalization of galaxy mass functions, their compactness and the quenching of star formation (e.g. Scannapieco et al., 2012, and references therein). Driven in part by this failure, semi-analytical models have gained a lot of relevance during the past years when performing comparisons between galaxy surveys and theory (see Cooray and Sheth, 2002; Baugh, 2006).

Semi-analytical models use pre-calculated halo formation histories and put on top of those simplified models for physical processes such as gas cooling, star formation, supernova feedback, etc. The principle behind this procedure is that in the hierarchical clustering paradigm, DM halos build up by successive merging from smaller pieces, so that halos which have the same mass at some specified time can nontheless have very varied formation and merging histories. These halo formation histories play a large part in determining properties, like masses and morphology, of the galaxies they contain. Thus, the fist key ingredient in semi-analytical models is the determination of the formation history of the halos, i.e. the construction of a merger tree. Merger trees can be calculated using a Monte Carlo method or a DM-only cosmological simulation.

The Monte Carlo method can construct merger trees for a particular cosmology and initial conditions describing the build-up of DM halos through merging. The number of halos of different masses per unit volume can then be calculated using the Press-Schechter mass function. Then the formation histories for each representative set of halos with certain mass is calculated. The process of galaxy or cluster formation is followed separately for each halo merger tree. An example of the application of such a procedure can be found in Lacey (2001). If a DM-only simulation is used instead, the formation of the halos can be followed through time by going through the different output-files produced at different redshifts. With the use of a post-processing code (f.e. SUBFIND) final halos and their high redshift progenitors can be identified and thus a merger tree for each halo can be directly constructed.

The evolution of the baryons within the DM halos is then calculated using the models and assumptions set "ab initio" about the different baryonic processes and the influence that interactions between halos may have in those. This approach, although flexible, presents the inconvenience of possible wrong extrapolations due to poor approximations in the assumed relations. Even so, we can not deny that semi-analytical models have been very valuable. Examples of their usefulness include the interpretation of observations of galaxies within the context of the cold dark matter framework, relating galaxy populations at different redshifts, the creation of mock galaxy catalogues to investigate selection effects or to translate measurements of galaxy clustering into information concerning the occupation of dark matter haloes by galaxies (Bower et al., 2008; Somerville et al., 2008; Guo et al., 2011; Bower et al., 2012).

Even if they are more computationally demanding, hydrodynamical simulations have a number of important advantages over semi-analytical approaches. One of the main advantages is that even if we have to make some assumptions, the amount of them is noticeably reduced in hydrodynamical simulations when compared to semi-analytical models. Hydrodynamical models evolve DM and baryons self-consisntently from the initial conditions forward, and thus they automatically include processes related to the interaction of both components, like the back-reaction of the baryons on the collisionless matter inside and outside halos. Also, with full cosmological hydrodynamical simulations we can model galaxies, the corresponding IGM and the interface of both of them simultaneously, which is critical for understanding feedback cycles and fuelling mechanisms in galaxies. Moreover, hydrodynamical simulations provide in general higher resolution descriptions of baryons, which allows comparisons with a wider range of observables.

Recently, the development of hydrodynamical simulations has accelerated dramatically. Thanks to the higher performance of current computers and the improvement in numerical codes, cosmological hydrodynamical simulations are capable of modelling increasingly well processes in galaxies and galaxy clusters such as radiative cooling, star formation, stellar feedback or AGN feedback (Borgani and Kravtsov, 2011a). Thus, current structure forma-

tion calculations done with the use of coupled DM and baryonic gas are noticeably more realistic and far more into the highly non-linear regime than the calculations done with DM-only simulations. Indeed, to date the agreement between simulations and observations of galaxies and galaxy clusters is so good that comparisons between theory and observations can be used to measure cosmological and physical parameters (e.g. Croft et al., 1998; Viel et al., 2004; McDonald et al., 2005).

However, as we have briefly mentioned before, running, storing and analyzing such simulations is a challenging task from a technical point of view. The use of HPC facilities like the LRZ is mandatory if we want to perform cosmological hydrodynamical simulations that cover a big enough volume with a high resolution. There is a high variety of fundamentally quite different numerical hydrodynamical methods in use for baryon modelling, the most prominent ones being the Lagrangian Smoothed Particle Hydrodynamics (SPH; Lucy, 1977; Gingold and Monaghan, 1977) and Eulerian Mesh-Based hydrodynamics (e.g. Stone et al., 1992) with or without Adaptive Mesh Refinement (AMR; Berger and Colella, 1989). In the following sections we will start with dark matter simulations and continue our route exploring the different numerical methods that compose a successful cosmological hydrodynamical simulation.

2.1 Routemap to a cosmological hydrodynamical simulation

2.1.1 Initial Conditions

The first challenge in the building of a cosmological simulation is the establishment of initial conditions for the dark matter particles involved. In order to reproduce the homogeneity and isotropy of the early universe we need an unperturbed initial mass distribution, thus we lay particles in a 'glass-like' initial distribution (White, 1994; Baugh et al., 1995). Such a 'glass-like' distribution may be formed when a Poisson particle distribution in a periodic box is evolved with the sign of gravity reversed until any residual forces have dropped to negligible levels (Springel, 2005). Then an initial displacement field is constructed in Fourier space using the Zeldovich approximation, with an amplitude of each random phase mode drawn from a Rayleigh distribution. Simulations start at high redshifts (between $z = 70$ and $z = 180$ depending on resolution) and are evolved to the present day using a leapfrog integration scheme with individual adaptive timesteps.

2.1.2 Modeling Gravity: Gravitational Softening

The DM component in simulations is represented with a series of particles that conform a colissionless fluid that interacts only gravitationally. This means, that we sample the phase-space distribution functions in our cosmological volume with discrete particles that conform an N-body system. The main problem with this appears when two particles come very close together, as the inherent numerical error of computational devices introduces artificial two-body interactions between these particles that violate the premise of colli-

sionless dynamics.

To prevent this inconvenience, a softened gravitational force replaces the Newtonian force below a certain softening scale ϵ, so that the potential at zero lag becomes $-Gm/\epsilon$. Strong reductions of the force occurs only at distances $\sim \epsilon$. At distances above 2.8ϵ the force is already fully Newtonian. In practice, we are limiting the maximum amount of acceleration a particle can exert on another. By doing this, we are capable of reproducing colissionless dynamics and at the same time we manage to avoid the formation of bound particle pairs and simplify the integration of particle movement.

2.1.3 Modeling Gravity: Gravitational Forces and the Tree-Particle-Mesh Approach

If we aimed to calculate the interaction of each particle that composes the fluid with each other over the complete box, cosmological simulations would take an unaffordable amount of time and resources to get completed.To alleviate this problem we have to take a less direct but more intelligent approach, called the Tree-Particle-Mesh (Tree-PM) scheme. This scheme combines the best of two different algorithms for calculating gravitational forces, the *hierarchical multiple expansion* with an oct-tree algorithm and the *particle-mesh algorithm.*

In the hierarchical multiple expansion procedure, we calculate the interaction between particles in a hierarchical way. That is, if we have a particle x, the forces exerted on this particle from particles nearby is calculated accurately, while the forces of faraway particles are calculated in an averaged way using a multipole expansion. Let us say we have a group of dark matter particles in our box. The tree construction starts with an enclosing cubical root node in which the particles are inserted sequentially one by one. Each cube contains eight siblings, each with half the side-length of the parent cube. These cubes form the nodes of an oct-tree structure. The tree is constructed such that each cube contains either exactly one particle, or is progenitor to further nodes, in which case the node carries the monopole and quadrupole moments of all the particles that lie inside its cube. A schematic illustration of a tree construction is shown in figure 2.1. After computing the corresponding multiple moments of each node recursively, these are used to approximate the gravitational forces. This tree is walked for each particle starting at the root node. If the multipole expansion is considered sufficiently accurate (following a previously established criterion), it is evaluated and added to the cumulative force. If not, the node is opened and the subnodes are considered in turn.

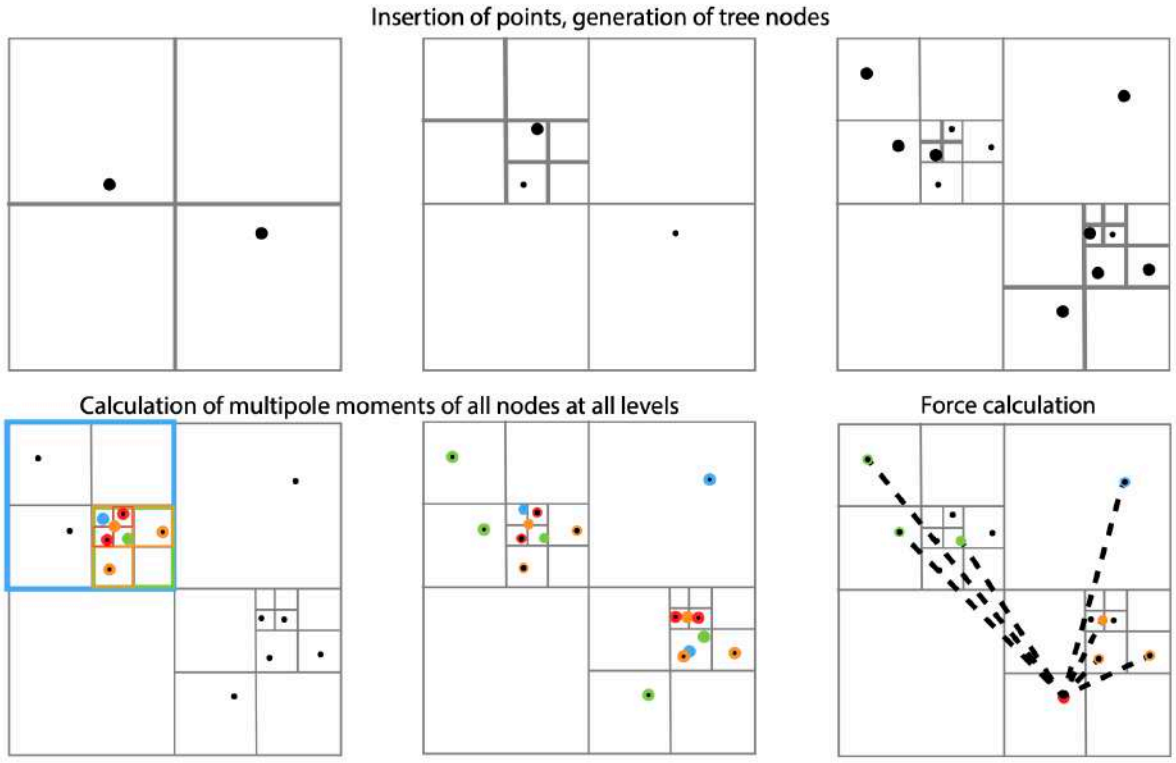

Figure 2.1: Schematic illustration of a tree construction, multipole-moment calculation, and force evaluation of one individual particle in an oct-tree algorithm (a quad-tree in the sketched 2D case). The upper panels show the insertion of particles and the consequent hierarchical splitting of the tree volume into sub-nodes. The lower left and central panels illustrate the calculation of multipole moments for all nodes, with the different colors denoting different depths of the tree hierarchy. The lower right panel represents the force evaluation between a single particle and the appropriate nodes. The goal of this algorithm is the reduction of this last evaluation with respect to an evaluation with all simulation particles (Weinberger et al., 2020).

In the Particle-Mesh approach, rather than working directly with forces, we work with the gravitational potential instead. Binning the mass distribution on a Cartesian regular grid via a cloud-in-cell (CIC) assignment, we can solve for the gravitational potential on the grid, then finite-difference it to get the force and interpolate the force field to the particle positions.A conceptually simple mathematical example application is considering the Fourier Transform of the Poisson Equation:

$$-k^2\phi_k = 4\pi G\rho_k \qquad \rightarrow \qquad \phi_k = -4\pi G\rho_k/k^2, \tag{2.1}$$

where ϕ_k is the gravitational potential in Fourier space, ρ_k the density, k the wavenumber and G the gravitational constant. Having an expression for the transformed gravitational

field, we can perform an inverse transform to get the potential field, which can be differentiated and interpolated to the particle position, giving as a result the forces exerted over each of the particles.

Both methods, the oct-tree and the particle mesh method, have strong and weak points. The Particle-Mesh algorithm is fast, conceptually simple and easily scalable to a large number of passing interface (MPI) tasks. However, it is bound to a cartesian mesh, which limits importantly the dynamic range of the calculation and poses an arduous deterrent for cosmological simulations. On the other hand, the oct-tree algorithm is efficient at handling large dynamic ranges in spatial scales, allowing high spatial force resolutions, but the scaling to a large number of MPI tasks is more difficult, especially when the clustering of the particle distribution is high (as it is usually in simulations at lower redshifts), as this means more work when establishing the subnodes.

The tree-PM algorithm has been designed to take the best of both worlds, just by splitting forces into short-range and long-range components. The short-range forces are computed using the tree algorithm while long-range forces are treated with the particle-mesh approach.The ability to discard far away mass distributions except for a local neighbourhood accelerates the tree force calculation significantly, making the complete Tree-PM scheme very fast, accurate and flexible.

2.1.4 Modeling Baryons: Adding the Gaseous Component

We know that if we want to model the complete picture we cannot forget about the gaseous component of large scale structures. The problem is that the interactions of gas are much more intricate than those of dark matter.Baryons can be described using several hydrodynamical methods, that can be mainly divided into two groups: Lagrangian Smoothed Particle Hydrodynamics (SPH) and Eulerian mesh-based hydrodynamics with or without mesh refinement.

SPH is a powerful Lagrangian technique to solve hydrodynamical problems, that was originally developed by the astrophysics community, but by now has found uses and applications in a wide range of fields. In this approach the flow is considered as a discrete phase of particles moving in space and carrying with them specific computational information, i.e. the fluid equations that govern the gaseous component evolve in a co-moving frame. Hydrodynamic properties are then evaluated at the particle positions, and are calculated from a weighted average of the values on other local particles. For example, the value of the function (or property) f in particle i can be calculated using:

$$f(x_i) = \sum_{j=1}^{N} \frac{m_j}{\rho_j} f(x_j) W(x_i - x_j, h)[1], \tag{2.2}$$

[1] see appendix A

where m_j and ρ_j correspond to the mass density of particle j and N to the total number of the particles that are in the field of influence of particle i. The function W is the Kernel function and determines the weight given to each particle. The choice of Kernel is not unique and remains one of the main topics of debate in theoretical computational fluid dynamics research. The parameter h contained in the Kernel function specifies the efficacy range of the Kernel function. We say that the particles are "smoothed" over a finite volume or a fixes mass, where h is the smoothing length, which implies that SPH codes are naturally adaptive with density and geometry. An example of an SPH code used in cosmological simulations is GADGET[2] (and its posterior updates [3]; Springel et al., 2001b; Springel, 2005) .

Eulerian methods on the other hand, use geometrical grids, either fixed or adaptive (the so called AMR or Adaptive Mesh Refinement codes), and evaluate the fluid parameters over the grid cells, by solving the Navier-Stokes equations for the flow field. In order to do that they use methods like the finite volume scheme (FVM), where volume integrals in a partial differential equation containing divergence terms are converted to surface integrals using the divergence theorem. These terms are then evaluated as fluxes at the surfaces of each finite volume. Because the flux entering a given volume is identical to that leaving the adjacent volume, these methods are inherently conservative. Some Eulerian codes used in cosmology are for example AREPO (Springel, 2010; Weinberger et al., 2020) or RAMSES (Teyssier, 2002).

It would be unreasonable to state that SPH or grid codes are "better" than the other. Each of them has its advantages and disadvanatges. For example, Eulerian AMR codes have a higher resolution for a given number of cells than SPH codes with an equal number of particles, and even if not easily they can be adapted to any previously chosen parameter, while SPH adapts to density only. However, as SPH is a Lagrangian method, advection of flow properties is inherent, while in AMR reproducing advection processes represents an important problem that entails unphysical increases of entropy. Also, SPH codes can be implemented so that in the absence of shocks they are inherently conservative of mass, momentum, energy and entropy. Shocks, however, represent a problem in SPH codes and by now they can only be treated correctly with grid codes.

It is clear that no approach is better than the other in absolute terms. The reality is that we need to choose the most appropriate method for the system we want to study and most importantly, we need to be aware of the limitations of the chosen approach, in order to interpret results correctly.

[2] https://wwwmpa.mpa-garching.mpg.de/gadget/
[3] https://wwwmpa.mpa-garching.mpg.de/gadget4/

2.1.5 Modeling Baryons: Subgrid Physics

The question that remains now is related to the treatment of the physics that is unresolved. As we mentioned in the beginning of the section, the formation of large scale structure and more specifically of clusters of galaxies is a process with an enormous dynamic range, where phenomena at very different scales have an impact in the final result. Obviously, resolving all scales in detail is completely impossible. However, we cannot simply ignore processes like star formation, supernova feedback and AGN feedback, as they have an important role in cluster dynamics and in the IGM composition. In order to account for those processes that fall under our resolution-limited simulations, we use 'subgrid models'.

Subgrid models are tuned so that some aspects of observational data are well-reproduced by the simulations. The implementation of the subgrid model can vary profoundly depending on the team, the cosmological simulation suite and the observables against which the subgrid model was calibrated. Describing all the different subgrid models for the different cosmological simulations in the field is out of the scope of this work. Nevertheless, it is possible to give a general sense on how such a subgrid model can be implemented when describing star formation, stellar and AGN feedback.

One of the first and more fundamental models applied to gas physics has to do with the radiative cooling of hot plasma. We know that this cooling has a crucial role in the formation and evolution of galaxies, by cooling low entropy gas and allowing the formation of stars. This cooling is captured in cluster observables related to the ICM, like in the self-similarity breaking of the $L_X - T$ scaling relation (Borgani and Kravtsov, 2011a). Typically, radiative cooling in cosmological hydrodynamic codes is handled with a scheme of the form:

$$u_i(t + \Delta t) = u_i(t) + \Delta t \times \Lambda(u_i(t + \Delta t)), \tag{2.3}$$

where u_i is the internal energy of particle i, Δt the integration timestep and Λ the cooling rate of particles with internal energy u_i at time $t + \Delta t$ (Zhu et al., 2017).

Stars form thanks to the cooling of gas and the creation of denser environments. In cosmological simulations we apply this by enforcing that stars are formed when the gas in a certain location exceeds a density threshold, that would cause it to become Jeans unstable. In the SPH formalism the local gas flow converges at a gas particle and from this gas particle a new star particle is created that represents a complete stellar population.

Real stellar winds are mimicked by averaging over the fictitious stellar population included in each simulated stellar particle. The main feedback processes that compose this wind come from Type II supernovae (SNII), Type Ia supernovae (SNIa), and asymptotic giant branch (AGB) stars, which are considered to be the most important drivers of stellar outflows and thus one of the principal sources of metal enrichment in the ICM. Each stellar population is characterized by an initial mass function (IMF), which describes the num-

ber of stars of a given mass per unit logarithmic mass interval in the stellar population. Consequently, the IMF also defines the ratio between SNII and SNIa, and thus the relative abundance of α-elements and Fe-peak elements for each stellar population.

The flow produced by the stellar feedback ejects masses of the different metal species produced by the stars. These masses are called stellar yields, and depend mainly on the metallicity with which the star originally formed and the type of outflow that the star ejects. There are some models and predictions that are usually used, however all prescriptions for the three sources of ICM enrichment suffer from profound uncertainties, and thus have to be treated with care (see e.g. Karakas and Lattanzio, 2007; Nomoto et al., 2013; Biffi et al., 2018).

Blach Holes (BHs) are, like stars, also created with a density criterion. They are established with an initial seed in areas where the gas density is larger than a certain threshold. This 'seeding' helps avoiding the formation of multiple BHs in the same galaxy, as they are not allowed to be seeded in a distance lower than a certain minimum. The BH accretion rate usually follows the well known Bondi–Hoyle–Lyttleton rate and is artificially capped at the Eddington accretion rate. Depending on the simulation project, AGN feedback may act in one or two separate modes. In the bimodal approach we encounter a 'radio' mode that operates at low accretion rates and a 'quasar' mode operating at high accretion rates (Dubois et al., 2014). During the radio mode the AGN deposits the feedback energy into a bipolar outflow modeled as a cylinder. The quasar mode instead, consists rather in an isotropic injection of thermal energy into the gas, modeled with a sphere of a certain radius.

The modeling of gas physics, star formation and feedback processes like supernovae and AGN feedback is critical in clusters of galaxies to create correct early type galaxies, to provide morphological diversity in galaxies and to regulate star formation. The current problem with subgrid models is that we do not have a unified prescription of those, partly because of the incomplete picture provided by observational data. Moreover, many physical aspects of galaxy clusters are sensitive to small changes in subgrid models, for example, the growth of BHs can be very reactive to the accretion model adopted.

In addition, technical aspects like the resolution of our simulations are aspects to consider when redesigning and readjusting parameters in the subgrid physics in use, so that we get results close to observational data. Indeed, the same feedback processes may give as a result very different galaxy morphologies at different resolutions. Naturally, this raises the question whether we have really understood the morphological evolution of galaxies and their quenching or the growth of BHs inside them. How much of what we think we understand is due to a good physical prescription and how much has to do with the consequence of artificial subgrid physics resolution artifacts? Answering these questions is fundamental if we seek to build cosmological simulations that help us understand real astrophysical and cosmological processes. Thus, studying cosmological simulations with different physics and resolutions is essential to help us improve the use of our subgrid models and thus bring

us to a deeper understanding of the evolution of (proto)clusters of galaxies and their substructures inside.

2.2 Searching Protoclusters in Simulations

Now that we know how to let structures evolve in a successful cosmological hydrodynamical simulation starting from some initial perturbations in a homogeneous field, we want to be able to identify the structures that we are interested in. For example, we want to identify clusters of galaxies at low redshift and be able to track them back to their protocluster stage.

As has been extensively discussed in the introduction, the formation of a halo has many complexities inherent to the non-linear nature of the process. Unfortunately, the definition of a DM halo is not a trivial task, as there is not such a thing as a density contrast delineating a halo boundary. In turn, what we find is a continuous, smooth outer density profile. Although one can identify a radial range, outside of which a significant fraction of mass is still infalling, this range is fairly wide and does not correspond to a single well-defined radius (Cuesta et al., 2008; Eke et al., 2001)

This has resulted in a number of various halo finding algorithms based on different mass definitions and halo boundaries (Knebe et al., 2011, 2013; Onions et al., 2013, show comparisons with different halo finders). Among the wide variety of used halo definitions the most widely used ones may be those based on the Friends-of-Friends (Davis et al., 1985) and the Spherical Overdensity (Lacey and Cole, 1994) algorithms.

2.2.1 The Friend-of-Friends Algorithm

Originally, the FoF algorithm was used to define groups and clusters of galaxies in observations (Davis et al., 1982; Huchra and Geller, 1982; Einasto et al., 1984) and was adopted to define collapsed objects in simulations of structure formation (Davis et al., 1985; Einasto et al., 1984).

The FoF algorithm considers particles to be members of the same group (i.e. 'friends"), if they are separated by a distance that is less than a given linking length. Friends of friends are also considered to be members of the same group. The linking length is the only free parameter of the method and is usually defined in units of the mean interparticle separation: $b = l/\bar{l}$. Where l is the linking length in physical units and $\bar{l} = n^{-1/3}$ is the mean interparticle separation of particles with mean number density of $\overline{n}$. In cosmological simulations this procedure is followed only by the DM component, as the general structure of the halo is established by the gravitational interaction of dark matter. The FoF algorithm is conceptually and mathematically simple, as it only has one free parameter, and assumes

no center for the halo or any type of preferred geometry or shape. Thus, it is capable of matching well the mass distribution of halos forming in the hierarchical structure formation models.

The two main disadvantages of the FoF algorithm are, on the one side the drawing of a theoretical interpretation of the FoF mass, and on the other side the sensitivity of the method to numerical resolution and to the presence of substructures. In a hierarchical paradigm the concentration depends on mass, redshift and cosmology, which means that the FoF halos will also vary with these parameters. At high redshifts the concentration of mass approaches its minimum, the number of particles in the FoF group is small and thus halos becomes 'fuzzier' and are more resolution dependent. The presence of substructure is an additional difficulty when it comes to the resolution and mass dependence of the FoF-identified halos (More et al., 2011). Besides, a common error caused by the working principle of the FoF algorithm is the joining of two neighboring distinct halos with overlapping volumes into a single group. Although this can happen at any time, the fraction of 'bridged' halos usually increases with increasing redshift or in between merging and crossing events.

2.2.2 The Spherical Overdensity Mass

The spherical overdensity algorithm defines the boundary of a halo as a sphere of radius r enclosing a given density contrast with respect to the reference density. Different than in the FoF algorithm, the definition of an SO halo requires the definition of a halo center. The common choices for the center of the halo in theoretical analysis are the minimum of the potential, the position of the most bound particle or the peak of density of the center of mass, although the latter is rarely used. To find simultaneously the center and the boundary of the halo, the SO method uses an iterative scheme. The overdensity radius R_c, is defined by solving the implicit equation:

$$M(< r) = 4\pi\Delta\rho(z)r^3, \tag{2.4}$$

where $M(< r)$ represents the total mass profile, $\rho(z)$ is the reference physical density at redshift z and r is the radius in physical units. The choice of density contrast and background density may be theoretically or observationally motivated. Common choices are defining the enclosed overdensity to be equal to the 'virial' overdensity at collapse predicted by the spherical collapse model, $\Delta\rho = \Delta_{vir,c}\rho_{crit}$ or 200 (500) times the background density (the reference density may be the critical or mean density).

The fundamental divergence between the FoF and SO methods is that the latter imposes a geometry, as it sets a center for the halo and a spherical boundary on the generally non-spherical mass distribution. Another inconvenience that may arise is the overlapping of spheres corresponding to different halos, causing a double counting of a certain fraction of mass (generally small; a discussion on the topic can be found in section 2.2 of Tinker

et al., 2008).

The enormous advantage of the SO algorithm is that the SO-defined mass can be measured in simulations as well as in observations. The only inconvenient difference is that the definition of the overdensity center may not be identical in both cases. Usually in observations the cluster center is defined at the position of the peak or the centroid of the X-ray emission or SZ signal, or at the position of the BCG, while in simulations we are dealing mainly with the DM component when defining halos.

2.2.3 Halo Finders

Halo finders are an indispensable post-processing tool that mix different methods and algorithms in order to identify structures and calculate their basic quantities like masses and radii. There is a wide variety of halo finders; however, in this work we will present the one that is used by most projects studying (proto)clusters of galaxies, which is SUBFIND.

SUBFIND identifies substructures as locally overdense regions of gravitationally bound particles by using a combination of the two methods explained above. Doing so, it manages to take advantage of what each of them does best. First, the FoF algorithm is used to perform a local density estimate for each particle with adaptive kernel estimation using a prescribed number of smoothing neighbours, so as to accomplish a first detection of density peaks. To establish a hierarchy of halos and subhalos the method starts from the isolated density peaks and adds particles in sequence of decreasing density. Whenever a saddle point in the global density field is reached that connects two disjoint overdense regions, the smaller structure is treated as a substructure candidate. To proof if the substructure candidate is physically bound to the bigger overdensity SUBFIND performs iteratively an unbinding procedure based on a tree-based calculation of the potential. All bound candidates with more than 20 particles are considered subhalos and are stored in the subhalo catalogues. The member particles of each subhalo are ranked according to binding energy and stored in that order. This facilitates the tracking of subhalos across the different outputs. Proceeding this way we have two sets of DM structures: FoF halos and subhalos. After having detected the main FoF groups and their substructures, the corresponding (virial, 200, 500, etc) radii and masses of these halos are estimated using the SO algorithm as explained above.

Even if SUBFIND profits from all the advantages of both methods, it is not infallible and also inherits some of the drawbacks mentioned in the previous sections. It is important to be aware of this, so that we do not take an error in SUBFIND as a physically meaningful result. Some examples of malfunctions in SUBFIND can be found in section 3.1.2.

2.2.4 Following a Halo Through Time: The Merger Tree

If we want to study the evolution of protoclusters through redshift we need to be able to identify the structures and then track them back to higher redshifts, following them through the different output files. To do so we first determine halos and subhalos at all output times and then we track structures back with a hierarchical merging tree that will give us a detailed description of how structures build up over cosmic time.

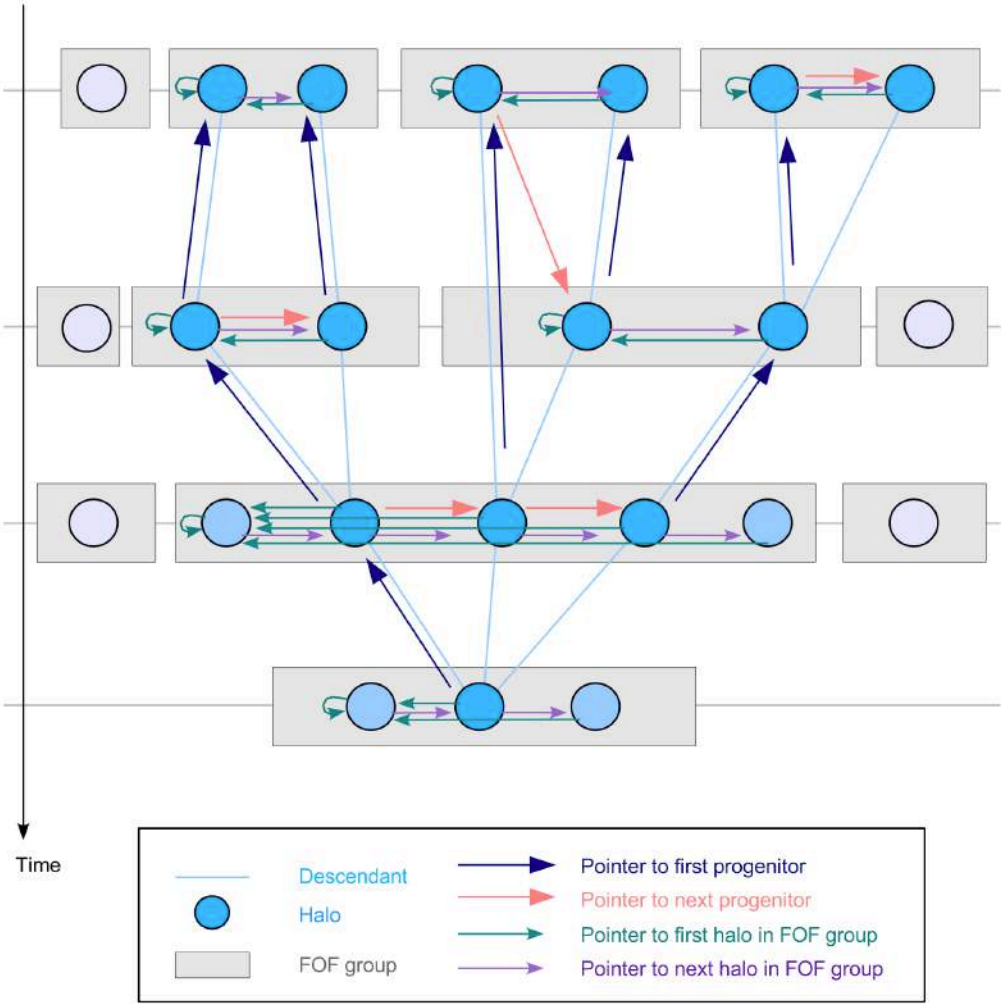

Figure 2.2: Schematic representation of the data structure of a general merger tree. At each output time, FoF groups are identified which contain one or several (sub)halos. The merger tree connects these overdensities. To facilitate the tree analysis, a number of pointers for each halo are defined. Each halo knows its descendant, and its most massive progenitor, and all halos in a given FoF group are chained together through the 'next halo' pointer (Springel et al., 2005a).

Due to hierarchical merging in CDM universes, a given halo can have several progenitors, although it will probably have only one descendant as the cores of DM structures do not split into two or more objects. Thus merger tree construction is based on the determination of a unique descendant for a given halo.

To determine the corresponding descendant, merger trees use the individual IDs that label each particle and track them between the different outputs in the simulation. For a selected halo we find all halos in the previous or subsequent output that contain some of its particles. The particles in each halo are counted in a weighted fashion, so that particles that are tighter bound in the final halo have a higher weight. By doing this we are capable of tracking rather the inner parts of the structure, which are less prone to suffer any kind of stripping when merging or falling into bigger halos, and thus are expected to survive longer.

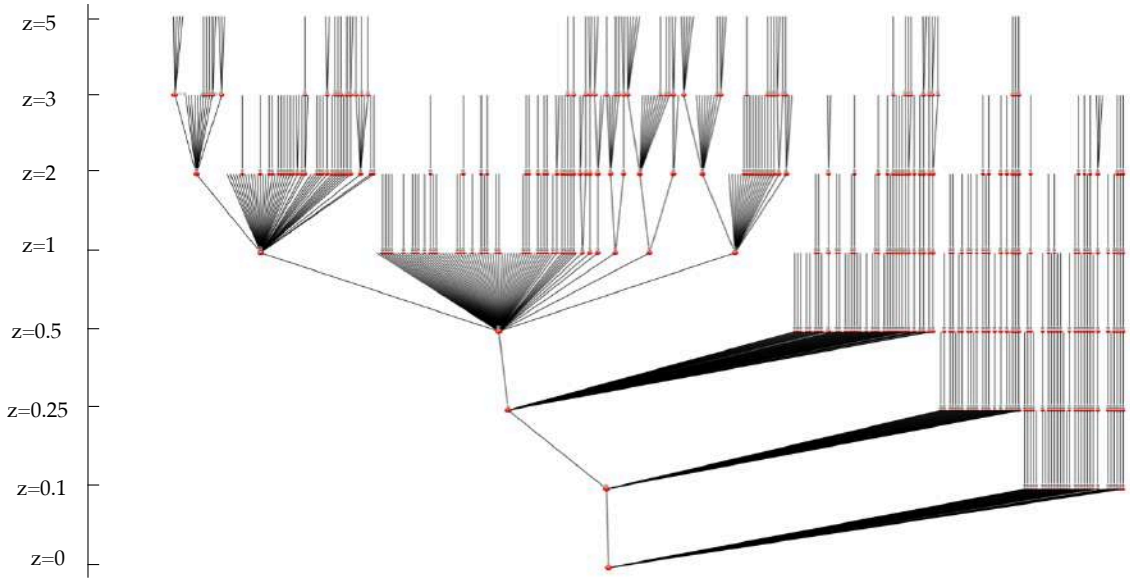

Figure 2.3: Example of a merger tree for the most massive cluster (with final mass $\sim 10^{15}M_{\odot}$)in the Compass Lagrangian region g1212639. The merger tree shows how the protocluster grows in mass through accretion at high redshift and a major merger at lower redshift.

The weighted counts are determined for each possible descendant and finally the one with the highest count is selected. This gives as a result a tree as shown in the schematic representation in figure 2.2. The FoF groups are represented at different times inside the grey boxes which may contain one or more subhalos. Each halo has a main descendant and this is linked to its substructures, which allows the retrieval of all progenitors of a halo, or of all other halos in the same FoF group. Subhaloes that are never connected to any $z = 0$ subhalo and that are never connected to any progenitor of any $z = 0$ subhalo are

not included in the trees.

There are several useful pointers for each tree subhalo. These include pointers to the dominant subhalo of the subhalo's FoF group, the next most massive subhalo in the FoF group, the progenitor that contains the largest fraction of the subhalo's particles, the subhalo's descendant and the next most massive subhalo that shares the same descendant. By doing this, each halo knows its descendant, and its most massive progenitor. Possible further progenitors can be retrieved by following the chain of 'next progenitors'. Halos in an FoF group (grey boxes) are linked together in a similar fashion by the pointers. An example of a real merger tree done for one of our galaxy clusters can be found in figure 2.3.

2.3 Cosmological Simulation Suites

As has been exposed along this work, there are various ways to build a working hydrodynamical cosmological simulation. For the gaseous component one can choose to use a Lagrangian method or an Eulerian code with or without AMR. On top of that the design and fine tuning of the subgrid physics can vary significantly. Also the resolution and the volume of the box is an issue when studying rare and massive object like galaxy clusters.

On the following we will present a short overview of the state of the art of current cosmological simulation projects. This does not intend to be a detailed description of their code implementation and subgrid physics as such an analysis would be out of the scope of this work. Rather, we try to give an idea of what simulations are available and where do our simulations lie with respect to their counterparts. Nevertheless, along this section the reader will be pointed to references with more detailed descriptions of each simulation suite.

2.3.1 Millenium Simulation Project

When published in 2005, the Millenium Run was the largest simulation of structure formation in a flat ΛCDM cosmology ever made. It used the a modified version of the publicly available Tree-PM code GADGET-2 (Springel, 2005), assuming $\Omega_m = 0.25$, $\Omega_b = 0.045$, $h = 0.73$, $\Omega_\Lambda = 0.75$, $n = 1$ and $\sigma_8 = 0.9$ and used 10^{10} particles to follow the dark matter distribution starting from $z = 127$ to the present day, within a comoving box of $500h^{-1}$ Mpc^3 and a spatial resolution of $5h^{-1}$kpc. Around 10^7 galaxies more luminous than the Small Magellanic Cloud were identified using SUBFIND, which conformed the first statistically relevant sample o galaxies formed in a cosmological simulation. A picture of the Millenium Run is shown in figure 2.4.

In 2008 a second simulation Millennium-II was completed with the same cosmology and same number of particles but in a 5 times smaller box and thus with 125 times better

mass resolution. The idea behind this run was that multiple simulations of differing mass resolution may allow to represent observed galaxy populations with high fidelity over a substantially broader range of galaxy mass and redshift.

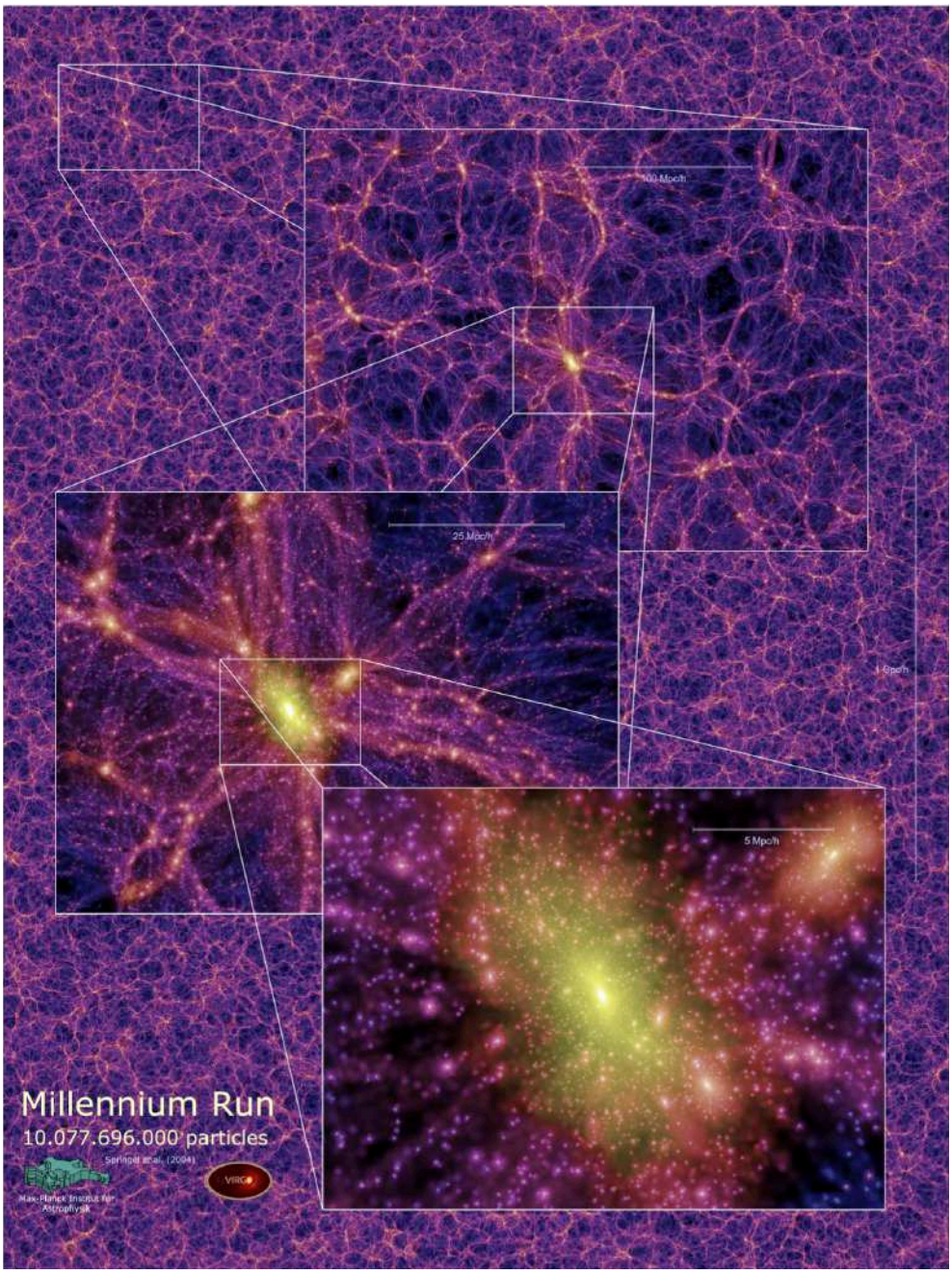

Figure 2.4: Poster of the Millenium Run taken from the Millenium Project. website Source: https://wwwmpa.mpa-garching.mpg.de/galform/virgo/millennium/

By 2012 a new simulation was presented, the Millenium XXL with 303×10^{10} particles to represent the formation of dark matter structures throughout a 4.1Gpc^3 box in a ΛCDM cosmology. The simulated volume of the MXXL is equivalent to that of the whole observable Universe up to redshift $z = 0.72$. It is more than 200 times that of the original Millennium Simulation (Angulo et al., 2012) and the particle mass ($m_p = 8.456 \times 10^9$) was seven times that of MS.

2.3.2 The Eagle Project

Eagle is a cosmological simulation performed also with a modified version of the N-Body Tree-PM smoothed particle hydrodynamics (SPH) code GADGET-3, which was last described in (Springel et al., 2005a). The main modifications are the formulation of SPH, the time stepping and, most importantly, the subgrid physics, which is based on that developed for OWLS (Schaye et al. 2010), and used also in GIMIC (Crain et al. 2009) and cosmo-OWLS (Le Brun et al. 2014). Detailed information of the subgrid physics implemented is presented by (Schaye et al., 2015). The biggest box in EAGLE is 100 Mpc^3 large while the rest are 50 and 25Mpc^3 in size. Table 2.1 lists box sizes and resolutions of the main simulations that ran till redshift $z = 0$.

Table 2.1: Box sized and resolutions of the main EAGLE simulations. The colums show from left to right: simulation box name; comoving box size; number of dark matter particles (equal to the initial number of baryons); initial baryonic particle mass; dark matter particle mass; comoving, Plummer-equivalent gravitational softening length; maximum proper softening length. Note that contrary to convention, box sizes, particles masses and gravitational softening lengths are not quoted in units of h^{-1}

.

Name	L [cMpc]	N	m_g [$M_\odot$]	m_{dm} [$M_\odot$]	ϵ_{com} [ckpc]	ϵ_{prop} [pkpc]
L025N0376	25	376^3	1.81×10^6	9.70×10^6	2.66	0.70
L025N0752	25	752^3	2.26×10^5	1.21×10^6	1.33	0.35
L050N0752	50	752^3	1.81×10^6	9.70×10^6	2.66	0.70
L100N1504	100	1504^3	1.81×10^6	9.70×10^6	2.66	0.70

Although a volume of 100 Mpc can contain many galaxy groups with $M_{200} = 10^{13} - 10^{14} M_\odot$, overdensities of the order of cluster mass ($M_{200} \geq 10^{15}$), are highly unlikely to be found in such a small box. Thus, it is difficult to evaluate the ability of these boxes to reproduce the physics of galaxies in a full range of environments.

Motivated by the limitations of their boxes, the Eagle team released a set of cosmological zoom simulations, called the Virgo Consortium Cluster-Eagle (c-eagle) project. This

simulation suite consists of zoom simulations centered in the formation of 30 galaxy clusters that lie evenly spaced in the mass range $10^{14} - 10^{15.4}\mathrm{M}_{\odot}$. This simulations allow them to probe environments that are not present in the original periodic EAGLE volumes presented in (Crain et al., 2015; Schaye et al., 2015).

These zoomed boxes are run using the standard eagle formation model (AGNdT9 calibration) and adopt the same mass resolution ($m_{gas} = 1.81 \times 10^6 \mathrm{M}_{\odot}$) and spatial resolution ($\epsilon = 0.7$ kpc) as the largest periodic volume of the eagle suite (L100N1504). The resolution of these zoomed Lagrangian regions allows to resolve the formation of galaxy clusters and the co-evolution with the ICM, as well as the formation of structures within the ICM and some of the energetic processes that shape it. To capture possible environmental effects on the clusters, the zoom regions extend around five times the virial radius of each object.

2.3.3 Horizon-AGN

Horizon-AGN is a cosmological hydro-dynamical simulation that employs the adaptive mesh refinement Eulerian hydrodynamics code, RAMSES (Teyssier, 2002). The details of Horizon-AGN , which we only briefly describe here, can be found in Dubois et al. (2012) and Dubois et al. (2014). The Horizon-AGN simulation is run in a $L_{box} = 100h^1$ Mpc cube with a cosmology with total matter density $\Omega_m = 0.272$, dark energy density $\Omega_{\Lambda} = 0.728$, amplitude of the matter power spectrum $\sigma_8 = 0.81$, baryon density $\Omega_b = 0.045$, Hubble constant $H_0 = 70.4 kms^{-1}$ Mpc^{-1}, and $n_s = 0.967$ compatible with the 7-year Wilkinson Microwave Anisotropy Probe data (Komatsu et al., 2011). The total volume contains 1024^3 DM particles, corresponding to a DM mass resolution of $M_{DM,res} = 8 \times 10^7 \mathrm{M}_{\odot}$, and initial gas resolution of $M_{gas,res} = 1 \times 10^7 \mathrm{M}_{\odot}$.

Even if the size of their boxes (~ 100 Mpc) is too small to have a valuable statistical sample of galaxy clusters, Horizon-AGN has interesting proposals specially in the treatement of AGNs, where they recently developed a unimodal model of AGN feedback instead of the unusually used bimodal approach. They have published various studies on the treatment of the subgrid physics for AGN feedback and how the presence of AGNs changes the morphology and evolution of galaxies and the ISM (for further information the reader may check Dubois et al. (2016) and Kaviraj et al. (2017).

2.3.4 IllustrisTNG

The illustrisTNG (Illustris The Next Generation) project is the successor of the original Illustris simulation (Genel et al., 2014; Sijacki et al., 2015; Vogelsberger et al., 2014) and its associated galaxy formation model (Vogelsberger et al., 2013; Torrey et al., 2014; Torrey et al., 2015). It is composed of three simulations run with the AREPO code (Springel, 2010), which employs a tree-PM algorithm to solve Poisson's equation for gravity and a second-order accurate Eulerian finite-volume Godunov scheme on a moving, unstructured

Voronoi-mesh for the equations of ideal magneto-hydrodynamics. The runs start from initial conditions adjusted to the Planck 2015 results ($\Omega_{\Lambda,0} = 0.6911, \Omega_{m,0} = 0.3089, \Omega_{b,0} = 0.0486, \sigma_8 = 0.8159, n_s = 0.9667$ and $h = 0.6774$ [4]; at $z = 127$ till today.

The three simulation volumes TNG50, TNG100, TNG300 were publicly released and introduced in a series of presentation papers (Marinacci et al., 2018; Naiman et al., 2018; Pillepich et al., 2018; Springel et al., 2018; Nelson et al., 2019a,b). Updates in the TNG model with respect to the original Illustris are among others the incorporation of a renovated galaxy formation model, which includes new physics and numerical improvements, as well as refinements to the original model, like the inclusion of a treatment of cosmic magnetism, following the amplification and dynamical impact of magnetic fields.

The three boxes try to complement each other by enabling studies of various aspects of galaxy formation. TNG300 covers a volume of 300 Mpc^3, and being the largest volume in the project is targeted to study rare and massive objects such as galaxy clusters. Thanks to its volume it also provides the largest statistical galaxy sample in IllustrisTNG.

TNG50 covers only 50 Mpc^2 but enables a mass resolution a hundred times better than the one in TNG300 by using 160^3 gas cells, with a corresponding baryon mass of $8 \times 10^4 \mathrm{M}_\odot$. It is focused on providing a thorough view of structural properties of galaxies, and small scale phenomena inside galaxies and their surroundings. Particularly, it is claimed to contain roughly 100 pseudo Milky Way mass-analogs and one massive galaxy cluster with a mass - $10^{14}\mathrm{M}_\odot$, a Virgo-like analog, and some group sized halos at $10^{13}\mathrm{M}_\odot$.

The TNG100 simulation is in the middle of both; it has a volume of 100 Mpc^3 and is targeted to study intermediate mass halos. It uses the same conditions as the original Illustris simulation (aside from a small shift in the adopted cosmological parameters), and is supposed to serve as a comparison between the original Illustris (which has been thoroughly studied) and the updated TNG model.

For each of the three volumes there are various resolution levels, three for TNG100 and TNG300 and four for TNG50. The highest resolution realizations, TNG50-1, TNG100-1 and TNG300-1, include $2 \times 21603, 2 \times 18203$ and 2×25003 resolution elements, respectively. As shown in table 2.2, the TNG300 run is performed at a factor of 8 (2) lower in mass (spatial) resolution when compared to TNG100. These are the typical steps between two resolution levels in the IllustrisTNG project. Consequently, TNG100-2 is realized at the same resolution as TNG300, and TNG100-3 corresponds to TNG300-2.

Usually the Illustris team performs renormalizations in their simulations to adjust to changes supposedly coming from resolution effects. However, even with resolution renormalizations, each of the volumes has its limitations as well. For example, TNG300 is still

[4] Data extracted from the IllustrisTNG official webpage: https://www.tng-project.org/about/

Table 2.2: Box sizes and resolutions for each of the resolution levels of the three flagship TNG simulations. The columns show from left to right: simulation box name; comoving box size; number of dark matter particles (equal to the initial number of baryons); initial baryonic particle mass; dark matter particle mass; comoving, Plummer-equivalent gravitational softening length; maximum proper softening length.

Name	L [cMpc/h]	$N_{DM,GAS}$ –	m_g [$M_\odot/h$]	m_{dm} [$M_\odot/h$]	$\epsilon^{z=0}_{DM,stars}$ [kpc]	$\epsilon_{gas,min}$ [ckpc/h]
TNG50(-1)	35	2160^3	5.7×10^4	3.1×10^5	0.29	0.05
TNG50-2	35	1080^3	4.6×10^5	2.5×10^6	0.58	0.1
TNG50-3	35	540^3	3.7×10^6	2.0×10^7	1.15	0.2
TNG50-4	35	270^3	2.9×10^7	1.6×10^8	2.30	0.4
TNG100(-1)	75	1820^3	9.4×10^5	5.1×10^6	0.74	0.125
TNG100-2	75	910^3	7.6×10^6	4.0×10^7	1.48	0.25
TNG100-3	75	455^3	6.0×10^7	3.2×10^8	2.95	0.5
TNG300(-1)	205	2500^3	7.6×10^6	4.0×10^7	1.48	0.25
TNG300-2	205	1250^3	5.9×10^7	3.2×10^8	2.95	0.5
TNG300-3	205	625^3	4.8×10^8	2.5×10^9	5.90	1.0

small for studying precision cosmology because it lies below the scale of BAO and also lacks statistics for halos of $M \sim 10^{15} M_\odot$. At the same time TNG50 is too low in resolution to resolve ultra faint dwarf galaxies with $M_\star < 10^5 M_\odot$, globular clusters, or small-scale galactic features such as nuclear star clusters.

2.3.5 Our Simulation Suites

2.3.5.1 The Magneticum Pathfinder Project

One of the largest cosmological simulations performed so far belongs to the Magneticum project (Hirschmann et al., 2014; Steinborn et al., 2016; Dolag et al., 2015; Teklu et al., 2015; Bocquet et al., 2016; Dolag et al., 2016; Remus et al., 2017; Bellstedt et al., 2018; De Boni et al., 2018; Ragagnin et al., 2019; Singh et al., 2020; Galárraga-Espinosa et al., 2020; Ragagnin et al., 2021; Biffi et al., 2021). This simulation set follows the evolution of up to 2×10^{11} particles of dark matter, gas, stars and black holes in a series of cosmological boxes that range in size from 50Mpc^3 to 4Gpc^3.

The simulations were performed with an extended version of the N-body/SPH code GADGET3, which is an update of the aformentioned GADGET-2. GADGET3 uses an improved Smoothed Particle Hydrodynamics (SPH) solver for the hydrodynamic evolution of gas particles presented in the paper by Beck et al. (2015). A complete explanation of the treatment of radiative cooling, heating, ultraviolet (UV) back-ground, star formation and stellar feedback processes can be found in Springel (2005). An overview of the im-

plementation of radiative cooling, stellar and AGN feedback is presented in appendix B . Cooling follows 11 chemical elements (H,He,C,N,O,Ne,Mg,Si,S,Ca,Fe) using the publicly available CLOUDY photo-ionisation code (Ferland et al., 1998). A detailed description of BH seeding and growth and some further details on AGN feedback can be found in Hirschmann et al. (2014).

Galaxy haloes and sub-haloes are identified using a version of SUBFIND Springel et al. (2001a), adapted by Dolag et al. (2009) to include the baryon component. This SUBFIND version additionally computes the values of M_{200} and M_{500} that are used in this work. The boxes belonging to Magneticum assume a cosmological model in agreement with WMAP7 results Komatsu et al. (2011), with parameters, $\Omega_{m,0} = 0.272$, $H_0 = 70.4 kms^{-1}km^{-1}$, $n = 0.963$, $\sigma_8 = 0.809$ and a baryonic fraction of 16.8%.

An overview of the different Magneticum simulations is presented in table 2.3. In this work in particular we used Box0/mr to follow the most massive haloes ($M \geq 10^{15}\mathrm{M}_{\odot}$), Box2b/hr to follow haloes within an intermediate mass range ($10^{13}\mathrm{M}_{\odot} \leq M \leq 10^{15}\mathrm{M}_{\odot}$) and Box4/uhr to follow haloes with masses in the galaxy range ($5 \times 10^{10}\mathrm{M}_{\odot} \leq M \leq 10^{13}\mathrm{M}_{\odot}$). A general overview of the different boxes in the Magneticum simulation is presented in figure 2.5. Figure 2.6 shows a visualisation of the second largest cosmological simulation (Box2b/hr).

The detailed description of baryon physics in Magneticum simulations is capable of matching several observed properties of galaxies and their haloes. Some examples are the specific angular momentum for different morphologies (Teklu et al., 2015); the mass-size relation (Remus et al., 2017; van de Sande et al., 2018); the dark matter fraction (see figure 3 in the paper by Remus et al., 2017); the baryon conversion efficiency; kinematical observations of early-type galaxies (Schulze et al., 2018); the inner slope of the total matter density profile (see figure 7 in the paper by Bellstedt et al., 2018), the ellipticity and velocity over velocity dispersion ratio (van de Sande et al., 2018), among many others.

The Magneticum Project has been used extensively also to help interpreting observational results, like the SZ data from PLANCK (Planck Collaboration et al., 2014) and SPT (McDonald et al., 2014) and to predict cluster properties from mock X-ray emission for future projects such as Athena and Astro-H (Biffi et al., 2012). The Magneticum boxes have been also used to produce the first mock observations for the eRosita cluster working group and the Athena+ white book. Other important achievements are related to the study of the properties of the ICM (Dolag et al., 2016) and the prediction of multi-wavelength properties of AGNs (Hirschmann et al., 2014; Steinborn et al., 2016).

The careful treatement of all relevant physical processes enabled the morphological classification of galaxies and the first study of their dynamical properties according to their shape Teklu et al. (2015). The enormous dynamical range available thanks to the combination of various resolution levels and cosmological volumes has helped with calibrating

the cosmological function based on hydro-dynamical simulations to the high level required by future cosmological probes (Bocquet et al., 2016).

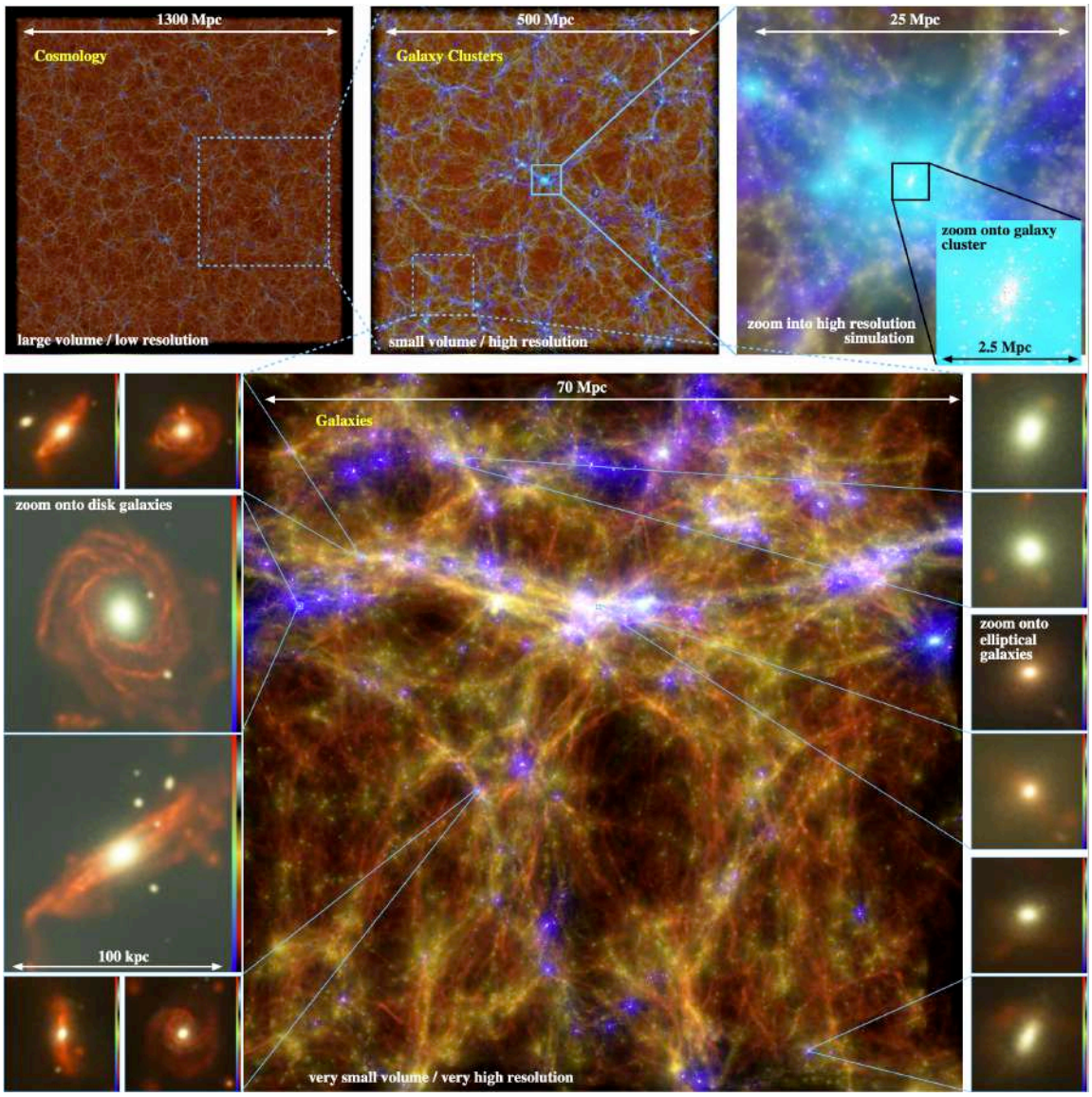

Figure 2.5: Overview of the different boxes in the Magneticum Pathfinder project, going from Gpc scales into galaxy clusters at Mpc scales and further till kpc scales to visualize cluster galaxies

.Source: http://www.magneticum.org/media.html

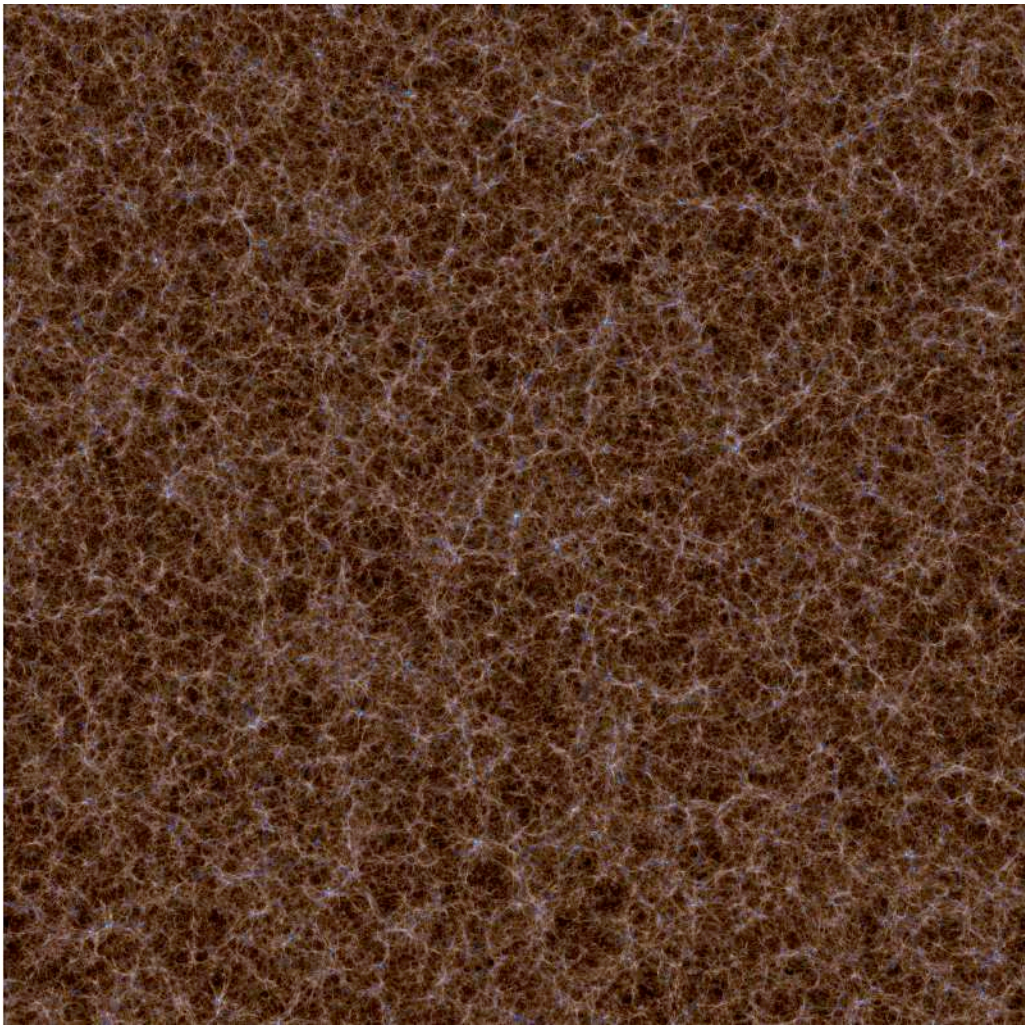

Figure 2.6: Visualization of Box0/mr from the Magneticum simulation set. The region in the picture spans a total length of 3800 Mpc, and contains (at $z = 0$) a total number of 1.86×10^{11} dark matter, gas, star and BH particles. In the picture we observe the gas filling the space between galaxies, color coded according to its temperature (cold=brown, hot=light blue), together with the galaxies and stars forming in the simulations (color coded in white)
.Source: http://www.magneticum.org/media.html

The web portal [5] allows the user access to a subset of the full Magneticum Simulation Set. In the data center 28 outputs of Box2/hr and the larger Box2b/hr (see table 2.3 for further details in the boxes) are available. For each cluster there are some useful pre-computed quantities available, that allow the user to select objects in commonly used categories, like fossils or compact objects.

[5] http://www.magneticum.org

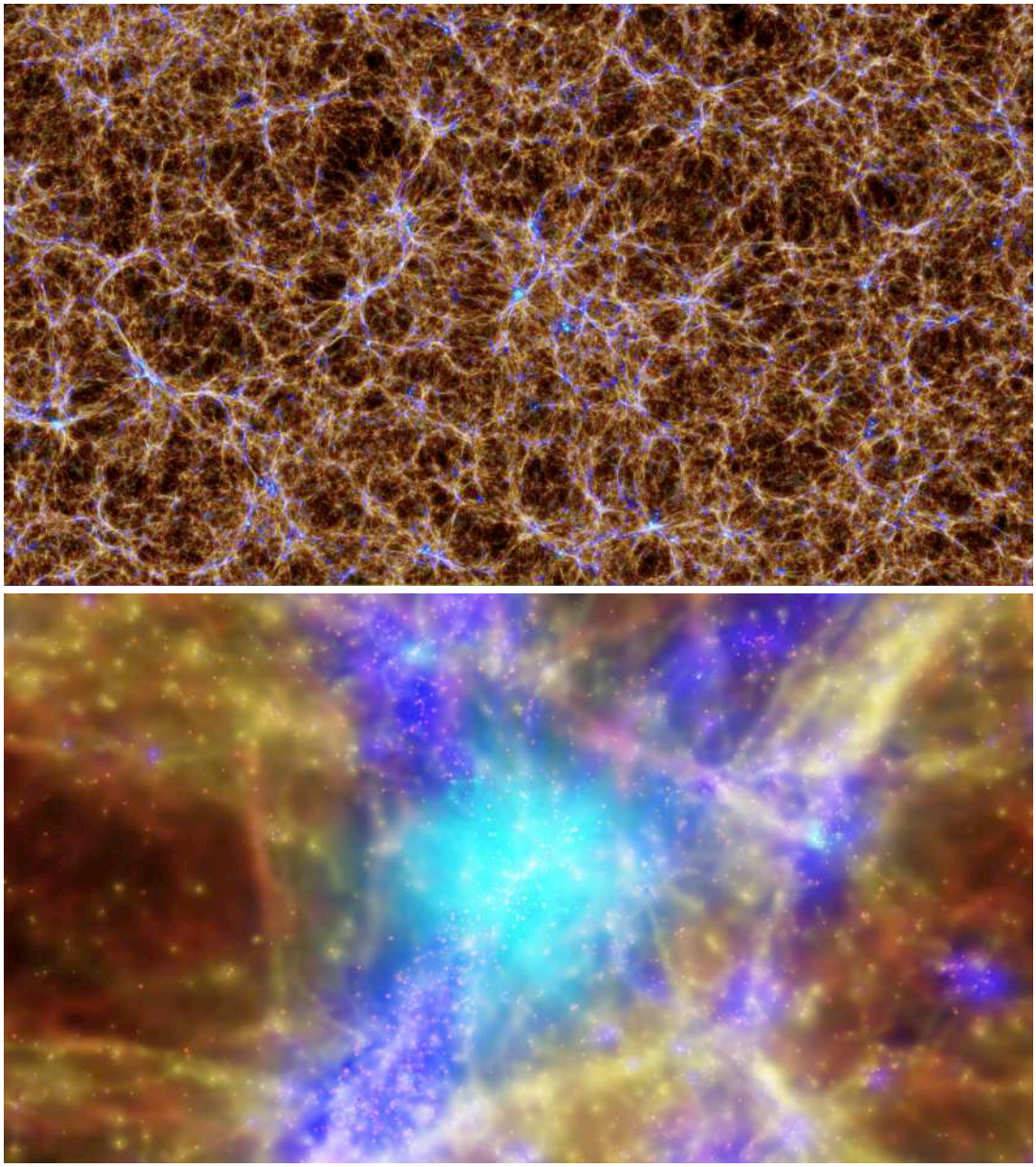

Figure 2.7: Visualizations of Box2b/hr from the Magneticum simulation set. The upper panel shows a region spanning a total length of 1000 Mpc. At $z = 0.2$ the region contains a total number of particles of 5.4×10^{10}, where we counted DM, gas, star and BH particles. Visualized is the gas that fills the space between galaxies, color coded according to temperature (cold=brown, hot=light blue), and galaxies and star-forming regions (colored in white). The lower panel shows a closeup look into the most massive cluster formed within the simulation.

Source: http://www.magneticum.org/media.html

Table 2.3: Set up of the three main Magneticum boxes used during this work. From left to right we find: the box size, the total number of particles, the mass of each dark matter particle, the initial mass of gas particles, the gravitational softening length of both dark matter and gas, and the gravitational softening length of star particles

.

Name	L [Mpc/h]	N	m_{dm} [$M_\odot/h$]	m_g [$M_\odot/h$]	$\epsilon_{DM,gas}$ [kpc/h]	$\epsilon_\star$ [kpc/h]
Box4/uhr	48	2×576^3	3.6×10^7	7.3×10^6	1.4	0.70
Box2b/hr	640	2×2880^3	6.9×10^8	1.4×10^8	3.75	2
Box0/mr	2688	2×4536^3	1.3×10^10	2.6×10^9	10	5

2.3.5.2 Dianoga and the Compass Set

Dianoga is a cosmological simulation carried out also with the SPH code GADGET-3 (Rasia et al., 2015; Planelles et al., 2017; Biffi et al., 2017; Biffi et al., 2018; Ragone-Figueroa et al., 2018; Bassini et al., 2020). It followed 1024^3 DM particles within a box of comoving side of $1h^{-1}$ Gpc, with h the Hubble constant in units of 100km s^{-1}Mpc^{-1}. The cosmological model assumed is a flat one, with $\Omega_m = 0.24$ for the matter density parameter, $\Omega_{bar} = 0.04$ for the contribution of baryons, $H_0 = 72 kms^{-1}$Mpc^{-1}for the present-day Hubble constant, $n_s = 0.96$ for the primordial spectral index and $\sigma_8 = 0.8$ for the normalization of the power spectrum.

Due to its big volume the Dianoga simulation contains various massive ($M_{200} \sim 10^{15} M_\odot$) galaxy clusters, which enable a meaningful theoretical study of these rare structures. From this cosmological box the 24 most massive clusters ($M_{200} \geq 8 \times 10^{14} h^{-1} M_\odot$) were selected together with 5, randomly chosen, smaller objects ($1 \times 10^{14} \leq M_{200} \leq 4 \times 10^{14} h^{-1} M_\odot$). These 29 Lagrangian regions where resimulated as zoom simulations, increasing mass resolution and adding the relevant high frequency modes of the power spectrum to build the appropriate initial conditions (see Tormen et al., 1997; Bonafede et al., 2011; Ferragamo et al., 2020) This set of resimulated massive galaxy clusters is what we call the Compass set.

Outside the highly resolved regions the masses of particles increase with increasing distance to the target halo, so that the computational effort is concentrated on the region of interest without missing environmental and large-scale tidal effects. We take special care in testing our simulations and shaping them in such a way that no low-resolution particles contaminate the central zoomed-in region as this can strongly disrupt the real shape of the highly resolved structures. We select a clean region of 5 virial radii so that the area is sufficiently large to contain more than one interesting non-contaminated massive halo.

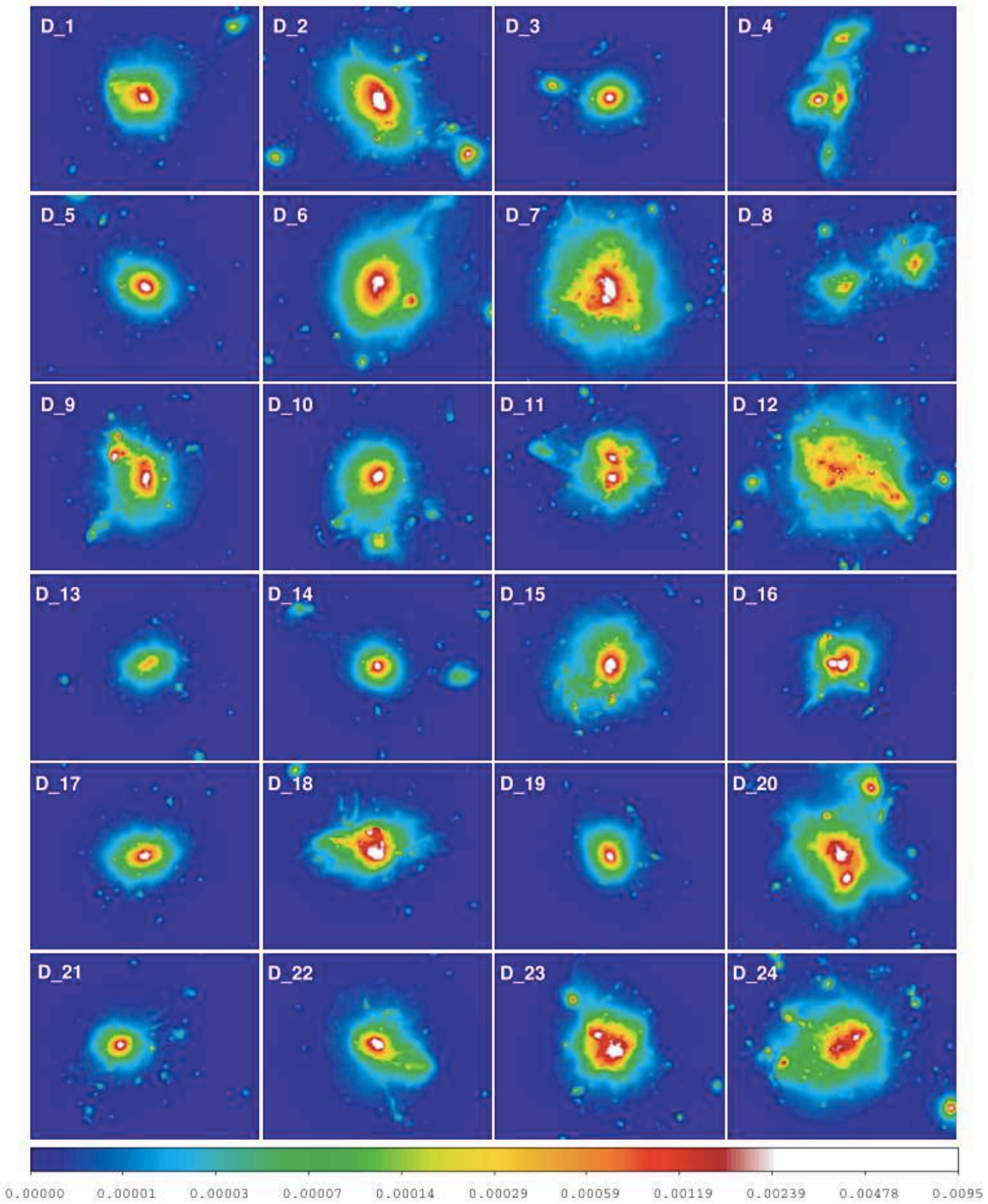

Figure 2.8: Visualization of the gas in 24 Lagrangian regions of the Compass set at $z = 0$. The gas is color coded according to the X-ray surface emission following the values of the color bar (Bonafede et al., 2011)

The initial conditions for the complete hydrodynamical simulations are generated by

splitting each DM particle within the high resolution region into two particles, one representing DM and the other representing the gas component, with a mass ratio that reproduces the cosmic baryon fraction. The mass of each DM particle is then $m_{DM} = 8.47 \times 10^8 h^{-1} \mathrm{M}_\odot$ and that of the gas particles is $m_{gas} = 1.53 \times 10^8 h^{-1} \mathrm{M}_\odot$. The simulations are then run using the GADGET-3 code just like the parent simulation. The gravitational force has an adaptive softening, with a Plummer-equivalent softening length fixed to $\epsilon = 5h^{-1}$ kpc in physical units for $z \leq 2$ and fixed in comoving units for $z \geq 2$.

One of the interesting features of these set is that these zoom simulations can be run with different prescriptions for the subgrid physics. The first set of hydrodynamical runs was performed with a simple prescription for star formation and for stellar feedback and with the gas radiative cooling model presented in section 2.1.5, equation 2.3. The second set of runs was performed adding a prescription for stellar evolution and a more complex stellar feedback that considered the two different types of supernovae and AGB yields (further details are presented by Dolag et al., 2017). Radiative cooling rates were computed by following the same procedure as presented by Wiersma et al. (2009). The contributions to cooling from each one of 16 elements (H, He, C, N, O, Ne, Mg, Si, S, Ca, Fe, Na, Al, Ar, Ni, Ej; where Ej stands for the sum of all metals that are not treated individually) were precomputed using the publicly available CLOUDY photoionization code (Ferland et al., 1998) for an optically-thin gas in (photoionization) equilibrium.

Table 2.4: Resolutions available for the Lagrangian regions of the Compass set with the corresponding DM masses and particles softenings

.

Resolution	m_{DM} [$\mathrm{M}_\odot/h$]	Particle Softening (gas, DM, stars, BH)
1x	8.3×10^8	3.75 / 11.25 / 1.0 / 1.0
10x	8.3×10^7	1.4 / 4.2 / 0.35 / 0.35
25x	8.3×10^7	1.0 / 1.0 / 0.25 / 0.25
250x	3.3×10^6	0.48 / 0.48 / 0.12 / 0.12
2500x	3.3×10^5	0.22 / 0.22 / 0.054 / 0.054

To provide a subresolution description of the interstellar medium, gas particles in regions above a certain density threshold are treated as multiphase as presented by Springel and Hernquist (2003). Stars of different masses, distributed according to a Chabrier initial mass function (Chabrier, 2003) release metals over a timescale that is determined by their mass-dependent lifetimes taken from Padovani and Matteucci (1993). Stellar feedback contributes to metal enrichment of the ICM by type Ia and type II SNe and low and intermediate mass stars (Tornatore et al., 2007). SNeII also contribute to the kinetic feedback according to the scheme presented by Springel and Hernquist (2003), where a star particle is assigned a probability to be uploaded in galactic outflows, which is proportional to its

star formation rate.

The third set of simulations adds on top of these prescriptions the effects of BH growth and AGN feedback. Following the current understading, where the released energy of AGNs results from the accretion of gas onto SMBHs, BHs in our simulations are described as sink particles, that grow in mass by accretion of gas or by merging with other BHs. The accretion of gas proceeds at the Bondi rate, and is artificially capped by the Eddington-rate. Our AGN model is bimodal, having an efficiency of $\epsilon_f = 0.1$ in the 'radio' mode and $\epsilon_f = 0.4$ when the AGN enters the quasar' mode (e.g. Sijacki et al., 2007; Fabjan et al., 2010b). The energy radiated by the BH corresponds to a fraction of the rest-mass energy of the gas accreted, and consequently when radiating the mass of the BH decreases by the corresponding amount. A more detailed mathematical description of the subgrid physics of the Compass Set can be found in appendix B. The identification of structures and their tracking through different outputs proceeds identically as with the Magneticum Project with the use of the halo finder SUBFIND (Springel et al., 2001b; Dolag et al., 2009) and the building of merger trees.

One of the main advantages of zoom simulations compared to full cosmological boxes is that zoom simulations can be resimulated at increasing resolutions using reasonable time and computational resources. Being 1x the resolution of the parent simulation DIANOGA the simulations can be rerun at 10x, 25x, 250x and 2500x times the original resolution. A detailed description of resolutions, DM masses and particle softenings can be found in table C.1.

During this work we performed a first thorough study of the Lagrangian regions belonging to the Compass Set at 1x resolution with different physical prescriptions, analyzing the possible effect of our subgrid physics on the evolution of the cluster and protocluster population as well as in the galaxy properties and SFR at high redshifts.

Chapter 3

Results

3.1 Structure and Evolution of a Simulated Cluster

If we want to study the evolution of simulated galaxy clusters through time, we need to be able to identify the structures we are interested in and then associate the final structure with the material that merged or was accreted to form it. In the following section we will explore the cluster morphology from its protocluster stage to its final virialization, and we will discuss some of the problems that can arise when trying to identify these structures in simulations.

3.1.1 General Cluster Morphology

In figure 3.1 we see the x-y projection of the evolution of the dark matter component of a protocluster at $z \sim 5$ evolving into a massive galaxy cluster of $M \sim 10^{15}$ $M_\odot$ at $z \sim 0$, where we excluded from the plot all particles that will not be part of the final structure. The overdensities identified by the halo finder SUBFIND are sign-posed in green, with the number corresponding to their ranking in virial mass calculated with the Spherical Overdensity method.

At $z \sim 5$ we encounter a structure that lacks the presence of a massive virialized halo. Instead, matter is arranged forming a web with filaments and nodes, on which the most massive overdensities sit. This is already the protocluster stage of the collapse. Overdensities accrete from the filaments growing in mass, so that at $z \sim 3$ we see denser nodes and a much more pronounced filamentary structure. At $z \sim 2$ the most dominant structures have already formed. The blue and green circles show an estimate of the corresponding R_{200} and R_{vir} performed by SUBFIND. These overdensities will continue growing by accreting from the surroundings and some of them will even suffer mergers with the overdensities that encircle them. This way, we encounter very outstanding overdensities at $z \sim 1$, two of which will suffer a major merger before $z \sim 0.5$. All three remaining halos will merge forming a single massive overdensity already at $z \sim 0.25$.

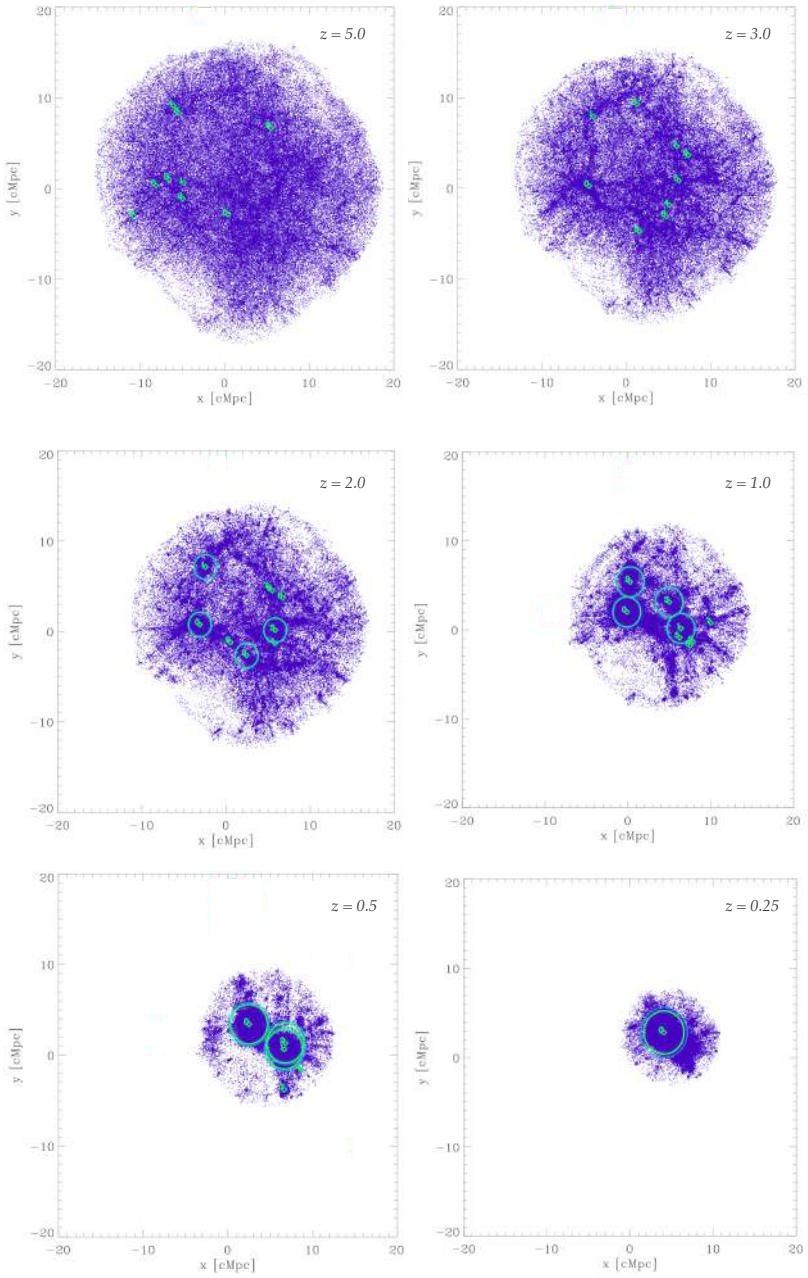

Figure 3.1: x-y projections of the evolution of the dark matter component of the protocluster in the Compass Lagrangian region g7358274 from $z = 5$ till $z = 0.25$. All particles not belonging to the final cluster where excluded. The numbers sign-posed in green on top of the structure mark the overdensities identified by out halo finder SUBFIND. The upper panels show the filamentary structure of the protocluster, lacking any virialized massive halo as expected in the hierarchical structure formation at high redshifts. The middle panels show the formation of four bigger halos by accretion through filaments and by merges between small overdensities. The blue and green circles show R_{200} and R_{vir} from SUBFIND. In the third panel we see how some of the halos already merged and the ones remaining will merge before $z = 0.25$.

Figure 3.2 presents a closer look into the three projections of the Lagrangian region at $z \sim 0.5$. From the plots we can infer that the merging process took place in two steps, first with a major merger between halos 1 and 2 and finally with another merger between the resulting overdensity and halo 0.

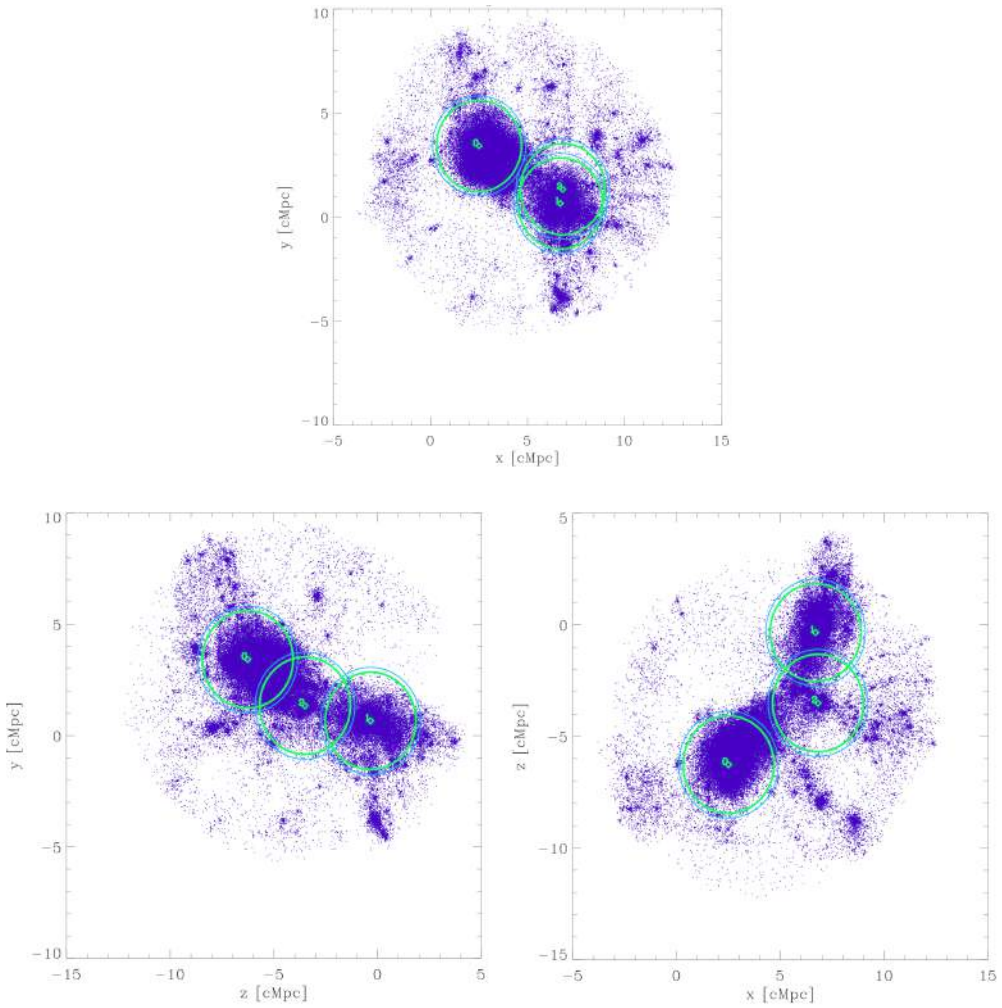

Figure 3.2: All three projection of the cluster region in g7358274 at $z = 0.5$. Due to the geometrical placement of the overdensities it seems plausible that the merging of took place first between halos 1 and 2 and finally with halo 0.

During this process of mergers and accretion the protocluster shrank from ~ 4.0cMpc to ~ 1.0cMpc and the virial mass of the most massive halo increased from 6.27×10^{13} $M_\odot$ at $z = 3.0$ to $1.138 \times 10^{15} M_\odot$ at $z = 0.5$. At even lower redshifts the large scale-structure surrounding the cluster appears to stabilize due to the increased expansion rate. At $z \approx 0$

we find a virialized galaxy cluster of $1.5 \times 10^{15} M_{\odot}$.

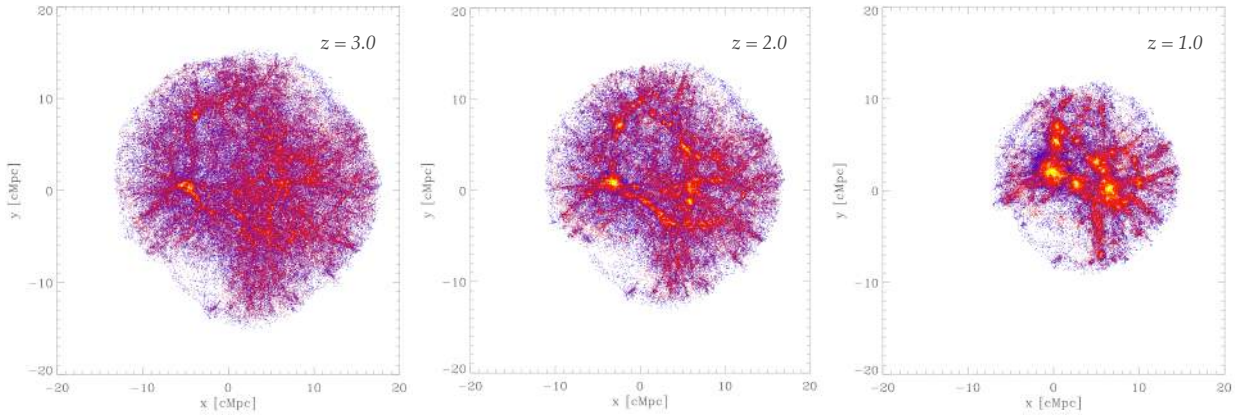

Figure 3.3: Evolution of the cluster in g7358274 as in figure 3.1 but with the gaseous (in red) and stellar (in yellow) components added on top. We can visualize how the baryonic component follows the DM potential wells already at high redshifts (see left panel), steepening the potential wells of DM. Gas clouds cool in overdense regions and thus stars are formed mainly in the nodes between crossing filaments.

When adding the gaseous component to a cluster, this will follow the DM structure early on (see figure 3.3), steepening the potential wells of DM (Borgani et al., 2002). Clearly, gravity dominates the evolution of all components of large scale structures. This explains how purely gravitational approaches, like the scaling relations presented by Kaiser in the 80s (Kaiser, 1986), have survived the pass of time reasonably well, even if we know that baryons are responsible for the breaking of these relations. During in-fall into the potential wells of DM, gas radiates and thus cools. If the density is high enough, gas clouds will collapse and form stars. Even if at $z \sim 3$ the amount of produced stars is still low, at $z \sim 2$ almost all remarkable overdensities have a non negligible number of stars in their core. This points to a high star formation rate at $z \sim 3 - 2$. At $z \sim 1$, it is clear that all the main halos have a high stellar content, thus we can expect that the resulting halo from the low redshift mergers will also have a reasonably high amount of stars.

In figure 3.4 we have a closer look at the evolution of the cluster at lower redshifts. In the first and second panels we see the structure of the main halo, which already has a central galaxy, i.e. a BCG, surrounded by satellites. This halo seems to be approached by another one, that being more poor only contains his own central galaxy. This central galaxy is surrounded by a smaller number of halos than its counterpart and dominates clearly the star formation. At $z \sim 0.1$ both halos have come closer together and the merging is imminent. Meanwhile in halo 0 the BCG continues growing through galactic cannibalism. If we look closely, we can observe how smaller satellites that surround the

BCG sink into the cluster center due to dynamical friction and tidal stripping. Finally, at $z \sim 0$ both halos collide. The central galaxy of the smaller halo passes through halo 0 producing a tidal arm that connects it with the BCG of the main halo. In the last panel of figure 3.4 we present the situation after the first passage, where the dark matter and gas content of the smaller structure, circled with a dotted line, have almost completely merged. The stellar content is stepping back again towards the center of the cluster and we can expect it to merge in the future with the central BCG.

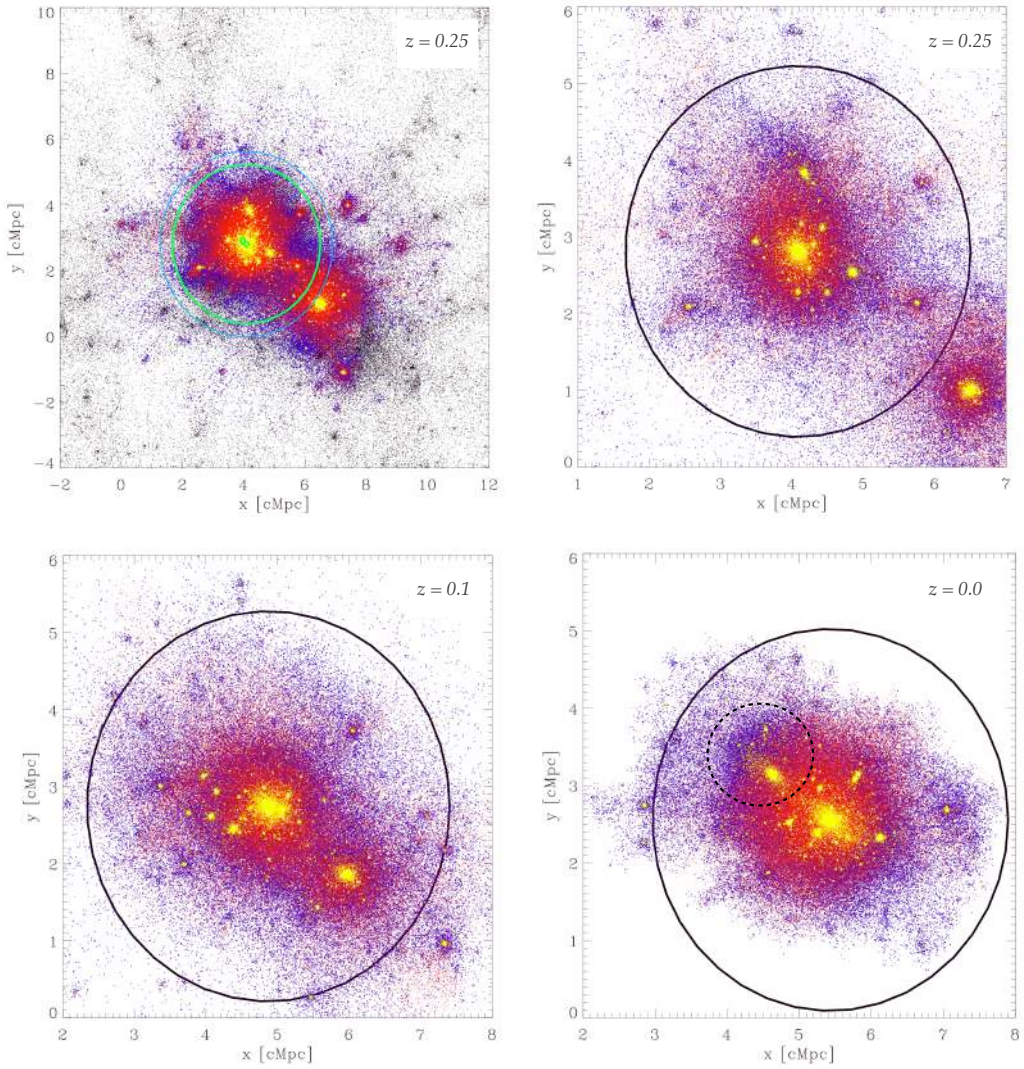

Figure 3.4: Closer look into the evolution of the cluster in g7358274 at low redshitfs, $0.25 \geq z \geq 0$. The upper panels show the structure of the main halo, with its R_{vir} and R_{200} plotted in the left figure as green (black in the right panel) and blue circles respectively. The lower panels show the merging event between two overdensities. After the crossing the approximate location of the smaller halo is circled with a dotted line.

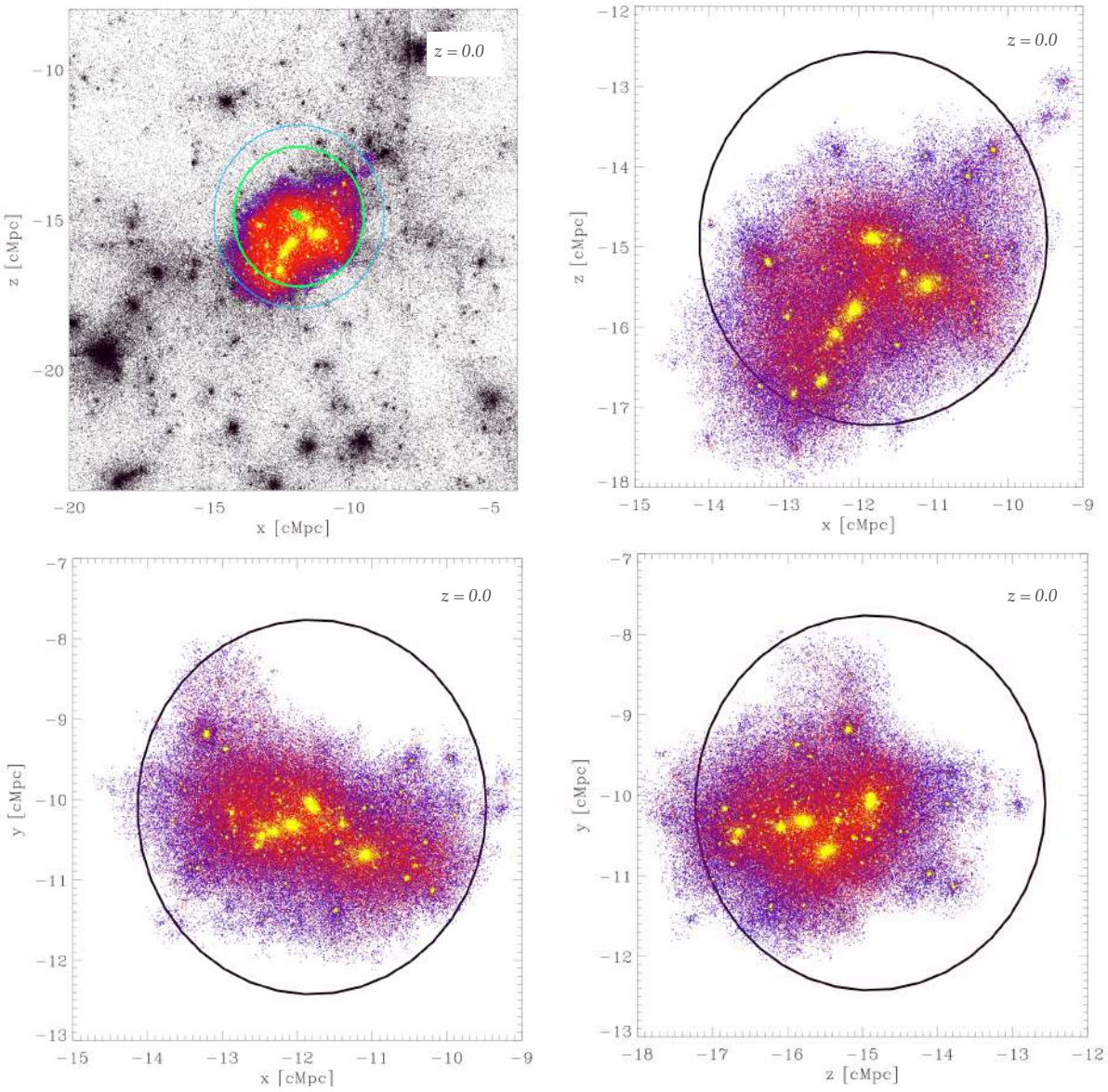

Figure 3.5: Projections of the internal structure of the main cluster in the region g1483463. In the upper left panel the green and blue circles represent R_{vir} and R_{200} as calculated by SUBFIND. In the rest of the figures the black circle stands for R_{vir}. The internal structure of this cluster does not show a dominating central galaxy but a chain of similar mass galaxies in the ranges $10^{11} - 10^{14}\mathrm{M}_{\odot}$. These are in turn surrounded by smaller satellite galaxies lying all over the cluster halo.

The final halo is a virialized structure with a central bright galaxy that most probably dominates star production (see section 3.3.3 for a more detailed discussion) and that, without further disturbances, is expected to slowly accrete its surrounding galaxies. However, this is not necessarily the case for all clusters of galaxies at low redshifts. As we mentioned

in the introduction, galaxy cluster evolution is a process that takes place at all redshifts, and thus we can find a wide variety of morphologies and internal dynamical structures. For example, the Lagrangian region g1483463 pictured in figure 3.5 lacks a dominant BCG at the cluster center. In turn, it contains a chain of galaxies of similar mass surrounded by smaller satellite galaxies all over the cluster. Similar to the case of the Virgo cluster (see figure 1.3), here we also have a cluster in assembly, that clearly cannot have reached virialization (see discussion in section 1.2)).

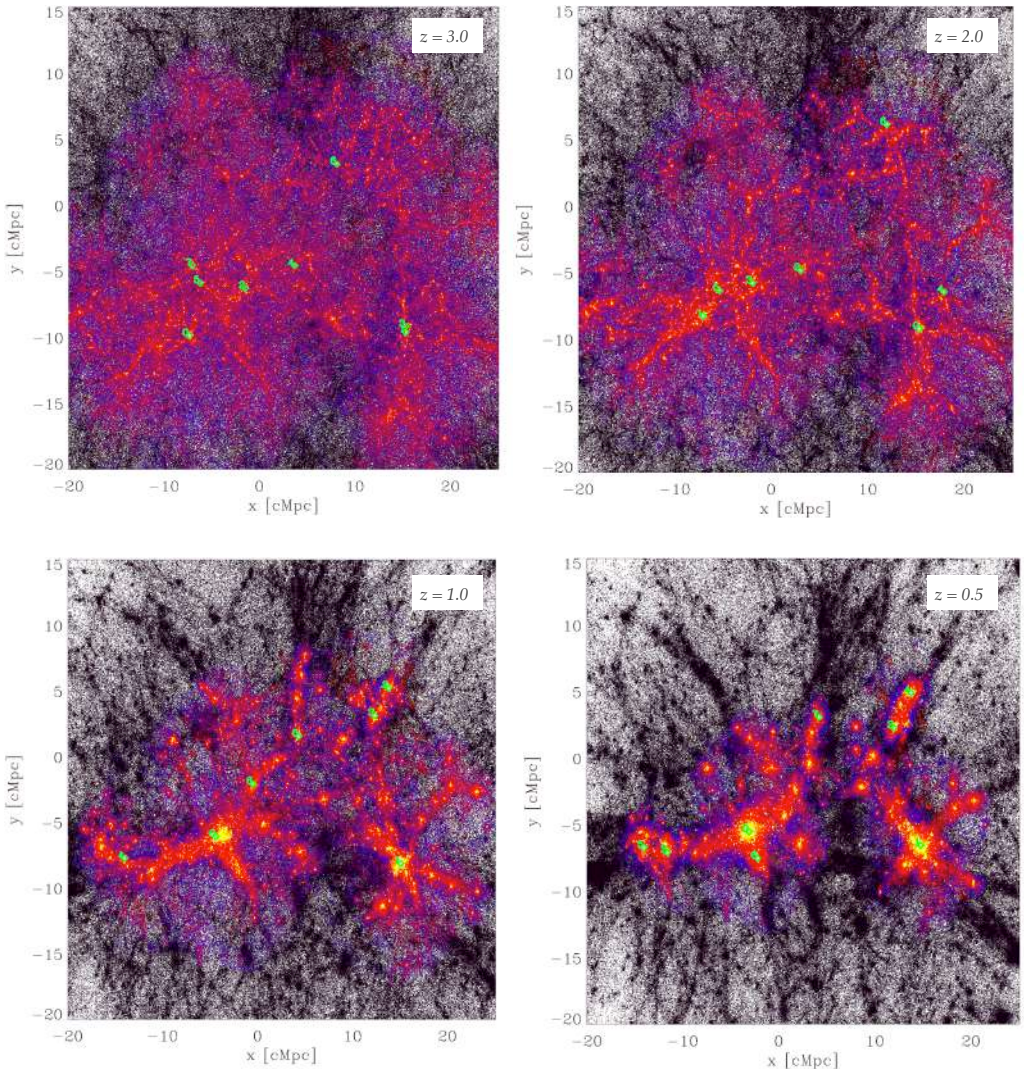

Figure 3.6: x-y projection of the Lagrangian region g7263961 from $z = 3.0 - 0.5$. DM particles belonging to the cluster are plotted in blue, while gas is plotted in red and stars in yellow. The background universe dark matter structure is plotted in black. The evolution of this region gives as a result a family of proto-clusters co-evolving in a volume of length ~ 40 cMpc.

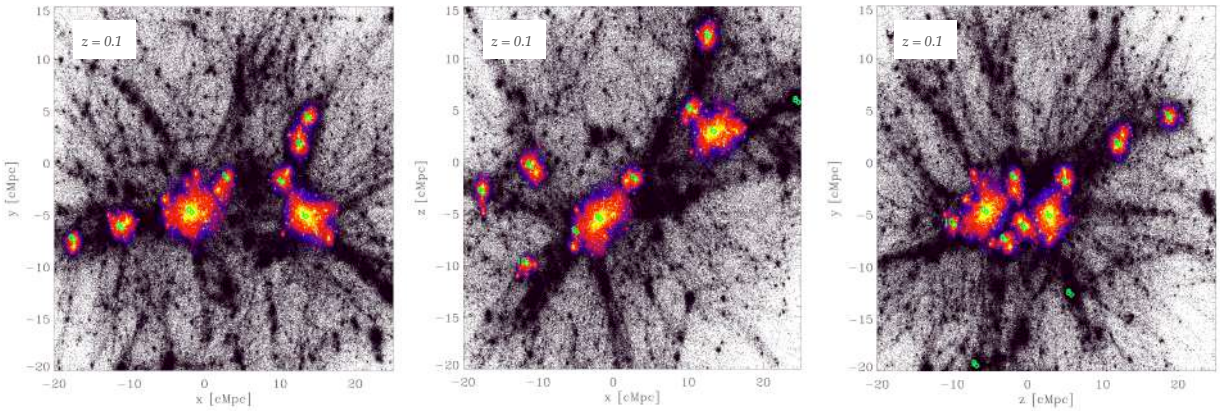

Figure 3.7: Projection of the clusters in region g7263961 at $z = 0.1$. The structures are already collapsed and compact although they are still connected by filaments and a future merger between clusters seems inevitable.

In the previous examples we showed clusters that evolve in isolation. Nevertheless, clusters may also evolve in a region surrounded by other clusters of similar masses. This is the case of the Lagrangian region g7263961 (see figures 3.6 and 3.7). Here the initial filamentary structure collapses into several co-evolving galaxy clusters with $10^{14}\mathrm{M}_{\odot} - 10^{15}$ $\mathrm{M}_{\odot}$ final masses. The filamentary accretion of clusters can be clearly seen in figure 3.6. The collapse of clusters is far away from spherical, it has a clear accretion path determined by the filamentary structure formed by DM at high redshifts and visible already at $z \sim 3$. At low redshifts the clusters coexist in an overdense environment, while still accreting from the surroundings through filaments, some of which have an extension of more than 10 cMpc. It is clear that in the hierarchical picture, cluster and galaxy growth departs strongly from spherical symmetry, showing very different geometries and internal configurations. This increases the complexity of this massive structures and makes them one of the most interesting building blocks of our Universe.

3.1.2 Possible Errors in SUBFIND

As was pointed out in section 2 of this work, SUBFIND is a very useful tool for the post-processing of data in cosmological simulations. Using the FoF and the SO methods, SUBFIND allows us to detect halos and to assign them corresponding masses and radii. However, as with any other simulation tool, we have to be careful with its blind spots, so that its errors do not drive us to unphysical conclusions. In the following, I will present different errors that we found in our current version of SUBFIND and different ways to detect them. Many of the errors were only observed in the parallel version of SUBFIND, thus even if tedious, it may be worth for the user to adjust the memory when post-processing so that SUBFIND runs in serial mode through all snapshot files. In any case, it is strongly recommendable to be conscious about the possible problems that may arise.

Maybe one of the most common and well known errors that SUBFIND may perpetrate in parallel as well as in serial mode, is the unification of two halos into one single structure (see figure 3.8). This error arises when two structures are close together prior to or in the process of merging. We can detect that this is happening by visual inspection of the Lagrangian region, or when plotting masses or radii of the structures through redshift. If suddenly a halo is identified as being part of another structure, we will see a sudden change in the cluster mass vs time relation that cannot be related to a physical merger, but is clearly a numerical artifact. An example of such a situation is shown in figure 3.9a. As this error is inherent to SUBFIND and the FoF method, there is not much that can be done about it. The user may try to circumvent the error by taking mass and radii estimates of other snaps or by jumping the affected snaps when building the merger tree (see figure 3.9b).

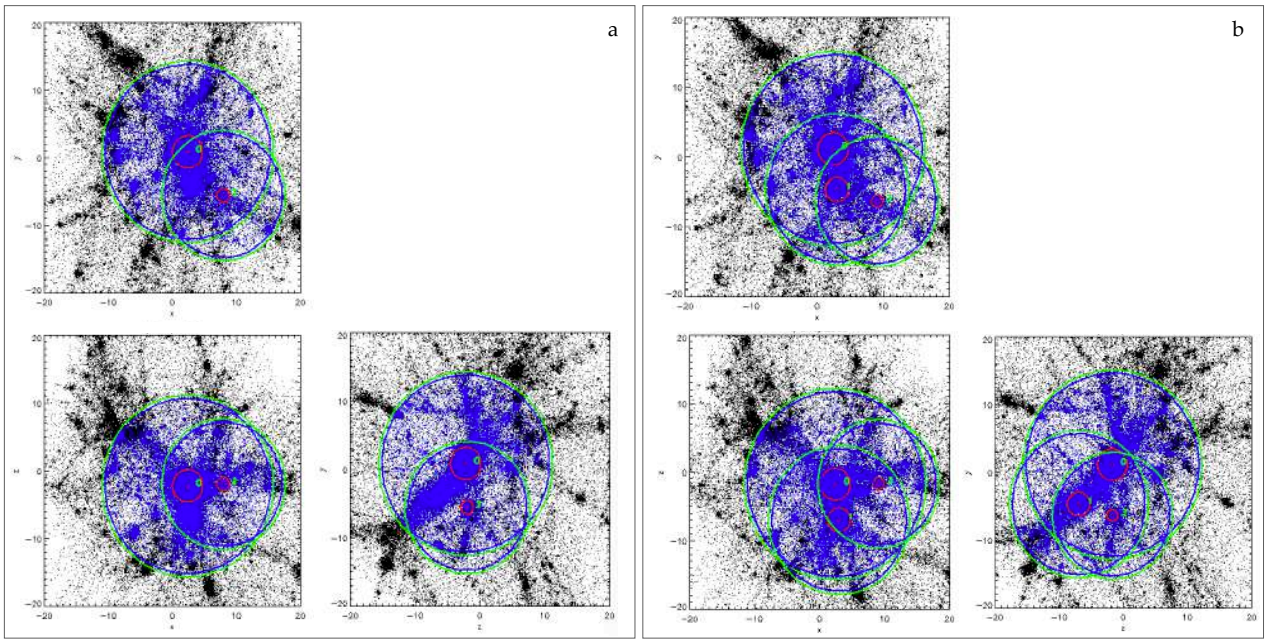

Figure 3.8: Visualization of the three clusters of region g1212639 with an erroneous cluster detection at the left and a correct cluster detection at the right. Due to the slow merger between halos 0 and 1, SUBFIND detects them as one single structure, taking for the center of the combined halo the position of the most massive bound particle in cluster 0. It assigned cluster masses and radii very similar to the ones of cluster 0 alone. The right panel shows the SUBFIND cluster detection one snapshot before, where it clearly detects three distinct halos.

Another error that we may encounter is the misidentification of the position, radius

and masses of halos. This problem was detected only when running SUBFIND in parallel and it was found to affect the most massive halos of several Lagrangian regions. We may have only detected this in the most massive halos because their larger masses and radii make the error more obvious or maybe because SUBFIND only makes this mistake in the deepest potential wells of the zoomed region. This can be seen though visual inspection (see figure 3.10), or when plotting mass quantities or radii through time. Although possible, it is uncommon that this error arises in all the subfiles of a simulation. Thus, we will have some files with reasonable masses for our halos, while other will have too low masses. Therefore, when plotting the evolution of stellar, gas or total masses through redshift we may encounter a wiggling similar to the one shown for the black line in figure 3.11.

The FoF group seems to be detected correctly, while the cluster center and its corresponding radius and mass are not. This may have to do with an error in the SO implementation of SUBFIND in parallel mode. A possibility would be that the most bound particle is not detected correctly and thus the radii and masses are estimated erroneously by the SO method. This error may be more difficult to detect in cases where we have a structure that for some reason has two deep potential wells (i.e., after a recent merger). In that case, the change in mass and radius will probably not be outstanding enough to result suspicious. The only way to detect this misidentification is by visual inspection. As an example we can see the panels presented in figure 3.12.

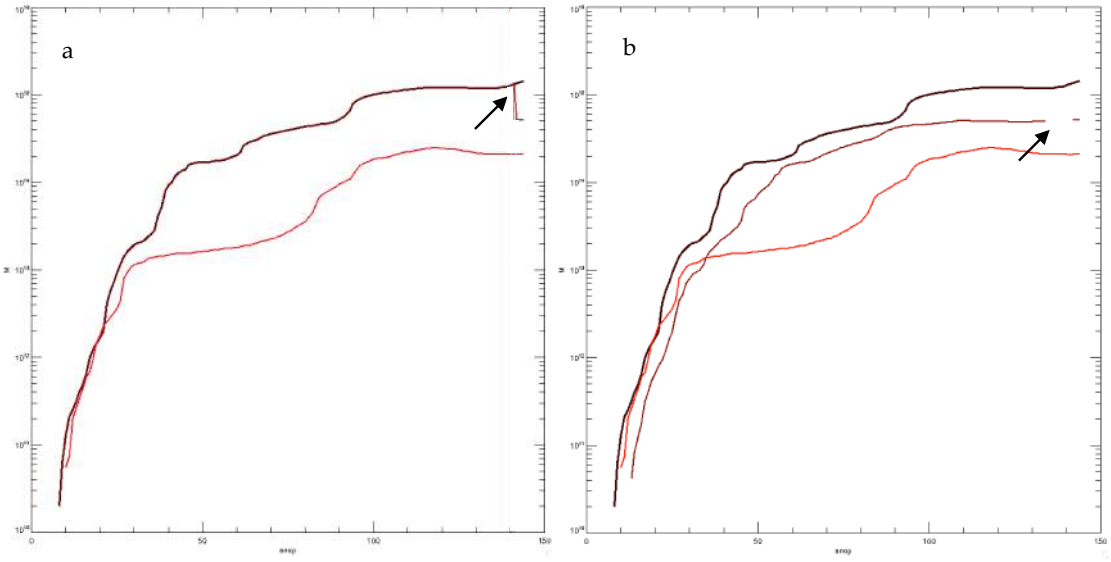

Figure 3.9: Visualization of the mass evolution of three halos through the different simulation snapshots. In the left panel we see a sudden unphysical jump in the mass of halo 1 towards the mass of halo 0. This mass history was calculated wrongly by the merger tree due to a previous miss-identification of SUBFIND. In the right panel we show the result of jumping the affected snapshots when walking the tree.

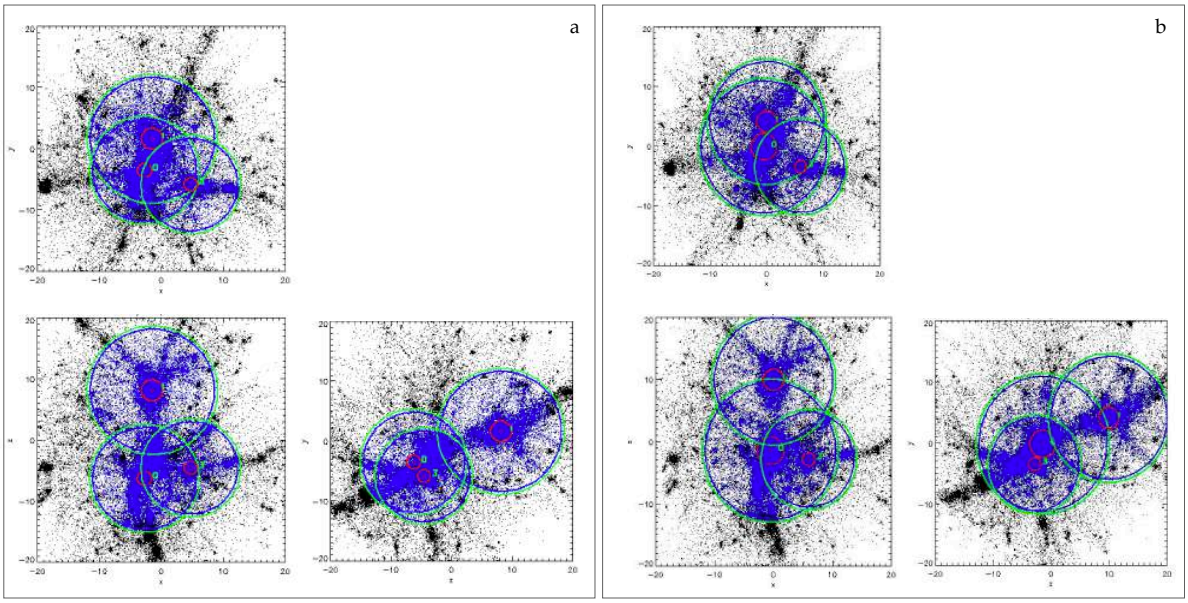

Figure 3.10: Left and right panels show the three projections of the same Lagrangian region at same redshift, but with a wrong and a correct halo position identification of the most massive cluster. The corresponding radius and mass of the cluster is also affected by this error.

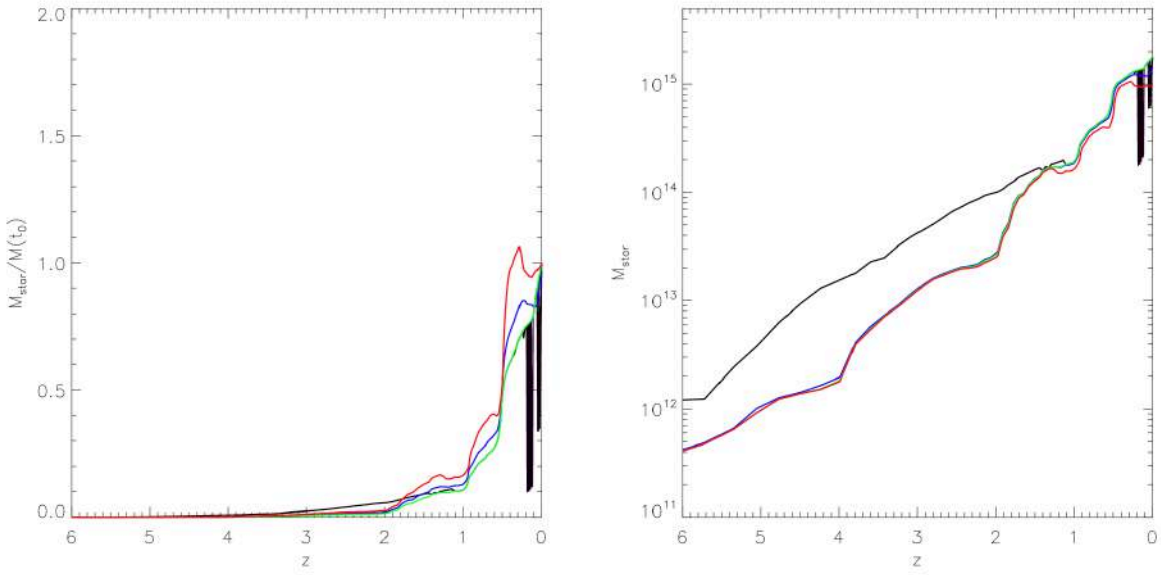

Figure 3.11: Normalized (left panel) and total (right panel) stellar mass evolution through redshift. The most massive halo (black line) suffers a wiggling due to the miss-identification of the halo center and consequently underestimation of its radius and mass.

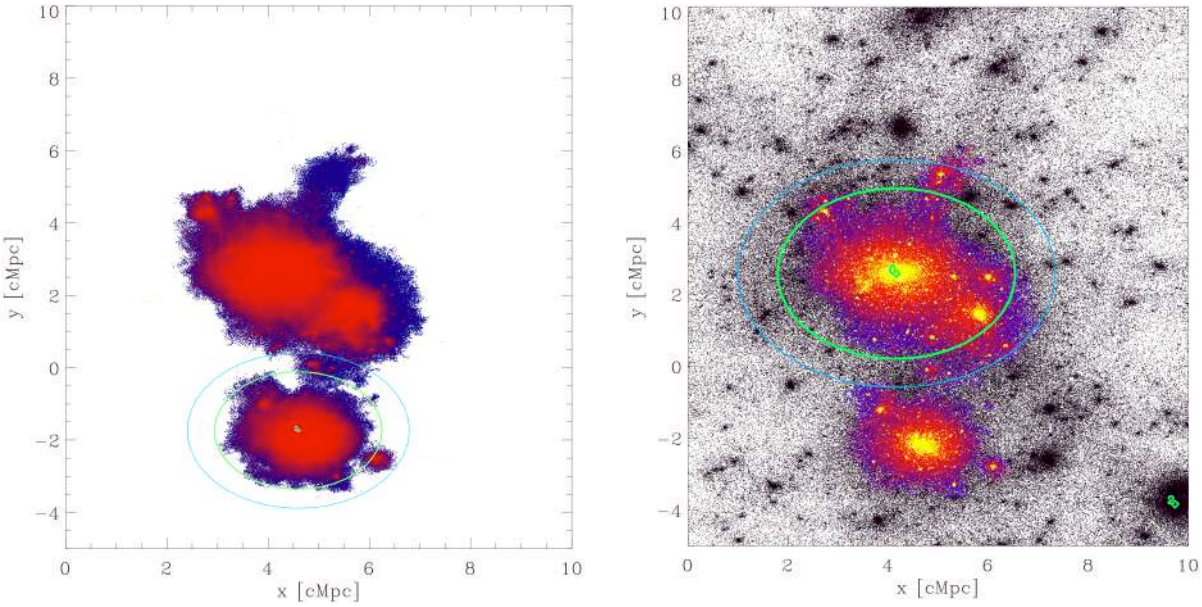

Figure 3.12: Misidentification of the center of a halo in the process of merging with another massive structure. As the masses and radii of both overdensities are of the same order of magnitude, the error can get overlooked unless we perform a visual inspection.

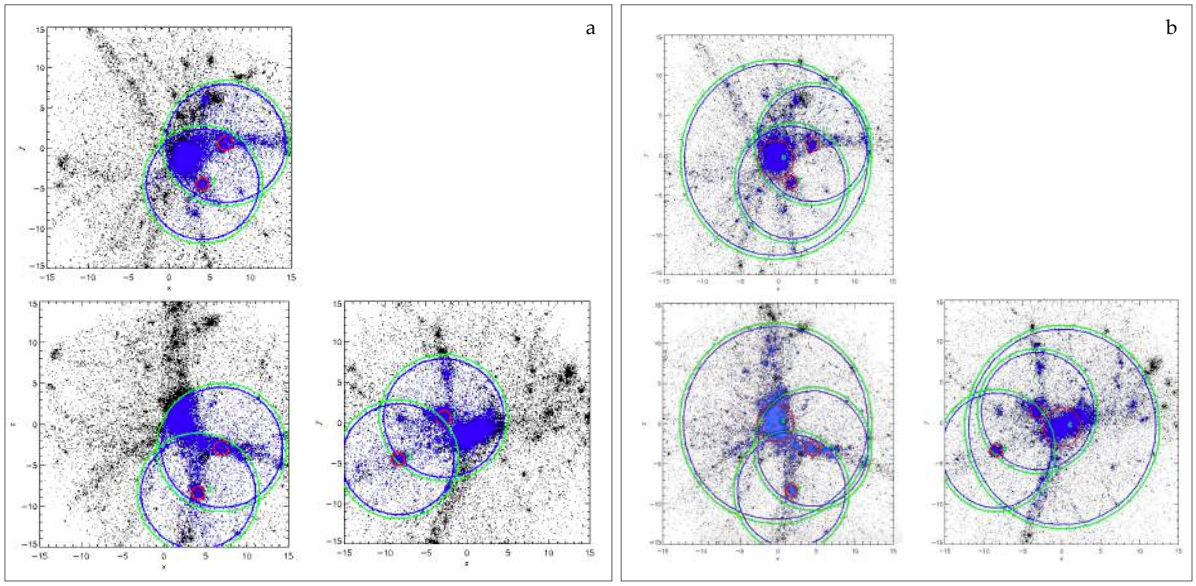

Figure 3.13: Both panels show the same Lagrangian region at same redshift. In the figure at the right SUBFIND was runned in serial mode and detected the three main overdensities. In the left panel we runned SUBFIND in parallel mode and it ignored the existence of the most massive halo.

An even worse situation arises when SUBFIND does not detect the existence of a halo at all (see figure 3.13). Again, this error was detected only in the parallel version and seemed to affect solely the most massive halo in the Lagrangian regions. In this case, there were no particles assigned to this structure and also no radii or masses available. The reason for this behaviour is unknown. The only solution found to this problem in the time of submission of this work is forcing SUBFIND to run in serial mode.

3.1.3 Following a cluster evolution through time: Merger Trees

The construction of merger trees is fundamental to relate our simulated galaxy clusters with their progenitors at high redshifts, and thus being able to have an accurate description of their forming history. To study the mass evolution of our clusters we looked at the main branch of the cluster, i.e. the lineage with the highest cumulative mass. To do so, we used first the pointer 'first progenitor' that brings us to one of the progenitor substructures (but not necessarily the most massive one) and then the pointer 'first halo in FoF group', that carries us to the most massive of these progenitor subhalos. By doing this, we can keep track of the mass history of the clusters in our simulations.

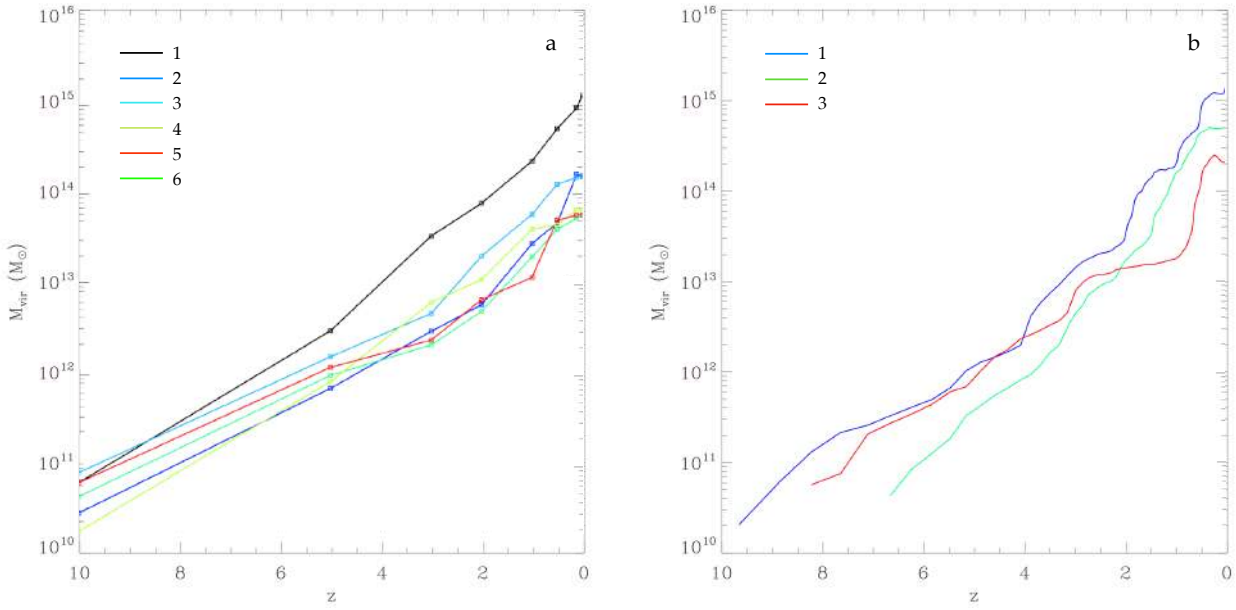

Figure 3.14: Evolution of virial masses through redshifts for the clusters in the Lagrangian regions g0272097 (left panel) and g1212639 (right panel). In both figures we observe several surpassings between halos. Some protoclusters with a higher mass rank at high redshifts end up as clusters with a lower mass rank at lower redshifts. Examples are halos 3 and 5 in the left panel and halos 1 and 2 in the right panel.

For example, figure 3.14 shows the virial mass evolution of the six galaxy clusters in region g0272097 and the three galaxy clusters in region g1212639. Interestingly, we observe how structures do not necessarily grow in a completely hierarchical way, meaning that massive protoclusters at high redshifts may end with a lower mass at $z \sim 0$ than their originally less massive counterparts, and viceversa. This happens i.e., for clusters 3 and 5 in figure 3.14a and for cluster 3 in figure 3.14b.

With our merger trees we can also study the merging and accretion histories of each of the clusters in our zoomed Lagrangian regions. For example, figure 3.16 presents the evolution of the most massive halo of region g1212639 at $z = 0$ ($M = 1.5 \times 10^{15} \mathrm{M}_{\odot}$). Each of the points represents an overdensity of certain mass. The displacement of the points at each redshift shows the mass growth of the corresponding structure due to the events happening in the previous redshift plotted. This tree in particular shows a major merger at high redshifts between two small halos and a posterior more massive major merger that establishes the lower redshift structure of the cluster, which will continue growing in mass by accretion of the surrounding small overdensities and remaining material.

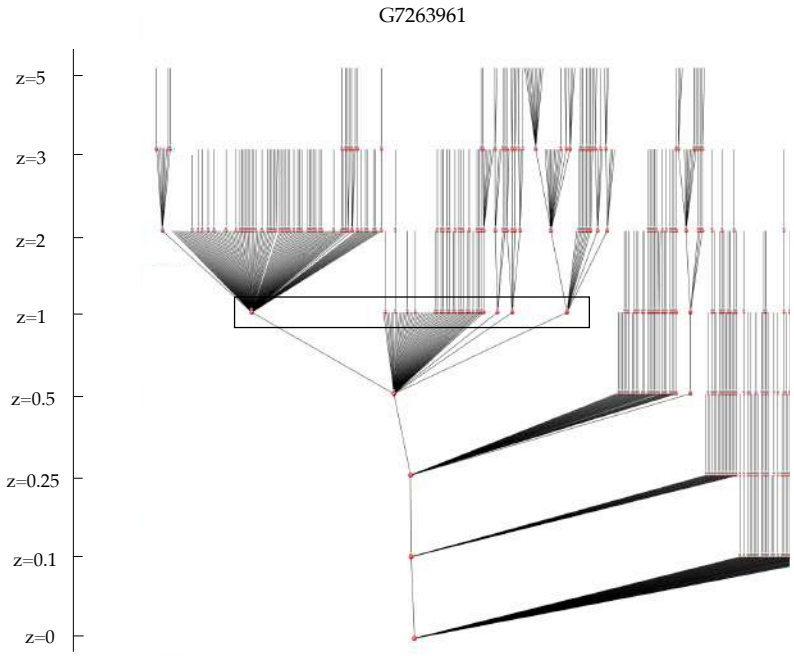

Figure 3.15: Merger tree of the most massive final halo in region g7263961. The rectangle points to a major merger between two halos happening simultaneously to a couple of minor mergers, all before $z \sim 0.5$. Afterwards the structure grows mainly by accretion although some further minor merges are also present.

Something similar happens with the most massive cluster in g7263961 ($M = 1.6 \times$

$10^{15}M_{\odot}$; see figure 3.15) that suffers a main major merger at $z = 0.5$ happening together with two minor mergers. For the second most massive cluster in that Lagrangian region (see figure 3.17; $M \sim 1 \times 10^{14}M_{\odot}$ at $z = 0$) we find various major mergers at $z = 1$ and $z = 0.5$ and a final minor merger at $z = 0.25$. As these structures are surrounded by many other clusters at $z = 0$, we do not expect them to relax in isolation but they will probably evolve further by major and minor mergers, that will produce shocks and enhance star formation inside them in the future.

The isolated cluster located in the Lagrangian region g7358274 suffers various major mergers at $z = 5$ and a simultaneous major and minor merger at $z = 0.5$, as portrayed in figure 3.18. Then it continues growing through accretion of the surrounding medium, forming a $1.5 \times 10^{15}M_{\odot}$ galaxy cluster at $z = 0$.

Figure 3.19 shows the evolution of the most massive halo in g0272097. In this case, the halo grows mainly through minor mergers and accretion. At $z = 5$ a halo is formed by a major merger between two overdensities. At $z = 0.25$ this halo suffers a multiple minor merger and ends up forming part of the bigger structure that conforms cluster 0 at $z = 0$.

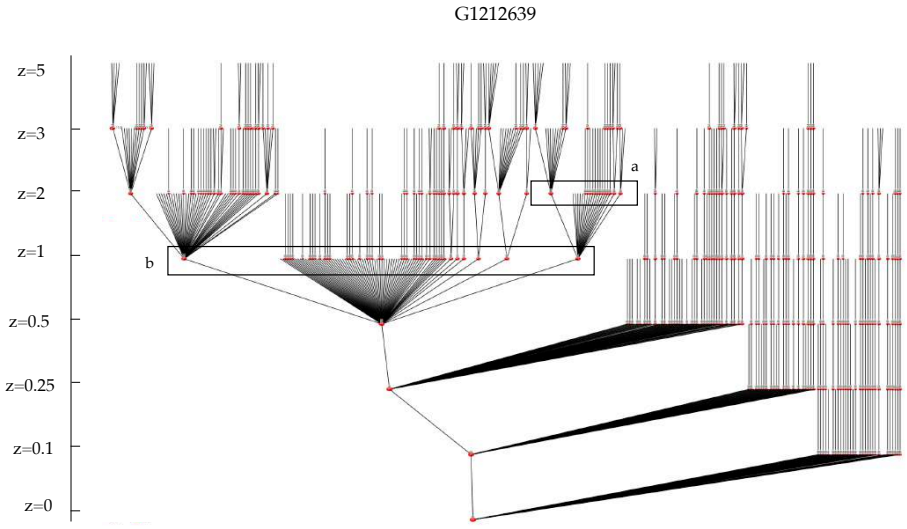

Figure 3.16: Merger tree of the most massive final halo in region g1212639. In rectangle a we see a major merger between two small halos while rectangle b shows another major merger at lower redshifts with higher mass halos. The resulting structure keeps growing though accretion of the surrounding medium from $z \sim 0.5$ on.

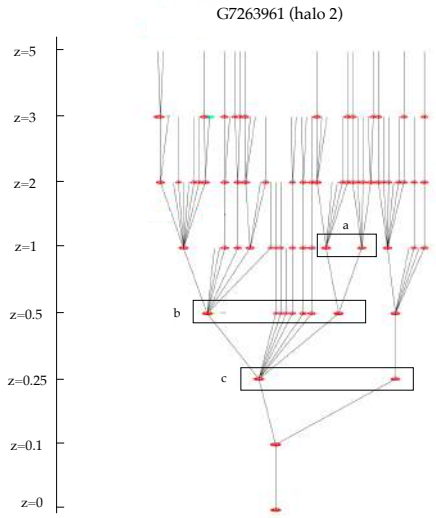

Figure 3.17: Merger tree of the second most massive cluster in the highly populated Lagrangian region g7263961. Rectangle a points to a major merger between to halos producing a structure that will again suffer a major merger leading to a galaxy cluster at $z \sim 0.25$ that will keep growing though a minor merger with a less massive halo and slowly relax till it $z \sim 0$.

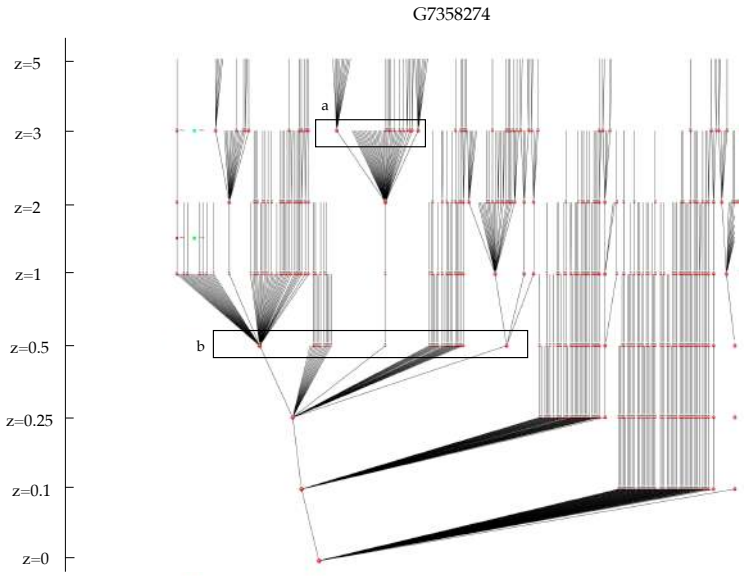

Figure 3.18: The merger three of the isolated cluster in g7358274 shows many interesting interactions between high redshift halos, like i.e. the major merger at $z = 3$, highlighted by rectangle a. Other minor and major merges construct the structures that merge at $z \sim 0.5$ forming the main structure of the galaxy cluster, that will continue growing though some very small minor merges and through accretion forming a final halo of $1 \times 10^{15} \mathrm{M}_{\odot}$.

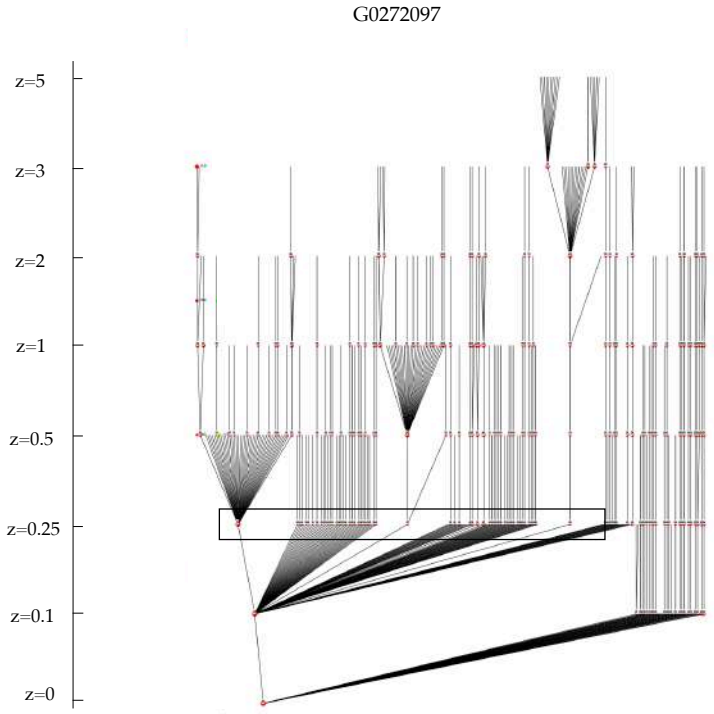

Figure 3.19: The most massive halo in region g0272097 shows some high redshift major mergers (at $z = 3$ and $z = 1$) and low redshift minor mergers and accretion, as pointed out by the rectangle at $z = 0.25$.

3.2 General Cluster Sample Study

We started by performing a study of the complete (proto)cluster sample (see appendix C for further details) at 1x resolution with the simplest hydrodynamical subgrid prescription, which includes radiative cooling and star formation (further details can be found in appendix B). We focused this first study on scatter relations between masses of the complete (proto)cluster region at different redshifts, as well as stellar content of the cluster and its central galaxy, the number of substructures and SFR values.

The first relation we studied was the scatter between the mass at high redshifts, $z = 5$, and the final mass of the cluster at $z = 0$ (see figure 3.20a). We found a very loose correlation between both quantities, showing us that the high redshift mass of protoclusters is not a good proxy for final masses of clusters of galaxies. This result is of high importance, as observations often rely on their mass estimates to declare an observation a protocluster candidate, and to relate these candidates with clusters of galaxies observed at $z = 0$. In our sample, however, this relation between protocluster and cluster masses is not direct and thus gives us a reason to doubt about the fidelity of these kind of extrapolations.

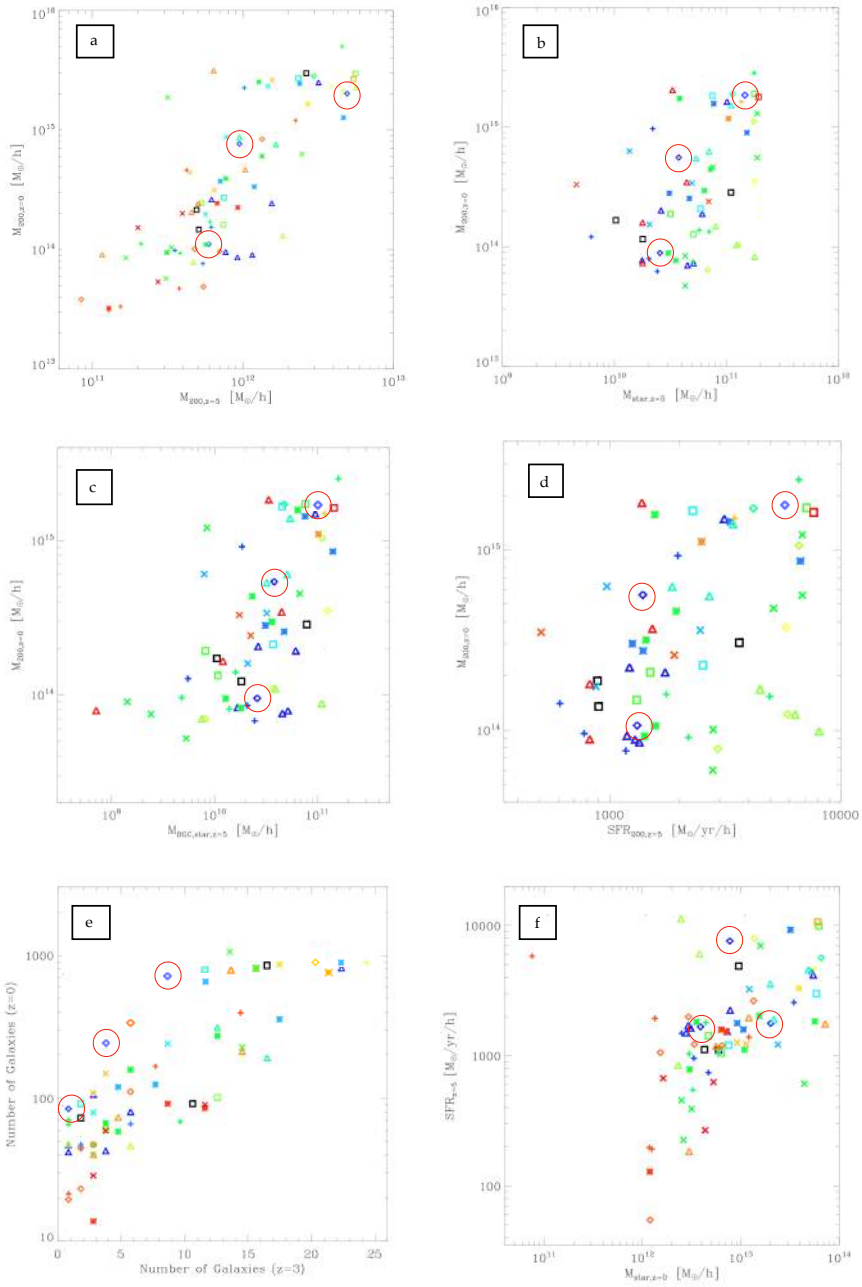

Figure 3.20: Scatter plots of the total masses, stellar masses and SFRs of the clusters in the simple runs of the Lagrangian regions of the Compass set. Points with same symbol and color are clusters belonging to the same Lagrangian region. The circled symbols are the clusters belonging to the Lagrangian region g1212639, which will be further analyzed in the next section.

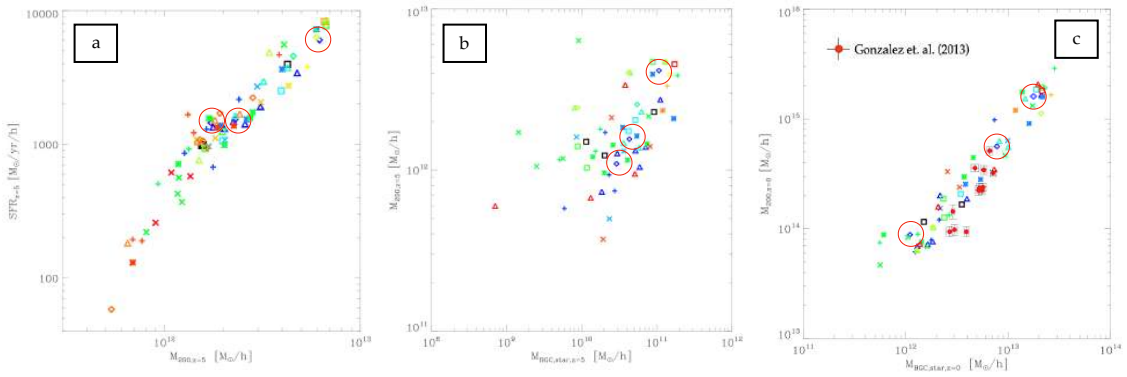

Figure 3.21: Scatter plots for the simple runs of all Lagrangian regions in the Compass set. The symbols description is identical to the one of figure 3.20.

The total stellar mass and SFRs at high redshifts do not show any clear correlation with the final cluster mass (as shown in figures 3.20b and d), although the total BCG high redshift stellar mass does show a loose correlation with it (see figure 3.20c). As the BCGs in our simulations are the main galaxies lying in the centers of our clusters, this correlation may be tightly related to the one in figure 3.20a, so that more massive high redshift BCGs have a higher stellar content and at the same time some of them belong to more massive protoclusters, thus being slightly more prone to end up in higher mass galaxy clusters at $z = 0$.

In panel e of figure 3.20 we studied the relation between the richness of protoclusters and clusters of galaxies, finding a slight correspondence. In general, there is a tendency for richer protoclusters to end up being richer galaxy clusters and viceversa. A high number of galaxies in clusters generally means also a higher number of galaxy-galaxy interactions like crossings and mergers that will enhance astrophysical processes like star formation. Thus, in view of this results we expect that richer protoclusters will suffer more energetic events that may produce starbursts all the way till their virialized cluster stage.

The SFR at $z = 5$ does not seem determine very strongly the final stellar mass of galaxy clusters (see figure 3.20f), which may lead us to the conclusion that the peak of SFR in our simulations at this resolution lies somewhere at lower redshifts (somewhere between $z = 4$ and $z = 3$ depending on subgrid physics, as we will see in the following sections).

Figure 3.21 shows relations of quantities of our clusters at same redshift ($z = 5$ for panels a and b and $z = 0$ for panel c). While the high redshift SFR does not seem to be related to the final mass, there is a strong correlation of this quantity with the high redshift cluster mass, meaning that higher mass clusters have higher stellar production. This makes sense, as higher mass clusters are expected to have a higher gas mass content and thus can have higher rates of star formation.

The stellar content of our simulated BCGs at low redshifts is clearly influenced by the total mass of the cluster, mimicking observations, like the ones reported by Gonzalez et al. (2013) and reproduced in figure 3.21c. This figure exhibits a heavy weight of central BCGs in the stellar content of galaxy clusters, as they have grown enough by merging and galactic cannibalism to be the dominant galaxy in the cluster. This relation, even if not as tight, can be found also in the high redshift case in figure 3.21b, where we see that high mass clusters have also BCGs with higher stellar mass, specially in the high mass end.

3.3 Varying Subgrid Physics Prescriptions: A Case Study

In order to make a study on the effect of our subgrid physics in galaxy (proto)cluster formation and evolution in our zoom simulations, we chose one Lagrangian region and ran the simulation with three different prescriptions for the subgrid physics, i.e. a simple run with radiative cooling and star formation, a second one with stellar evolution and a detailed SN feedback, and a third run adding AGN feedback (further details on the subgrid physics can be found in section 2 and appendix B).

To do this, we chose the Lagrangian region g1212639, which has in its high resolution region three clusters with final masses $M_0 \sim 1.5 \times 10^{15} \mathrm{M}_\odot$, $M \sim 3 \times 10^{14} \mathrm{M}_\odot$ and $\mathrm{M} \sim 1.2 \times 10^{14} \mathrm{M}_\odot$ (slightly varying with subgrid physics). This constitutes a massive enough sample to be representative of the observed high mass cluster population. These set of clusters are the ones circled in the relations presented in section 3.2. Some of the interesting features that made us choose this Lagrangian region are the high final mass of the most massive halo of the region, as well as the high stellar mass of its BCG at high redshifts and high SFR (see panels a, c and d of figure 3.20 and figure 3.21).

3.3.1 Mass Evolution

First we looked at the mass evolution of the three clusters through redshift for the three different subgrid physics prescriptions. The results are shown in figure 3.22. Interestingly, the mass evolution of the clusters does not change significantly when changing our subgrid physics. Final masses may be slightly higher in the run with detailed SNe prescription and lower in the run with AGN comparing with the simple test run, specially for halo 1 and 2. In figure 3.22c we see how halo 0 and 2 start at similar times with almost same mass and evolve almost in parallel till $z = 4$, where halo 2 starts to grow slower getting surpassed by halo 1. Same happens in panel a and b, but later, at $z = 2$ and $z = 3$ respectively. Even if the general mas evolution of our clusters does not change, the time at which surpasses happen does change significantly.

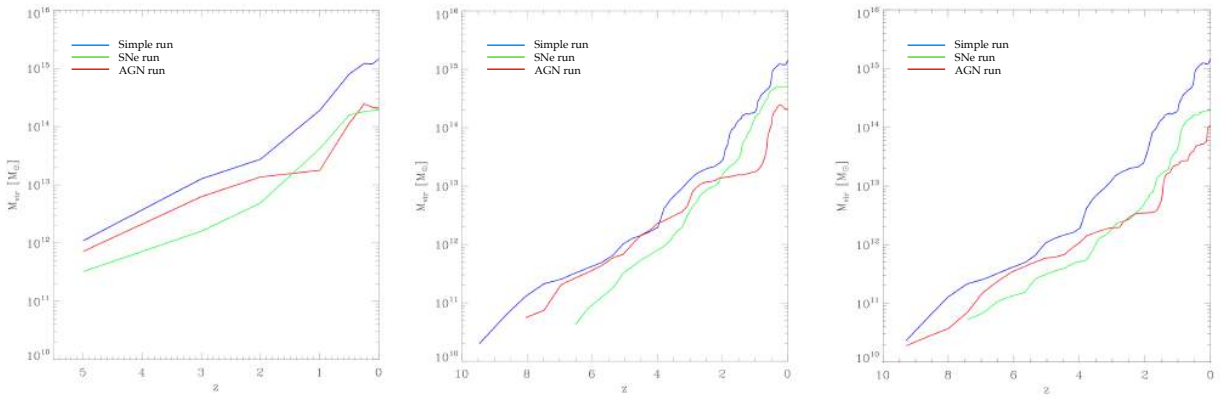

Figure 3.22: Evolution of the virial masses of the three clusters in g1212639 for the simple run (panel a), the SNe run (panel b) and the AGN run (panel c).

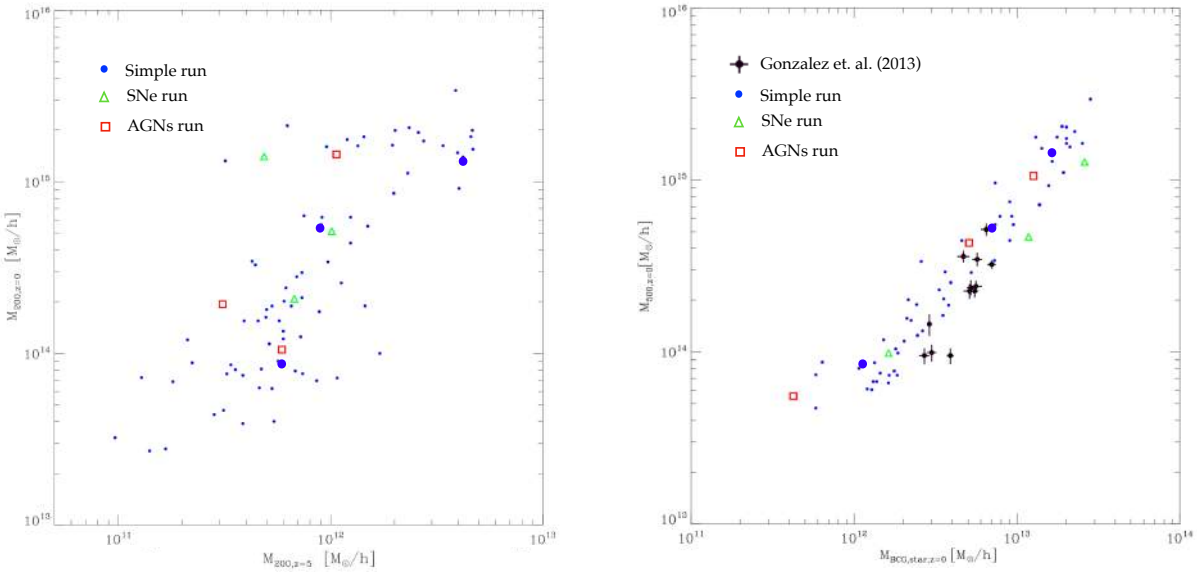

Figure 3.23: At the left: scatter plot of the relation of M_{200} at $z = 5$ and at $z = 0$. At the right: relation of the BCG stellar mass and the M_{500} mass of the cluster at $z = 0$. The blue dots stand for the simple run, where the oversized one are the ones belonging to g1212639. The green triangles correspond to the SNe run and the red diamonds to the one with AGN. The black points in the right panel are observational data taken from the paper by Gonzalez et al. (2013).

We compared also the M_{200} scatter plots performed in section 3.2 for our test runs with the SN and AGN simulations of g1212639, as presented in figure 3.23. The thicker blue dots represent the three clusters of region g1212639 with our simple prescription of

star formation. The green and red symbols stand for the SNe and AGN prescription runs. The inclusion of SNe and AGN to our subgrid physics does not seem to have created any stronger correlation between high and low redshift masses.

In the case of the BCG stellar mass vs M_{500} (see right panel in figure 3.23), the strong correlation observed for the simple runs is maintained with the new subgrid physics prescriptions, in concordance with observational data extracted from the paper by Gonzalez et al. (2013), represented in the plot with black dotes. Note that because of technical reasons we used the value of M_{200} for the simple run instead of M_{500}, while for the SNe and AGN runs we used the latter following the observed data by Gonzalez et al. (2013). The SNe run seems to overproduce stars in the central BCGs, which gets corrected by adding of AGN, as they act on the centers of massive galaxies quenching star formation.

3.3.2 Feedback Processes and Temperature Profiles

In order to accomplish a successful study of the effect of subgrid physics in our simulated galaxy clusters, we considered necessary testing the right performance of the elements more prone to causing errors in simulations, which are BHs. Therefore, in figure 3.24 we show the accretion rate vs BH mass plots at different redshifts. At high redshifts ($z \sim 5$) BHs start getting seeded and accrete following the over-plotted parallel lines, i.e. they accrete at the Eddington accretion rate. As expected, some BHs start getting quiescent already at $z \sim 3$ and accrete at lower rates. As structures grow further, BHs are seeded and follow the Eddington accretion rate, while older BHs start falling from this relation. At $z \sim 0$ very few BHs continue accreting at the maximum rate, rather most of them accrete at lower rates or have become almost completely quiescent.

To further check what are the internal effects of feedback processes in our clusters, we looked into the temperature and density phase space of gas particles inside halo 0 at different redshifts. This kind of studies are interesting as they give us an insight into the thermal and dynamical processes of gas inside clusters and about the accretion processes at different redshifts, which have a high influence when it comes to the evolution of proto-clusters into galaxy clusters (see Murali et al., 2002).

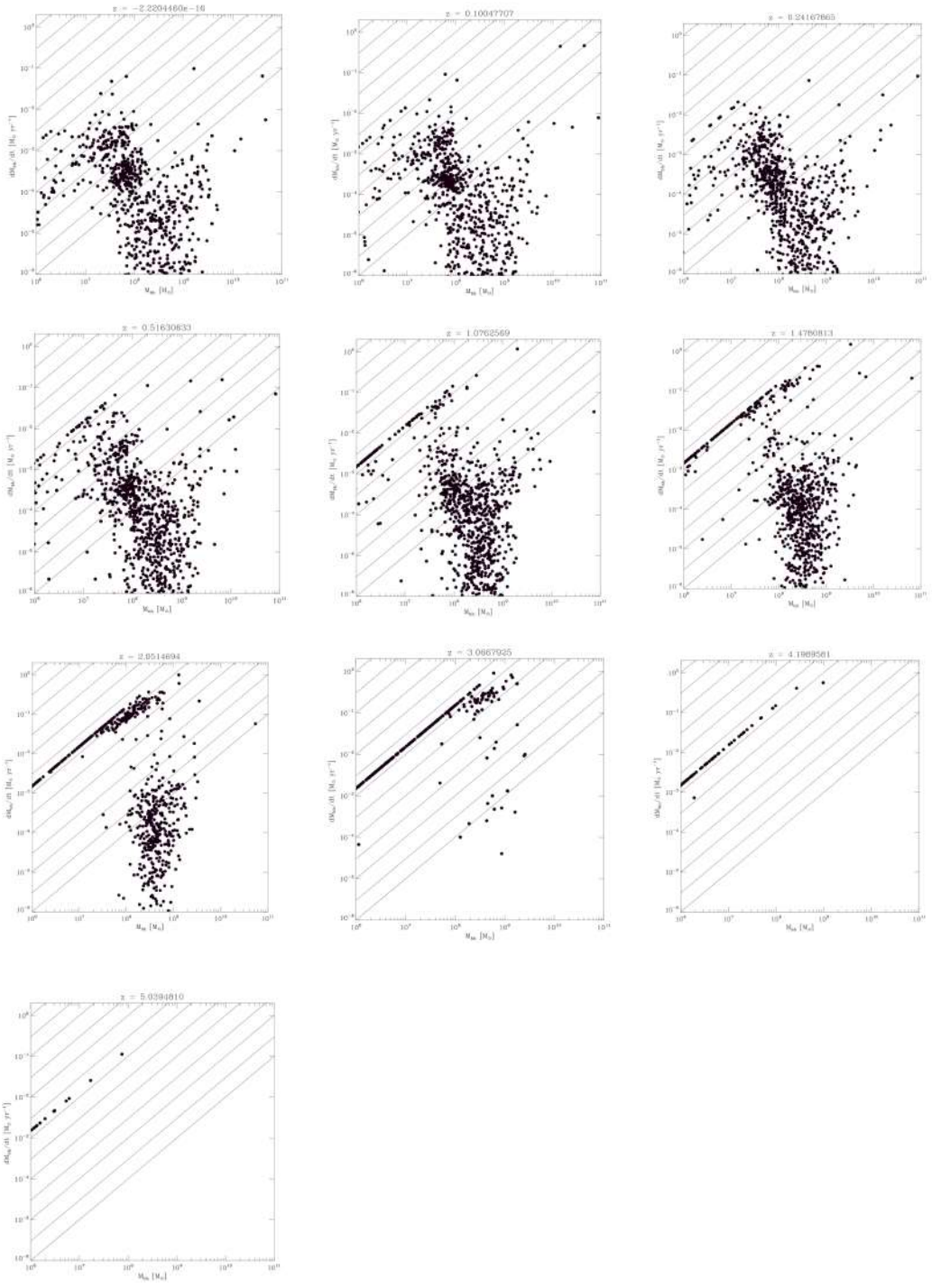

Figure 3.24: Accretion rate vs BH mass for the seeded BHs at different redshifts. The lines indicate the Eddington accretion rate slope. At high redshifts (see lower panels) BHs are seeded in the overdensities and accrete at the Eddington accretion rate. At $z \sim 3$ some BHs start accreting at lower rates and fall from this relation. At $z \sim 0$ most of the BHs are accreting at lower rates or have become almost completely quiescent.

Figure 3.25 introduces the principal features that can be observed in such a diagram. We can clearly differentiate hot and cold gas, the first one corresponding to shock-heated gas in (quasi-)virialized haloes and at the low-density end around filaments, and the latter to radiatively cooled, dense gas in galaxies. This gas spans a range of densities till the star-forming threshold at $\rho \sim 10^{-25} g/cm^3$. Once that threshold is surpassed gas particles become multiphase and start forming stars, entering in the star-forming branch. The low density tail at the left of the figure has to do with the adiabatic expansion approximation and consists of low-density, highly photoionized gas in the IGM. In our cosmological model with cosmological constant the Universe expands. The increase in volume causes a pressure decrease, that similarly to how it happens with air when pressure decreases, leads to an adiabatic cooling of the gas clouds. This forms the adiabatic expansion tail, that maintains a tight temperature-density relation by the competition of adiabatic cooling and photoionization heating (Hui and Gnedin, 1997; Kereš et al., 2005). The branch slowly disappears once the structure gets more compact and virializes at $z < 0.5$.

The high density tail on the right side of the figure has a very different nature. It is attributed to wind particles, associated to starbursts and galactic outflows. Winds are a very important outcome of stellar feedback, as they can reheat and transport collapsed material from the centers of galaxies back to their extended DM halos and beyond into the IGM. By offering baryons a route to climb out of the galactic potential wells, they help reducing the overall cosmic star formation to a level consistent with observational constrains. Even if winds are necessary to reproduce observations, the mechanism by which they originate in real galaxies and clusters is not yet well understood Mac Low and Ferrara (1999); Efstathiou (2000); Aguirre et al. (2001); Springel and Hernquist (2003); Brüggen and Scannapieco (2009).

In our galactic winds implementation we consider that the mass loss rate that goes into the wind is proportional to the SFR. Whether the material will be able to escape the potential well depends mainly on the velocity to which the gas is accelerated, the amount of gas involved and the depth of the potential well it resides in. Once kicked, the wind will carry a previously established fraction of the SN energy. Real galactic outflows are thought to originate from regions close to the surface of star-forming discs, so that winds can escape the star-forming region without causing a major impact on the ongoing star formation. However, in our model we do not restrain wind formation to a surface layer. We rather follow a probabilistic criterion where we allow all SPH particles in the star-forming region to become wind particles. The problem arising is that wind particles coming from inner parts of the star-forming region would be stopped by other particles inside that region, which could lead to strong perturbations due to the momentum input and a rapid dissipation and thermalization of the kinetic energy. This contrasts heavily with our understanding of winds escaping from their dense environment without affecting it and being stopped first outside the region by gas-dynamical interactions within the halo.

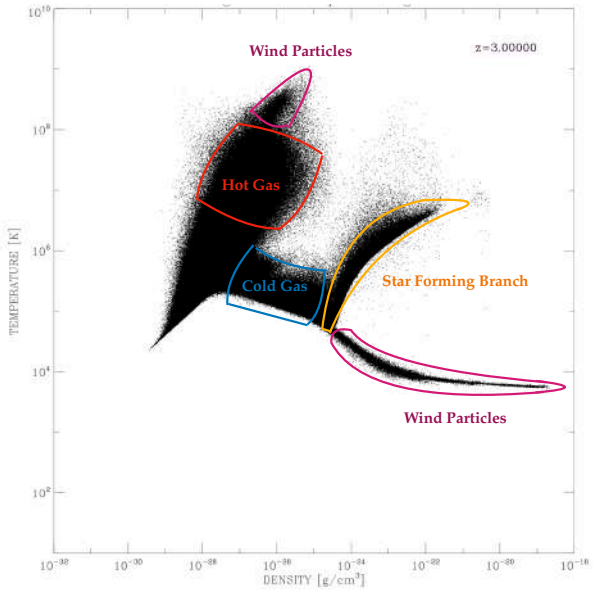

Figure 3.25: Scheme of a temperature vs density diagram. The labels show the hot and cold gas regions, the star-forming branch and the wind particle tails. The tail at the bottom left is related to the adiabatic expansion approximation.

To mimic this behaviour, we circumvent the problem by allowing wind particles not to interact with the dense environment they come from. We decouple' them a brief time from the hydrodynamic interaction, so that they neither exert no receive hydrodynamic forces during that period of time (although they continue being included in the computation of the gas density and in gravity calculations). This allows the wind particles to travel undisturbed up to a few kpc, so that they are able to leave the dense star-forming phase before coupling again. Thus, these wind particles are by definition excluded from star formation even if they are above the density threshold and thus, they appear in the phase diagram as a low temperature branch at very high densities. In this way, we can reproduce reasonably well the strong, but quiescent mass loss from a star-forming region. However, we want to emphasize that this cold high-density branch should not exist in reality, as at those densities the particles should be multiphase and on the equation of state for star-forming particles. Thus we say that its appearance is an artifice of our galactic outflow modelling (the reader may check appendix B for further details).

Figures 3.26 to 3.29 show the evolution of the temperature vs density phase space diagrams for the most massive cluster in region g1212639, performed with the three different subgrid physics prescriptions at different redshifts. At $z \sim 7$ the majority of the gas is rather cold, with a lower limit of $T \sim 10^{14}$ K (which corresponds to the limit for atomic cooling), and we do not have many star-forming particles. As the protocluster region evolves the amount of hot gas particles and star-forming particles increases substantially so that at $z \sim 4$ we already have a clear hot gas region and a well defined star-forming

branch. This in turn means a higher amount of supernovae and supernova feedback that produces winds that manifest in the upper part of the hot gas and in the high density tail of the diagram.

At lower redshift ($z \leq 1$) the amount of star-forming particles slowly decreases and the gas temperature starts exhibiting a bimodal distribution that is more pronounced the more the structure evolves. About half of the gas seems to follow the classic picture of galaxy formation, where it gets shock heated to roughly the virial temperature of the galaxy (or cluster) potential well ($T \geq 10^6 K$) when accreted, getting in hydrostatic equilibrium with the DM (Hansen et al., 2011) before cooling and condensing to form stars. The other half of the gas seems to radiate its acquired gravitational energy already at much lower temperatures ($T \sim 10^5 K$) forming a bimodal temperature histogram. This colder gas that does not get shock heated is through to be accreted through filaments, while hot accretion is supposed to be quasi spherical (Kereš et al., 2005; Macciò et al., 2005). Thus, in general, the cold mode' of accretion tends to dominate low-mass systems, while the 'hot mode' accretion is predominant in higher mass systems. This halo mass dependence leads to a redshift dependence of cold and hot accretion rates, so that the cold mode dominates at high redshift where overdensities are less massive and accrete mainly through filaments, and hot mode dominates at group and cluster environment at low redshift where structures are more massive and closer to virialization.

Indeed, cold accreted gas dominates in our cluster at $z \leq 3$ for all physical prescriptions. At lower redshifts warmer gas starts balancing the situation until hot low density gas ends up dominating at $z \leq 0.1$. This is in concordance with the morphological evolution studied in section 3.1.1. At high redshifts, we find an ensemble of small halos, mostly unvirialized, lying in the nodes of a web and thus accreting from the cool dense filaments connecting them. At lower redshifts as structures start getting more compact, larger in mass and closer to virialization, the accretion is less filamentary and thus our objects are expected to accrete the gas from their surroundings more spherically, shock heating it to the virial temperature of the halo.

In view of this picture we can divide our gas particles by means of their possible temperature history in four different types. Some hot particles, may have been heated at $T \sim 10^6$ K or higher by shocks when accreted and they retain that temperature, remaining at equilibrium with the corresponding virial halo temperature. Other particles may be shock heated to $T \sim 10^6$ K but then cool slowly and fall to lower temperatures. Some particles of the cold branch that lie closer to the center of the halo may have been shock heated first but cooled down rapidly, maybe even suffering different episodes of heating and cooling. The final type of gas particle was part of a cold accretion process and probably was never substantially shock heated (Hansen et al., 2011).

In order to understand better cold and hot accretion processes and thermodynamic evolution of the gas in our clusters, we studied the effects of SN feedback and specially AGN

feedback in the temperature vs density phase space diagrams comparing them with our simple physics run. One of the most outstanding signatures of AGN feedback in the phase space diagrams is the repeated heating of cold dense gas that lies near the star formation threshold (see the panels at $z \leq 1.7$ in figures 3.28 and 3.29, and also the panels at $z = 2.78$ in figure 3.27 or $z = 4.19$ in figure 3.26). While in the simple run there is no change in the star-forming branch till $z = 1$, the SNe and the AGN run show clear earlier quenching of star formation portrayed in the shortening and fading of the star-forming branch, starting at $z \sim 2.3$ and continuing till $z = 0$.

Both feedback processes are having a clear influence in quenching star formation at low redshifts when compared to our simple run, although the run with AGN feedback quenches it even more than the one with only SN feedback (see the SF branch in the last panel of figure 3.29). In the case of the AGN run, as the SF branch shortens, the amount of warm dense gas lying before the SF threshold increases. This may be the effect of AGN feedback in the central denser gas, which heats the medium reducing star formation. We can also see dense warm gas in the run with only SN feedback (see middle panel at $z = 1$ in figure 3.28), but SN feedback is clearly not capable of injecting as much energy as AGN in the central dense gas regions.

The evolution of the cold dense wind also follows the evolution of the star-forming branch. As the mass transferred from the star-forming region into the wind depends on the SFR, the quenching of star formation produces a reduction of the wind, which again is more pronounced in the SNe and AGN runs. The shape of the wind in the SNe is wider than the one in the simple run due to the inclusion of metals with different cooling rates. The shape of the wind branch changes even more in the AGN run. This is due to a new interpretation of their density contribution which is still in development and will be further studied in future works., as it does not have any obvious further influence in our current work.

Figure 3.30 shows the redshift evolution of the total temperature of the most massive cluster (solid line) and its BCG (dashed line) for the three runs with different subgrid physics (in blue the simple model, in green the SNe model and in red the AGN model). The simple run shows overall a higher cluster and BCG temperature till it drops at $z < 0.5$ to the temperature of the SN and AGN runs. The increase in temperature occurs smoothly for all runs for $z < 0.5$. However, right after $z \sim 0.5$ all runs show a small bump in temperature, that may be related to the major merger suffered by the cluster around that same redshift (see figure 3.16). The AGN and SN runs show identical cluster temperature features and evolve parallel to each other with the AGN run being slightly displaced towards higher temperatures, maybe due to a continuous feedback from BH accretion.

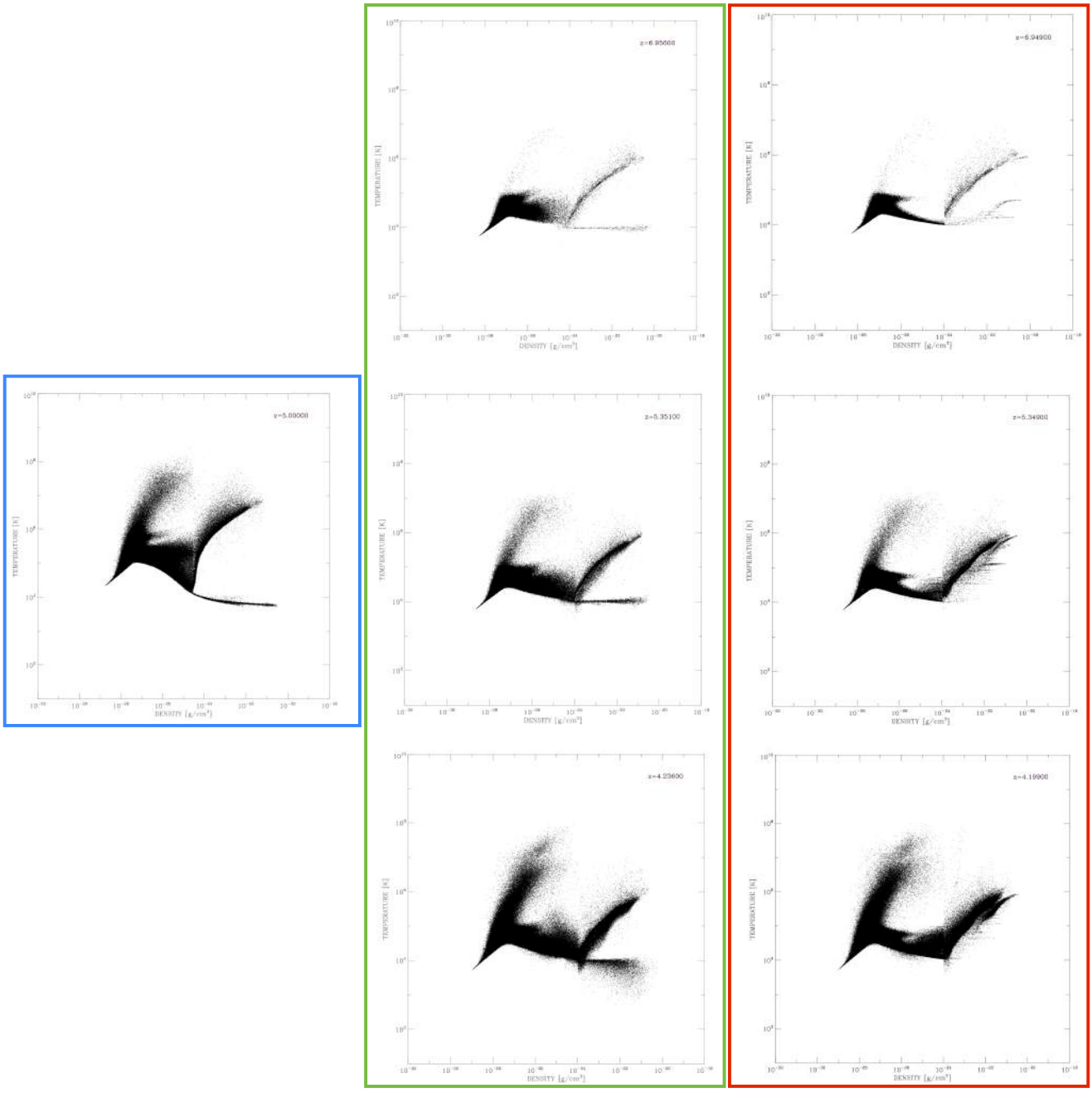

Figure 3.26: Temperature vs density diagrams for the simple, SNe and AGN runs (from left to right) for different redshifts. The lower number of outputs in the simple run allows the complete comparison only at certain redshifts.

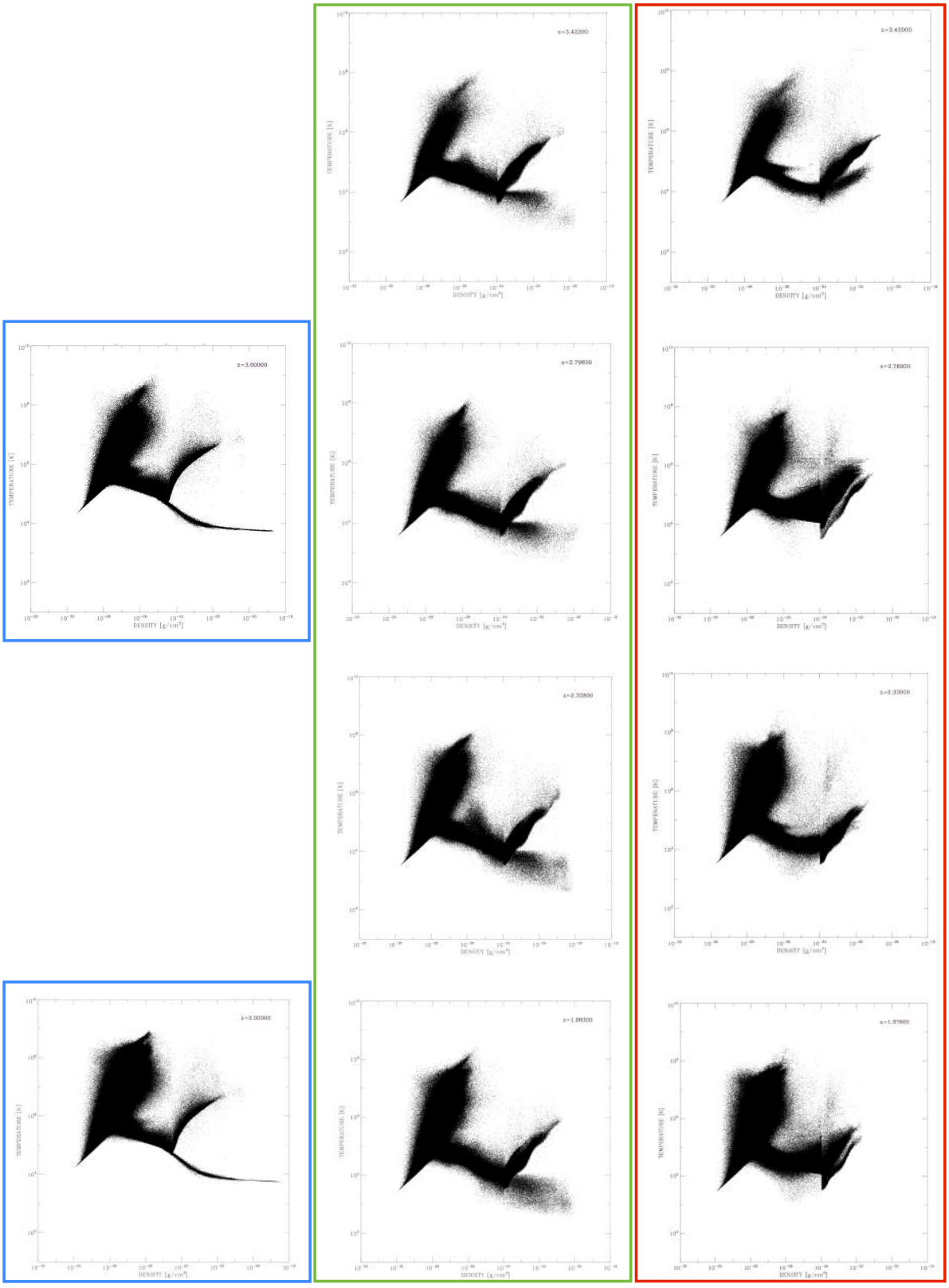

Figure 3.27: Continuation of figure 3.26

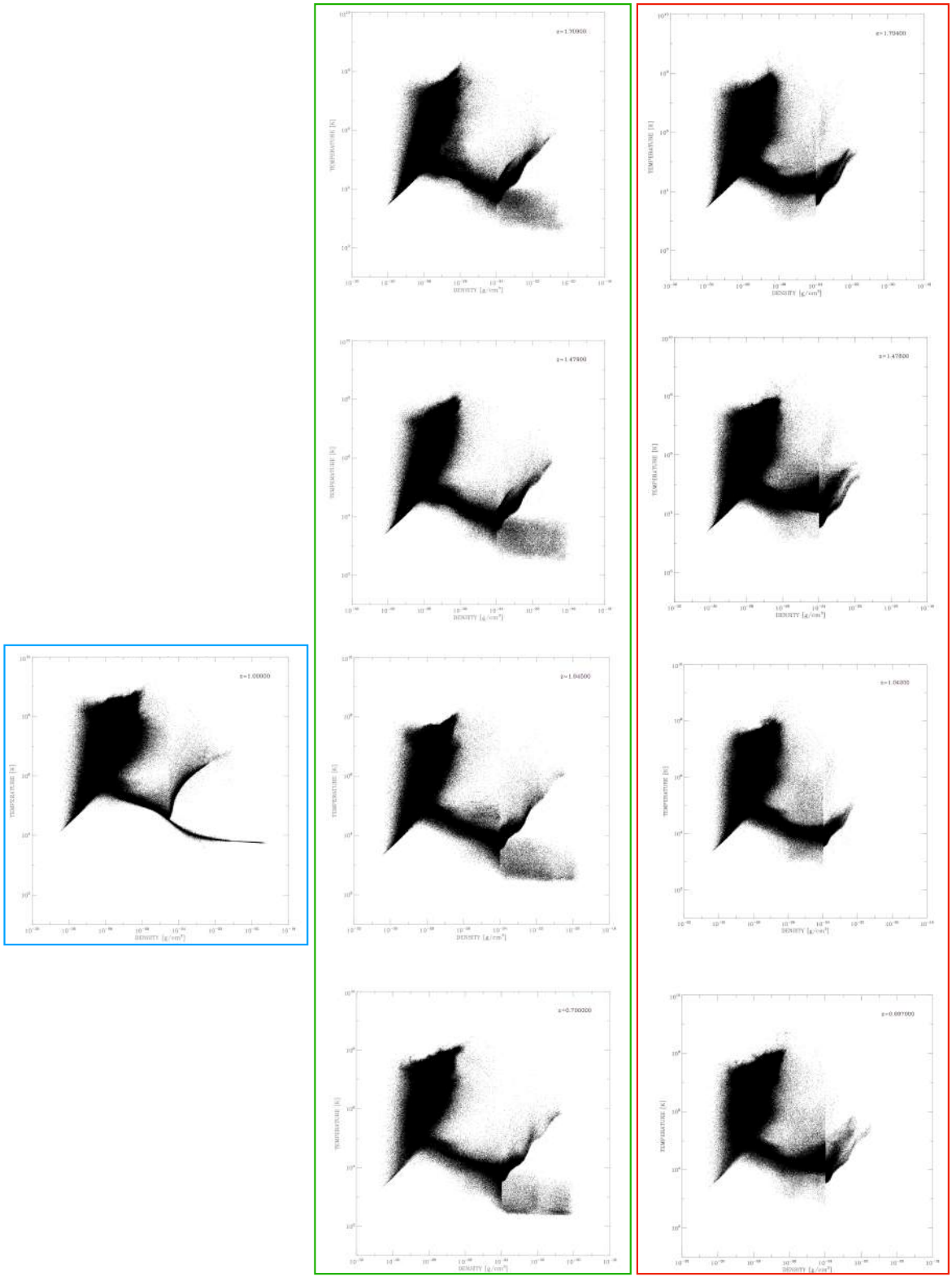

Figure 3.28: Continuation of figure 3.27

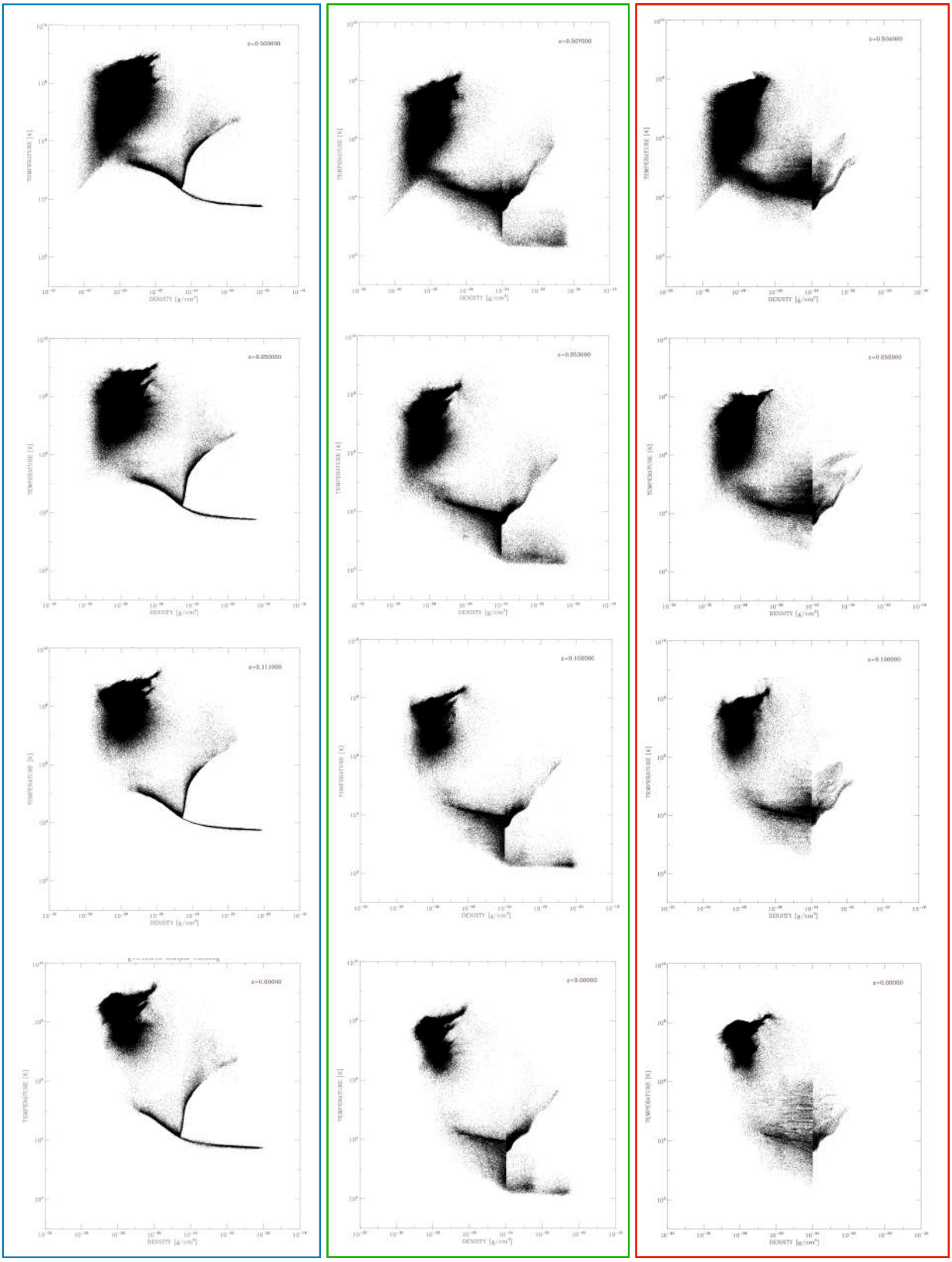

Figure 3.29: Continuation of figure 3.28

Additionally, figure 3.31 shows the influence of the BCG in the total cluster temperature. The BCG starts having a strong influence already at $z \sim 4$. After $z \sim 3$ the BCG seems to suffer some overcooling comparing with the rest of the cluster, visible in the increase in the SFR inside the galaxy. As the BCG grows and the cluster gets more compact and virializes ($z < 1$), the difference between both temperatures decreases dramatically. Overall, the difference in temperature between the cluster and the BCG is higher in the AGN run than in the SN run. Thus, we see that AGN are proportionally more efficient heating the sattelite galaxies and the surroundings of those than the central BCG itself.

Another interesting feature of galaxy clusters is their temperature profile. Already in the 90s ASCA observations established that most of the clusters show departures from isothermality, with negative temperature gradients (Markevitch et al., 1998). The improved Chandra and XMM-Newton satellites have provided an even more detailed picture of temperature profiles in nearby galaxy clusters. They show clearly that relaxed clusters have a steady declining profile towards the centre, reaching values in the innermost regions that may be about half the overall virial cluster temperature (e.g. Vikhlinin et al., 2005; Piffaretti et al., 2005; Pratt et al., 2007; Baldi et al., 2007, 2012) . The current galaxy cluster picture proposes that the cause for this temperature decline in the central region is gas cooling, together with a feedback mechanism that supports it so that it does not fall into overcooling and thus suppressing star formation.

Hydrodynamical simulations have demonstrated being able to reproduce very well the temperature profiles of galaxy clusters outside the core regions, where gas cooling is less important (Loken et al., 2002; Roncarelli et al., 2006)). However, once we introduce gas cooling, temperature profiles usually get steeper in the core regions, in disagreement with observations (e.g. Valdarnini, 2003; Borgani et al., 2004; Nagai et al., 2007). This conflict between simulations and observations is believed to be caused by the inability of current feedback models in balancing the cooling runaway.

In figure 3.32 we show the comparison between observations of temperature profiles from Nagai and Kravtsov (2005) and the temperature profile of our simulated cluster with the three different subgrid physics implementations. The central profiles of our simulated cluster are steeper for all the three runs than the ones derived from observations. The central profiles improve when adding more complex feedback. AGN are specially helpful in this matter, as they act in the center of BCGs and thus in the center of galaxy clusters. The situation is not better for the radiative simulations done using AMR (solid black line; taken from Borgani and Kravtsov (2011a)). However, we see how the non-radiative comparative run, represented by the black dashed line, shows no core cooling at all, thus pointing to the unavoidable need of radiative cooling in our simulations.

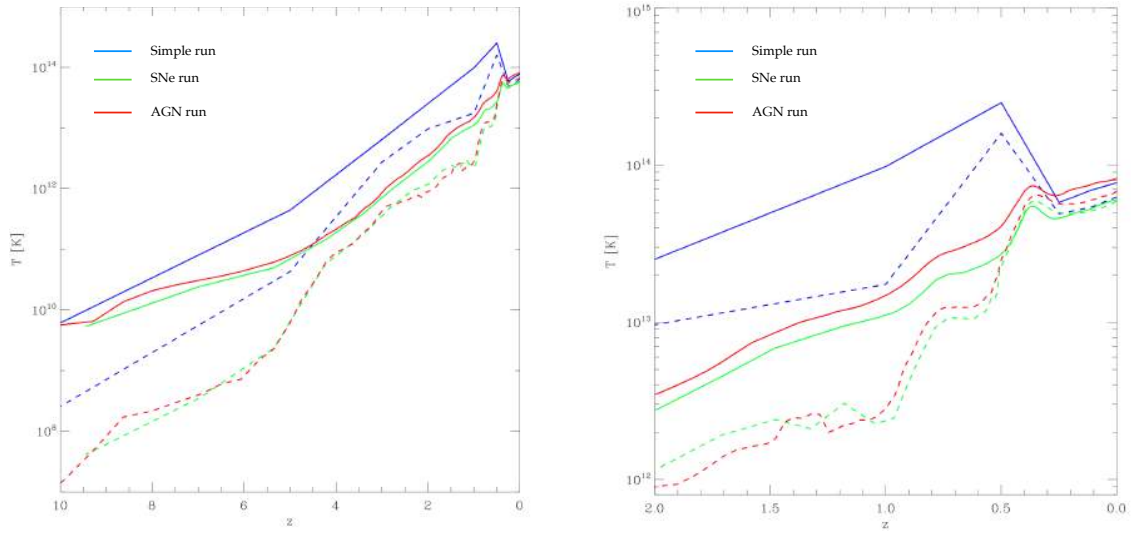

Figure 3.30: Temperature of the most massive cluster in g1212639 through redshift in the simple (blue), SNe (green) and AGN (red) runs. The solid line shows the temperature of the complete (proto)cluster region, while the dash lines stand for the temperature of the associated BCG.

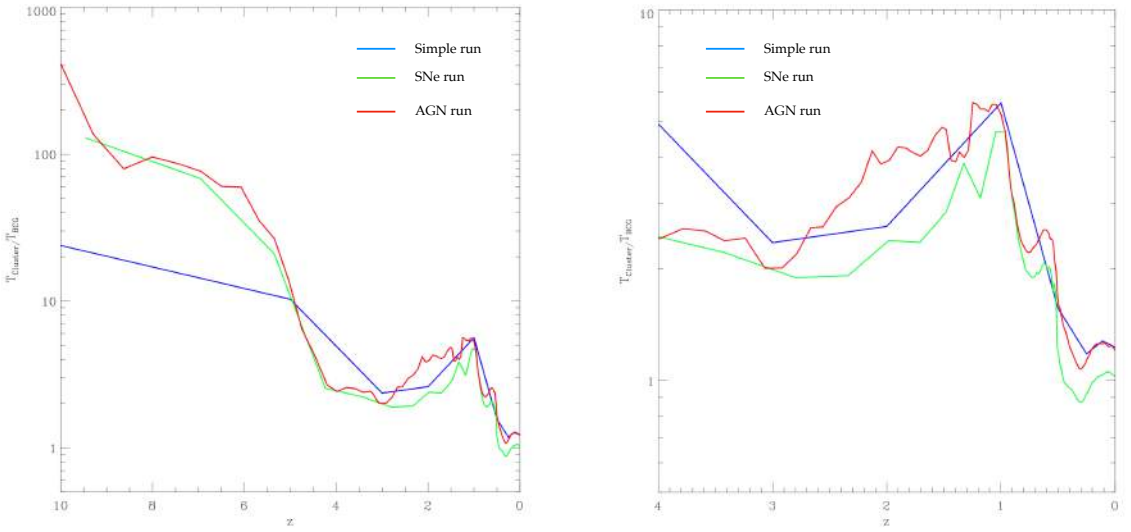

Figure 3.31: Comparison of the temperature of the BCG with respect to the total temperature of the cluster (simple run = blue; SNe run = green; AGN run = red). The influence of the BCG in the (proto)cluster is already notorious at $z \sim 4$ and, suffering some small changes, it increases even more at $z \leq 1.0$

The task of developing an efficient feedback scheme that prevents overcooling in relaxed cluster centers is complicated, as the fact that a feedback mechanism is able to produce the

correct temperature profiles does not guarantee in itself that overcooling is prevented. We may have a scheme that produces temperature profiles which are in reasonable agreement with observations but still have a resulting too high stellar fraction within clusters. As overcooling happens in the centers of galaxy clusters, it is expected that a correct AGN prescription would be able to regulate overcooling in such a way, as to get results in concordance with observations. Our current AGN prescription in the Compass zoom simulations improves the temperature profiles when compared to the runs without AGN, but still lies in disagreement with the observed profiles. This is a sign that further development of our AGN feedback is still necessary.

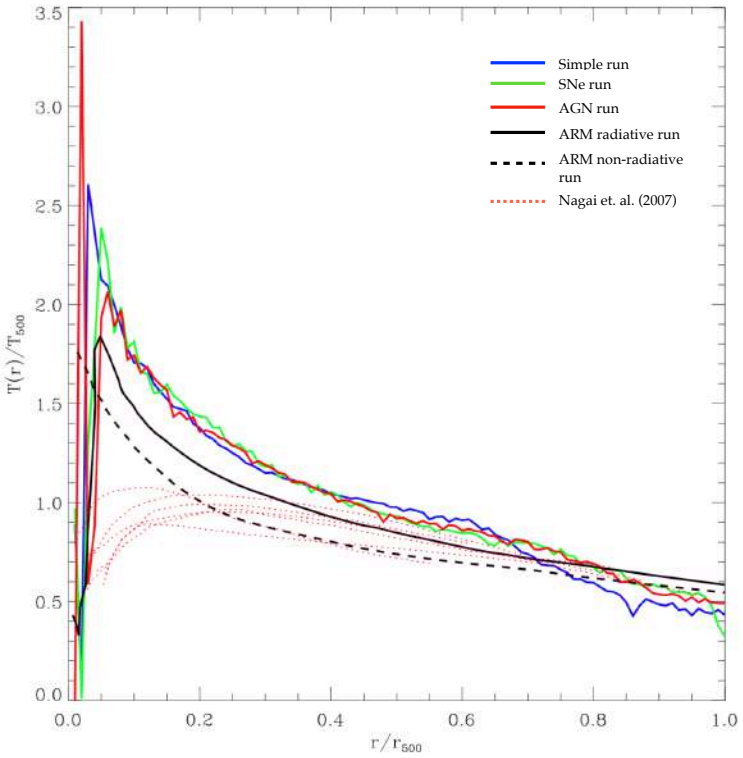

Figure 3.32: Temperature profiles for observed and simulated clusters at $z = 0$. The temperature profile of our simulated cluster is shown for the three different runs (simple run = blue; SNe run = green; AGN run = red). The solid black line stands for an AMR radiative simulation of a cluster presented by Borgani and Kravtsov (2011a). The dashed black line stands for the same cluster in a non-radiative simulation. The red dotted lines are temperature profiles for clusters observed by Nagai et al. (2007)

3.3.3 Star Formation Rate in Clusters and Central Galaxies

Getting the correct rate of stellar production in clusters is one of the main concerns when it comes to the correct reproduction of the processes inside these massive structures in simulations. In fact, even if models and simulations to date get generally the right amount

of stars at low redshifts (or even overproduce stars), they struggle reproducing the large SFR observed at high redshifts (see i.e. Saro et al., 2008; Granato et al., 2015).

The panels shown in figure 3.33 present the SFR history of our main cluster and corresponding central for the three different subgrid physics runs. All three runs show a peak in SFR at high redshifts, as established also by observational data. In the case of the simple run and the run with SNe the peak lies at $z \sim 2.7$, while in the AGN run this peak takes place before, at $z \sim 3.5$. The BCG SFR for the simple and SNe run increases smoothly with redshift, showing some abrupt changes only from $z \sim 1.5$ on, which may be related to major mergers happening between the halos at lower redshifts (see merger tree in figure 3.16). In turn the BCG in the AGN run evolves quite differently. It has an initial increase in the SFR around $z \sim 9$ and then remains around a value of SFR ~ 300 $M_\odot$/yr till $z \sim 1.5$. In the meantime the SFR suffers many abrupt changes, specially around $z = 4$, which corresponds to the SFR peak. The absence of the smooth increase and the abrupt changes in SFR may be related with high probability to the interplay between cooling and heating by AGN feedback, which affects strongly the center of the cluster and thus the BCG.

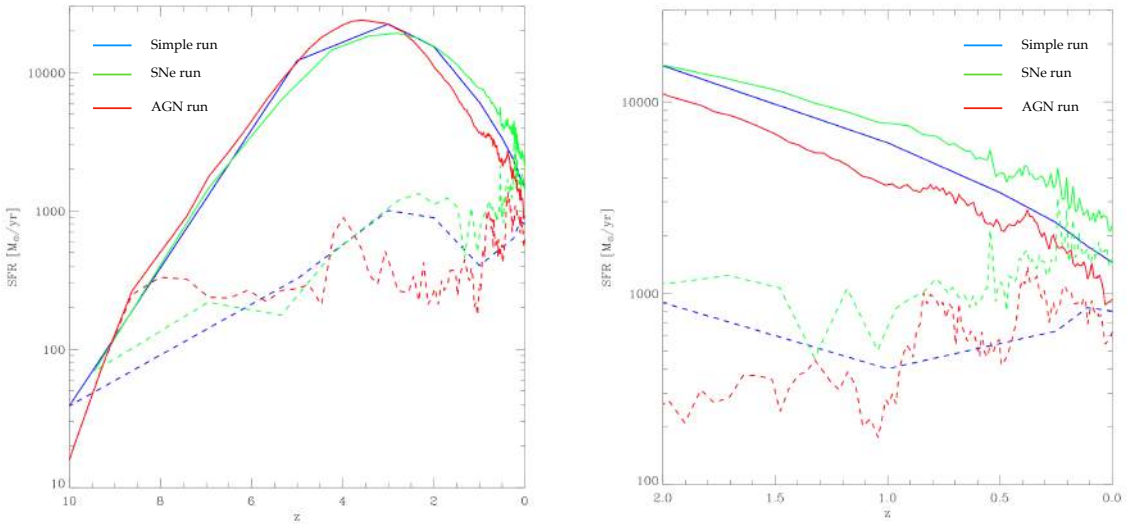

Figure 3.33: SFR with redshift for the complete cluster (solid line) and its BCG (dashed line). The different runs are color coded as follows: simple run = blue, SNe run= green, AGN run = red.

In figure 3.34 we present more clearly the relation between the BCG SFR and the complete SFR of the cluster through cluster history. It is specially outstanding how the cluster in the AGN run seems to be way less influenced by the BCG star formation rate at high redshifts, $1.5 \leq z \leq 5.5$. This is no surprise, as the AGN feedback quenches specially star formation in centrals, thus giving them a less protagonist role in star production. A

high starburst can be seen in the sudden drop at $z \sim 4$, followed by smaller starbursts at lower redshifts. These abrupt changes in the SFR of the BCG may be strongly related to the AGN feedback cycle. AGN accrete cooler gas from their surroundings, producing a feedback in the process that heats the surrounding gas and thus hinders accretion, lowering AGN feedback and allowing gas to cool again and condense forming stars.

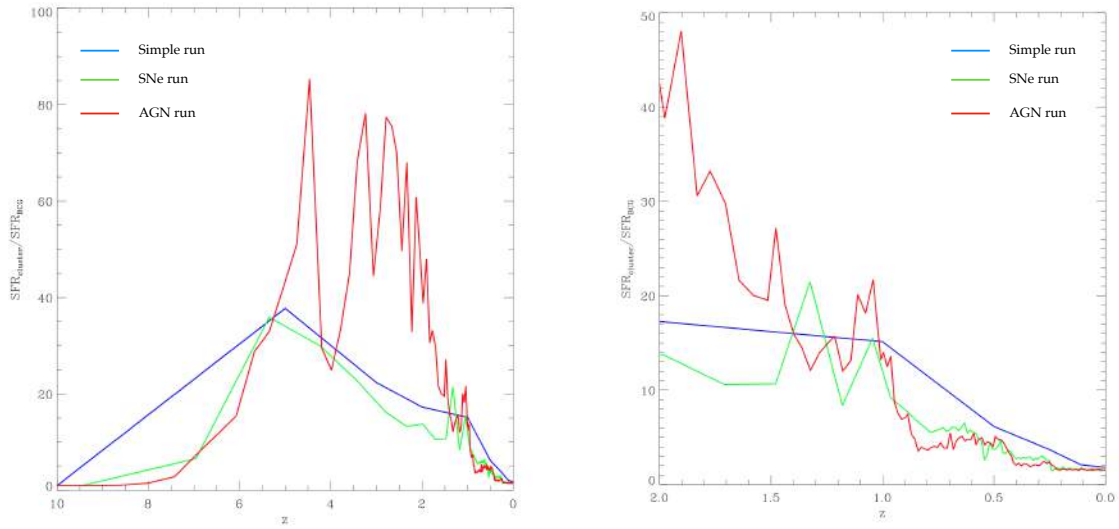

Figure 3.34: Influence of the SFR of the BCG in the total SFR of the cluster through redshift.

At $z < 1.5$, the cluster gets more compact and relaxed, the SFR has decreased significantly and the BCG has become the main star producer for all three runs. In figure 3.35 we show the SFR of our BCG for the different runs, with the solid lines being the SFR of the complete region as stated by SUBFIND and the dashed lines the SFR corresponding to a 30 kpc aperture. This aperture criterion is applied in an attempt of excluding the ICL region from the SFR computation, as observations exclude it in their measurements.

The observations we compare to are taken from the paper by McDonald et al. (2018), which constitute a subsample of the BCGs presented by Fraser-McKelvie et al. (2014). The sample selection was performed regarding all galaxy clusters in a volume limited sample, $z < 0.1$, with a measured X-ray luminosity in the ROSAT $0.1 - 2.4keV$ band $L_x > 10^{44} erg/s$, which ensures a completeness of 80% for the cluster sample (see Fraser-McKelvie et al., 2014). By selecting the sample by cluster properties instead of BCG properties, the sample is expected to be less biased towards high SFRs. However, this original sample was discovered to have some biases related to the lack of important k-corrections (see Green et al., 2016), which were corrected by **?**. The clusters have masses in the range $4 \times 10^{14} \leq M_{500} \leq 1.5 \times 10^{15} \mathrm{M}_{\odot}$, which coincides with our simulated cluster final mass $M_{500} \sim 1.3 \times 10^{15} \mathrm{M}_{\odot}$.

Our results present a strong agreement between the SFR of the AGN run within the 30 kpc aperture and the observations (see figure 3.35). While the simple run and the SNe run show an overproduction of stars at low redshift, AGN seem to successfully quench star formation at low z, bringing the results to the observational levels.

The total sSFR (solid lines in figure 3.35) shows values similar to the ones reported for EAGLE and IllustrisTNG for halos with masses $M_{200} \sim 1 \times 10^{14}$ $M_\odot$, which are sSFR $\sim 2 \times 10^{-12} yr^{-1}$ and sSFR $\sim 1 \times 10^{-11} yr^{-1}$ for EAGLE and IllustrisTNG respectively (see Davies et al., 2019). Within the 30 kpc aperture all of our runs, but more pronounced in the AGN run, seem to have a too high stellar content in comparison to the low redshift SFR, possibly pointing to a previous overproduction of stars.

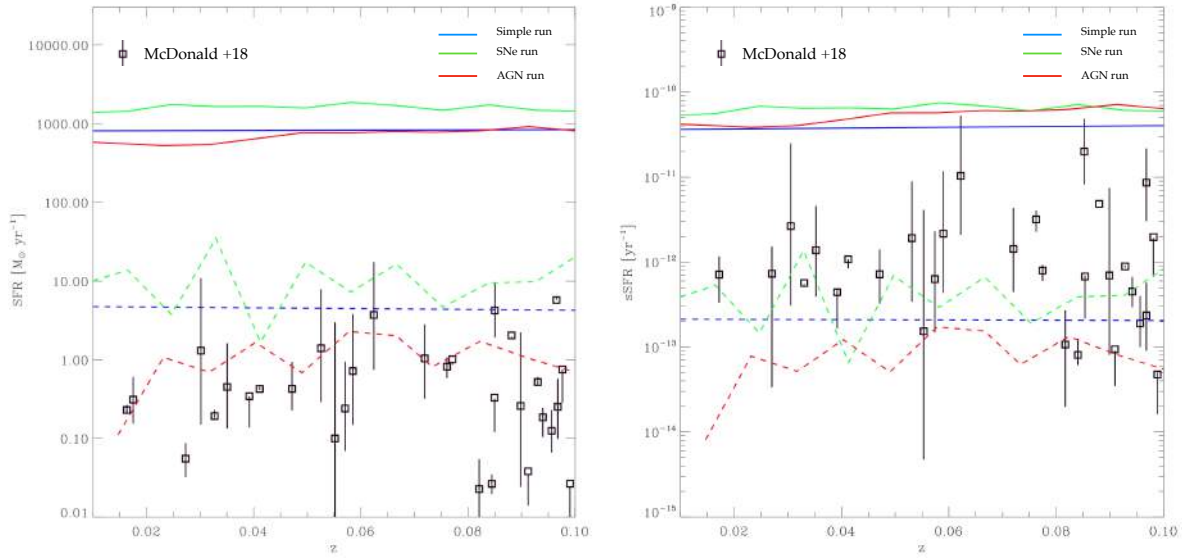

Figure 3.35: SFR and sSFR for our three runs, counting the complete region as stated by SUBFIND (solid line) and using a 30 kpc aperture (dashed line). The points are observational data from the cluster sample of Fraser-McKelvie et al. (2014) after the corrections performed by McDonald et al. (2018)

While the SFR at low redshifts in simulations is similar or higher than the observational values, it is a common problem in all protocluster simulations the reproduction of the large, observed star-formation rates at high redshifts (see i.e. Saro et al., 2008; Granato et al., 2015). In the three panels of figure 3.36 we present the integrated SFR as a function of the area on sky for our simulated cluster at different redshifts for the three different runs. In the right panel we added the observed integrated SFR for the proto-cluster SPT2349-56, observed at $z = 4.3$ with a virial mass of $M_{vir} = 2 \times 10^{13}$ $M_\odot$, which is of the order of our simulated cluster mass at that redshift, $M_{vir} = 1.3 \times 10^{13}$ $M_\odot$. For all the three runs, the

sum of the simulated star formation rate is a factor of 4 lower than the one observed for SPT2349-56.

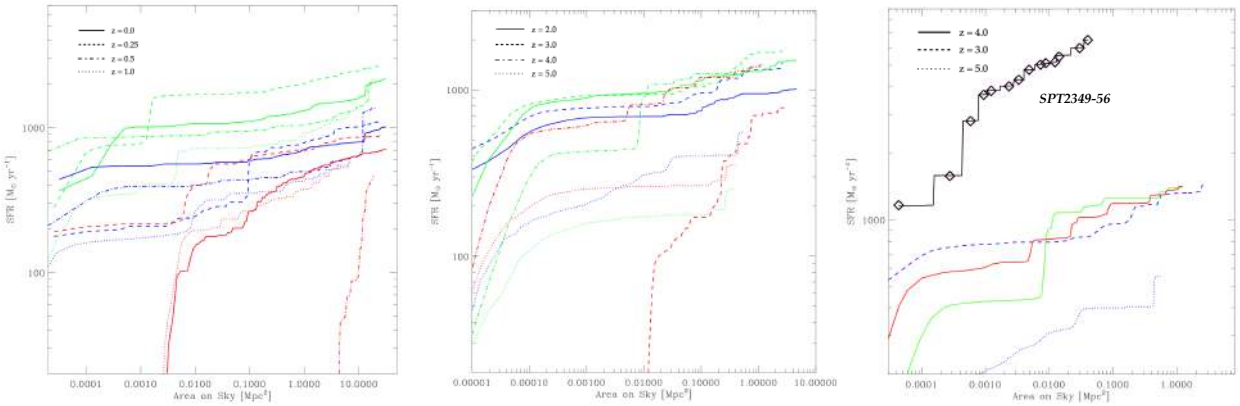

Figure 3.36: Integrated SFR of our (proto)cluster at different redshifts for the three different runs. The right panel shows as a comparison the values of the integrated SFR for the protocluster SPT2349-56 at $z \sim 4.3$.

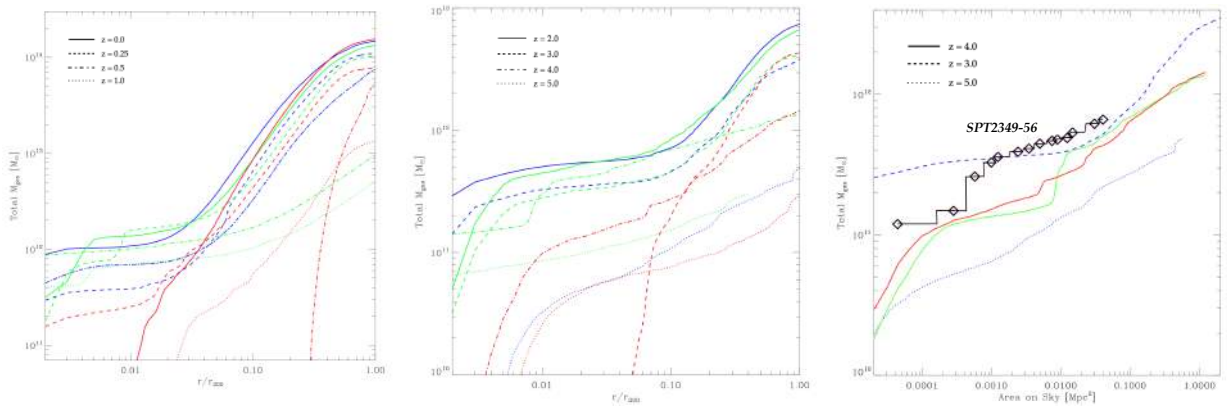

Figure 3.37: Integrated gas mass of our (proto)cluster at different redshifts for the three different runs. The right panel shows as a comparison the values of the integrated gas mass for the protocluster SPT2349-56 at $z \sim 4.3$.

On top of this we also studied the amount of gas in our simulations at different redshifts (see left and central panels in figure 3.37), and compared it to the observation for SPT2349-56 (see right panel in figure 3.37). We encounter that our simulated protocluster show a similar integrated gas-mass value for all the three runs.

Putting both findings together we may conclude that our simulations are inefficient when producing stars. However, to understand better the origin of the discrepancies in the SFR between observation and simulations we calculated the correlation between the stellar mass and the SFR of the 10 most massive galaxies inside the most massive cluster in g1212639. Figure 3.38 shows the results obtained together with several observations for redshifts $z = 2.3$ and $z = 4.3$. The squares, triangles and diamonds represent the galaxies for the simple, SNe and AGN runs (where the BCGs have a red dot in the center). In the left panel of figure 3.37 the red solid line represents the main sequence (MS) of star-forming galaxies, which was derived by Whitaker et al. (2014) by considering star-forming galaxies selected in UVJ colours in the redshift range $2 \leq z \leq 2.5$. The red dashed line is the red sequence at $z = 2.3$ from the paper by Schreiber et al. (2015), but corrected to a Chabrier IMF in order to compare it with our results. Green circles and blue squares are galaxies data from the protoclusters of Gómez-Guijarro et al. (2019) and the cluster of Wang et al. (2018) respectively.

As portrayed in figure 3.37, the SFRs of our simulated cluster galaxies follow the red sequence for the high mass end but are below the observed relation for the low mass end by a factor of ~ 2 to 3. In the case of the AGN run the drop is even higher for smaller galaxies, which most probably is related to the strong quenching effect of AGN in star formation in small halos. This discrepancy in SFR at $z \sim 2$ has been reported before and has to do with the general inconsistency between observations and simulations around the peak of star formation in simulations (see i.e. Davé et al., 2016; Xie et al., 2017).

The right panel in figure 3.37 shows the same symbol pattern for our simulated galaxies as explained before. The red solid line stays for the main sequence of field galaxies at $4 \leq z \leq 4.8$ as observed by Steinhardt et al. (2014). The blue points are galaxies in SPT2349-56 as reported by Hill et al. (2020), who updated the values of SFR of Miller et al. (2018) and estimated the mass of single galaxies through their measured line-widths. At $z \sim 4.3$ simulations show a fairly good agreement with observations with no departure from the normalisation of the MS. Nevertheless, contrarily to our simulated galaxies, the galaxies in SPT2349-56 are scattered around the MS with a few but strong starburst. This points to a different interpretation of the SFR discrepancy. It seems that the real problem is not an inefficient star production, but rather that observed galaxies at high redshift suffer stronger star formation burst than simulated galaxies. This is further confirmed by the correct stellar to halo mass relations observed at lower redshifts (see section 3.3.5 for further details). In short, simulations show a correct (and sometimes even too high) amount of total star production at low redshifts, but also show too low SFRs at $z \sim 4$, which leads to the conclusion that we are missing in our simulations some mechanism that takes place inside galaxy clusters at high redshifts, producing strong star-forming bursts.

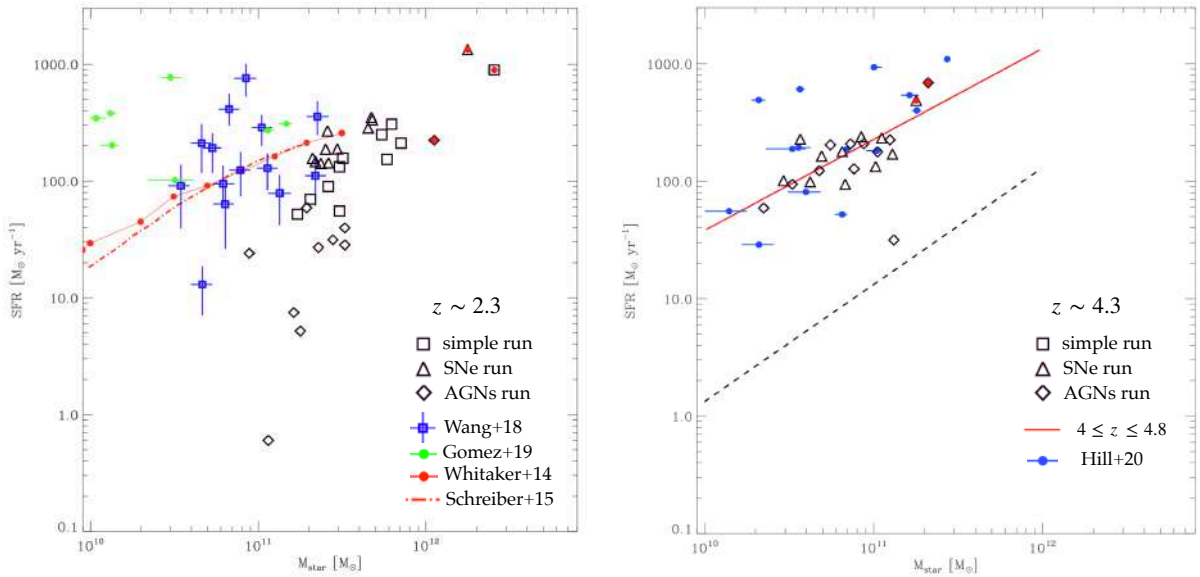

Figure 3.38: SFR as a function of galaxy stellar mass at $z \sim 2.3$ (left panel) and $z \sim 4.3$ (right panel). The black squares, triangles and diamonds stand for the values of the 10 most massive substructures inside the cluster for the simple, SNe and AGN run respectively. In the left panel the red solid and dashed lines are observational data from Whitaker et al. (2014) and Schreiber et al. (2015) respectively. Green dots and blue squares are galaxies from the protoclusters of Gómez-Guijarro et al. (2019) and the cluster of Wang et al. (2018) respectively. In the right panel the red line is observational data from Steinhardt et al. (2014). Blue dots represent galaxies of SPT2349-56 as analysed in Hill et al. (2020).

3.3.4 Mass Fractions and Scaling Relations

Galaxy clusters have their origin in the peaks of primordial fluctuations in the density field of the early Universe, and as such their growth contains a lot of information about our Universe and LSS. Scaling relations are particularly interesting as they link cluster observables with the underlying true halo mass, which enables the use of galaxy cluster samples for the measurement of cosmological parameters (Haiman et al., 2001; Carlstrom et al., 2002). Scaling relations can suffer the effects of non gravitational phenomena like star formation and AGN feedback, and thus they provide an observational tool to study high energetic energy phenomena in clusters of galaxies and the thermodynamic history of massive cosmic halos (e.g. Mohr et al., 1999; Pratt et al., 2010; Young et al., 2011).

There have been many studies related to this scaling relations from the observational (Zhang et al., 2011; Lin et al., 2012; Rozo et al., 2013; Lin et al., 2017) and from the hydrodynamical simulation side (e.g. Bryan and Norman, 1998; Nagai et al., 2007; Truong et al., 2018; Pillepich et al., 2018).

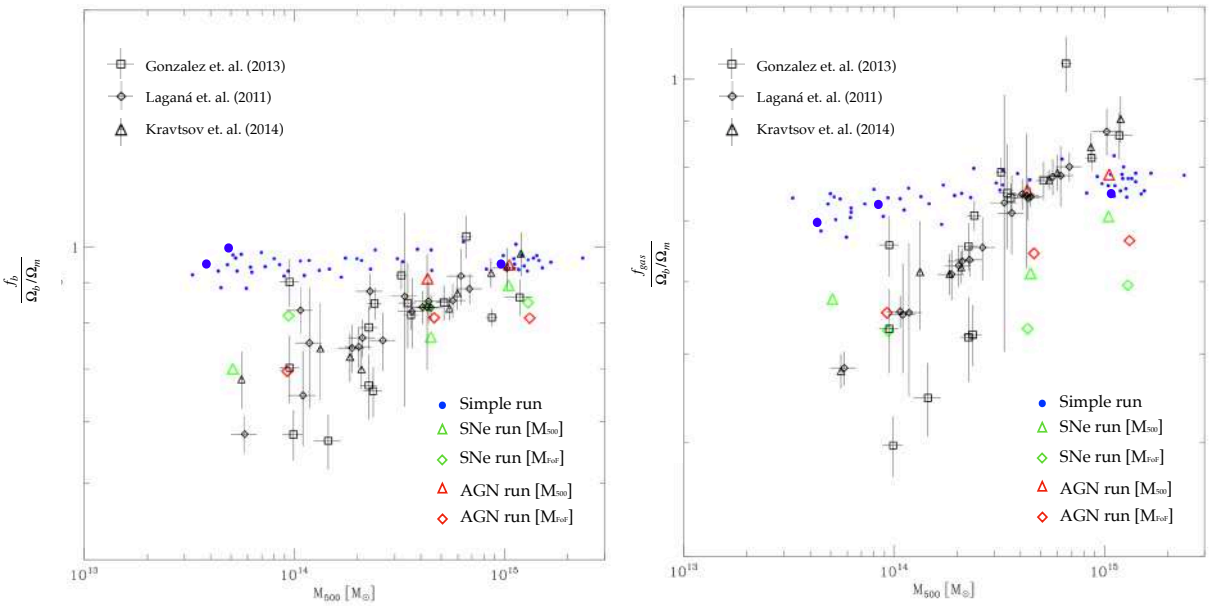

Figure 3.39: Baryon and gas fractions as function of cluster mass in our simulated clusters. The blue dots show the values for all the clusters in the Compass set runned with our simple subgrid model. The oversized blue dots stand for the three clusters in g1212639. The green and red diamonds stand for the baryon and gas fractions in the SNe and AGN runs considering all the mass assigned ot the clusters by SUBFIND. The triangles show the same relation considering only the particles inside M_{500}. The lowest mass cluster in the AGN run does not have a corresponding M_{500} value and thus only the value of the total mass is presented. Observational data are over-plotted in black with their corresponding uncertainties (Laganá et al., 2011; Gonzalez et al., 2013; Kravtsov et al., 2018).

We studied the effect of our subgrid physics in the final baryon, gas, stellar and cold baryon fraction relation with cluster mass and compared our results with the tight correlations appearing in observations. Figure 3.39 shows total baryon and gas fractions for our simple, SNe and AGN simulations (blue, green and red symbols respectively). The different symbols for the SNe and AGN runs stand for considering the total FoF group (diamonds) or just particles inside M_{500} (triangles). In this two panels we can see clearly how the simple run fails at reproducing the slope of the two relations. When adding a more detailed description of stellar feedback the results improved noticeably, but only when adding AGN are we able to reproduce results in concordance with observations for both relations, specially for the high mass.

The case of the stellar and cold fraction is more complicated. Even if the implementation of stellar and AGN feedback seems to improve our results, we cannot reproduce the slope seen in observations due to an overproduction of stars at the high mass end 3.40. Indeed our cold baryon and stellar fractions are too high for clusters with masses

$M_{500} \geq 5 \times 10^{14}$ $M_{\odot}$.

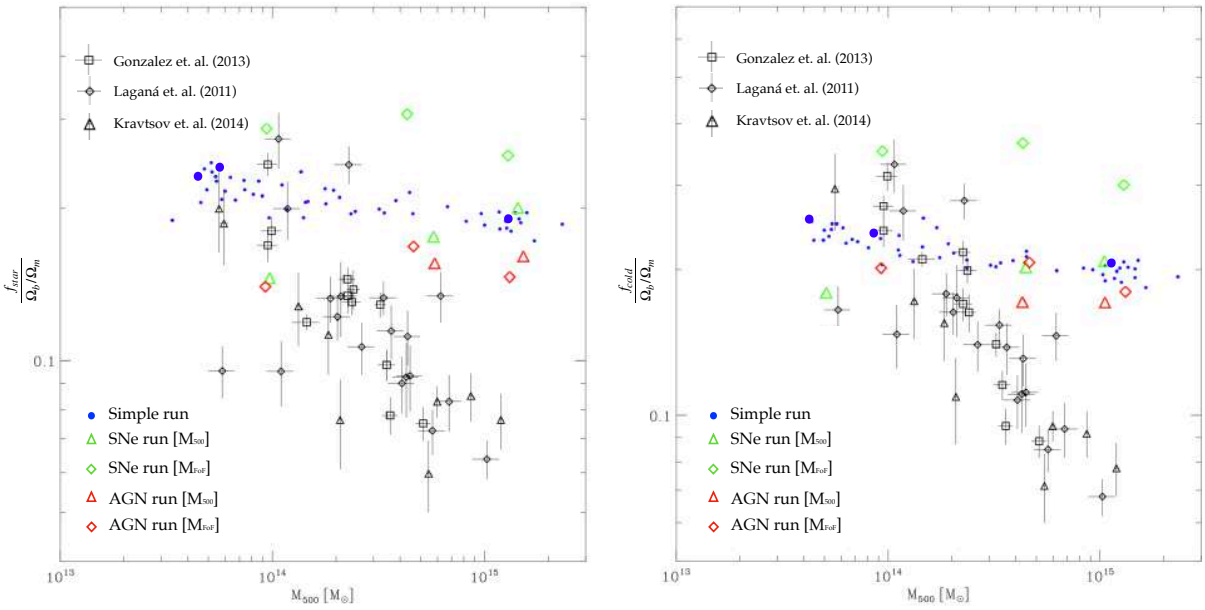

Figure 3.40: Stellar and cold baryon fractions as function of cluster mass in our simulated clusters. Same as in figure 3.39, the blue dots show the values for all the clusters in the Compass set runned with our simple subgrid model. The oversized blue dots stand for the three clusters in g1212639. The green and red diamonds stand for the baryon and gas fractions in the SNe and AGN runs considering all the mass assigned to the clusters by SUBFIND. The triangles show the same relation considering only the particles inside M_{500}. The lowest mass cluster in the AGN run does not have a corresponding M_{500} value and thus only the value of the total mass is presented. Observational data are over-plotted in black with their corresponding uncertainties.

3.3.5 Stellar to Halo Mass Relation

In order to further study the link between the cluster galaxies and their dark matter halos, we looked into the stellar to halo mass relation (SHMR) of the galaxies in our simulations at $z \sim 0$. This relation provides an insight into the connection between the baryonic properties of galaxies and the dark matter halos they reside in. Because of the unusual dense environment of clusters, the evolution of galaxies inside them is driven by different mechanisms than the ones affecting field. Because of this particular environment, satellite galaxies inside clusters are thought to evolve differently than the centrals, which in the course of their history are continuously growing by accreting matter. Satellites are expected to be subject to destructive influence by their host, and their dark matter will be gradually stripped by tidal forces (Gao et al., 2004; Nagai and Kravtsov, 2005; Giocoli et al., 2008; Xie et al., 2015; Rhee et al., 2017). These differences in evolution are expected

to leave an imprint in relations like the SHMR.

Figure 3.41a shows the SHMR for satellite galaxies (green dots) and BCGs (red dots) in clusters ranging from $1 \times 10^{13} \leq M_{200} \leq 7 \times 10^{15}$ form the MAGNETICUM simulation boxes (BOX0,B0X2b and BOX4; see section 2 for further details on these boxes). Over-plotted are observational data for BCGs in clusters at $z \sim 0$ presented by Gonzalez et al. (2013) and Kravtsov et al. (2018) and some data for satellite galaxies presented in the paper by Niemiec et al. (2017).

The difference in the evolutionary paths are clearly imprinted in the SHMR observed for simulated satellites and BCGs. Even if both galaxy sets follow the same trend, satellite galaxies are shifted towards lower halo masses compared to centrals. This has been also observationally suggested by gravitational lensing measurements (see i.e. Limousin et al., 2007; Natarajan et al., 2009; Sifón et al., 2015; Niemiec et al., 2017; Sifón et al., 2018) and also by measurements calibrated by abundance matching technique (Vale and Ostriker, 2004; Rodríguez-Puebla et al., 2017).

Observations for satellite galaxies lie within the values we obtained in our simulation sample. In the case of the BCGs, the observational data is in agreement with our most massive centrals, although we do have a small overproduction of stars. The BCGs belonging to BOX0 (circled with a dashed line) show a lower stellar content than what would be expected following the trend for the less massive BCGs. As there is no obvious physical reason for this behaviour, it may possibly have to do with a resolution effect, as BOX0 is the lowest resolution run of the three boxes. However, further studies need to be done in order to confirm or contradict this statement.

In panels b,c and d of figure 3.41 we over-plotted the results for our central and satellite galaxies in our most massive halo in region g1212639, for the three different subgrid physics runs. Satellite galaxies clearly follow the same trend as those in the MAGNETICUM boxes for the three runs, although the quench in star formation is obvious when adding AGN (see panel d). Indeed, in the case of the AGN run, satellite galaxies lie closer to the central values calculated from observations. When it comes to the BCG (oversized blue dot), the simple and SNe runs overproduce the amount of stars. It is only when we add AGN that we get the BCG to have a stellar vs halo mass relation in accordance with observations. This highlights again the special importance of AGN feedback in central cluster galaxies.

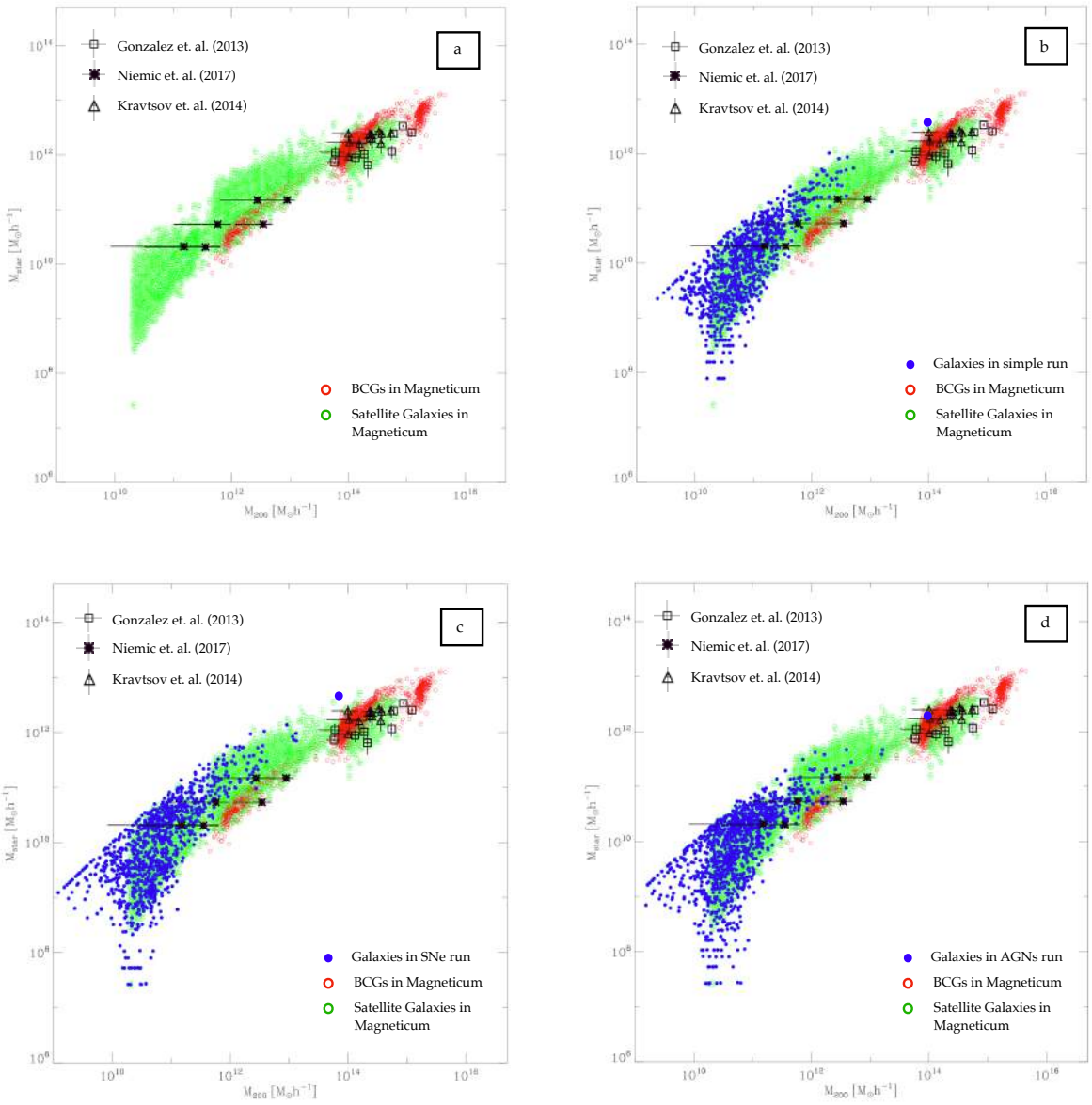

Figure 3.41: Stellar to halo mass relation for simulated clusters and observations at $z \sim 0$. Red and green circles represent the values for the central and satellite galaxies in boxes 0, 2b and 4 of our Magneticum Pathfinder simulation suit. Blue dots stand for the galaxies in our most massive galaxy cluster in g1212639, where the central is plotted as an oversized blue dot. Panels b, c and d show the results for the simple, SNe and AGN run respectively. The black symbols represent observational data of BCGs taken from Gonzalez et al. (2013) (squares) and Kravtsov et al. (2018) (triangles), and of satellite galaxies reported by Niemiec et al. (2017) (stars) K, all of them with their corresponding uncertainties.

3.4 Overview

As we have seen in this chapter, protoclusters of galaxies are structures that show a wide variety of internal structures and morphological evolutions. At low redshifts, galaxy clusters show compositions, which in lie many cases far away from virialization, with chains of galaxies in the process of assembling and merging. The high redshift total masses show a loose correlation with final cluster masses. So much so, that high mass ranked clusters at high redshifts in a Lagrangian region might end low ranked at low redshifts. At low redshifts, all clusters follow the observed relation between BCG stellar mass and final cluster mass.

By running the same Lagrangian region with three different subgrid physics prescriptions we were able to further comprehend the effect of SNe and AGN in protocluster formation and evolution. AGN shows a very pronounced effect in quenching star formation, visualized in the earlier fading of the star forming branch of the temperature vs density diagrams for the AGN run. The inclusion of AGN reduces overcooling and thus causes an improvement in the temperature profile of the most massive cluster. Nevertheless, our most massive simulated cluster in g1212639 does not achieve to mimic the temperature profiles derived from observations.

The SFR vs stellar mass relation at high redshifts tends to be lower in the AGN run, which brought the BCG closer to the observational result but over-quenched star formation in smaller galaxies. With a similar gas mass content profile than the one observed in cluster SPT2349-56, the most massive cluster in our simulated Lagrangian region shows a too low SFR profile at high redshifts, with no improvement when including AGN. In turn, the AGN run reproduces very well the observed total SFR at low redshifts, while our other two runs show a too high SFR.

Gas and baryon fractions improve dramatically when adding AGNs, matching the values obtained from observations. Meanwhile, the values for the stellar and cold fractions, even if they are better in the AGN run, still lie above the observed ones for the clusters at the high mass end. The low redshift SHMR of sattelite galaxies inside the most massive cluster lies within the expected values for the three runs. The central galaxy, however, shows a too high stellar mass in the simple and SN runs, which gets fixed with the addition of AGN.

Overall, we see an improvement of our results when adding prescriptions for BH growth and AGN feedback. We reproduce the correct SHMR for all the galaxies in our most massive cluster and correct SFRs at low redshifts. However, despite having the right amounts of gaseous mass at high redshifts and even ending with too high stellar and cold baryon fractions at low redshifts, our clusters are unable of reproducing the high SFR profiles observed in high redshifts protoclusters.

Chapter 4

Conclusions

Galaxy clusters are large scale objects with an enormous complexity due to the interplay of non-linear processes acting at many different scales. The dynamical range of cluster formation is enormously wide; it goes from the collapse of fluctuations at tens of cMpc to highly energetic processes that affect observable properties but act at subparsec scales (Voit, 2005; Allen et al., 2011; Kravtsov and Borgani, 2012). Thus, the formation of a cluster is a unique process that allows us to study the material that formed inside galaxies and the material that did not, all at the same time. This provides us with a much more complete picture of galaxy formation, and enables the simultaneous study of fundamental cosmological parameters, gravity and different aspects of hydrodynamics. As a result, understanding the processes involved in the formation and evolution of protoclusters has become paramount for modern cosmologists and astrophysicists.

The difficulties associated with observational biases and constraints, make it difficult to study the phenomena taking place in (proto)cluster of galaxies with observations alone. Fortunately, the increasing computational power and the continuous development of improved algorithms, allow researchers to perform new hydrodynamical cosmological simulations with higher resolutions and more complex subgrid physics prescriptions than previously possible. These improved simulations allow us to further comprehend the mechanisms taking place in these large scale structures. Even so, it is unclear to which extent some energetic processes, like star formation, stellar feedback and evolution or AGN feedback leave an imprint in (proto)cluster properties. Moreover, no scientific consensus has been reached on how to correctly implement all these processes in numerical simulations.

Regarding the current status of protocluster research, the central goal of this work has been to study the effects of such processes in the protocluster properties of our cosmological hydrodynamical zoom simulation sample of massive galaxy clusters. Our simulations set, called Compass, contains 24 Lagrangian regions, resulting in a total number of 73 galaxy clusters with $M_{vir} \geq 10^{14}\mathrm{M}_{\odot}$, of which 24 have final virial masses $M_{vir} \geq 10^{15}\mathrm{M}_{\odot}$.

We run the complete sample with a simple subgrid model that has prescriptions for star-

formation, simple cooling and a simple stellar feedback in the form of SN driven winds. We studied the different types of morphologies and formation histories of our clusters, showing that as discovered by observations, our simulated (proto)clusters have a wide variety of internal morphological structures at all redshifts. A nice example of this, is the most massive cluster in the region g1483463, which shows a Virgo-like structure with a chain of galaxies in a clear assembly process at $z = 0$. Obviously, this cluster cannot be virialized, as it is still suffering a strong in-fall of matter, and thus it is expected to be far away from the state of equilibrium. This further shows evidence, that the virialization state of galaxy clusters can only be a first order approximation, working better in the centers of clusters which have a more evolved and dominating BCG. However, this rises the question of the extent to which the virialization approximation is introducing errors in the quantities inferred form observations.

We continued by analyzing our galaxy (proto)clusters correlations between total masses, stellar masses, SFRs and substructure content at high and low redshifts. Contrary to what is commonly assumed in observations, we showed that the high redshift protocluster mass is only loosely correlated with the final cluster mass. Thus, the protocluster mass does not seem to be a good proxy for final cluster masses. Surprisingly, we have found a mild correlation between the structure richness at high and low redshifts. A high number of galaxies in a structure generally means also a higher number of galaxy-galaxy interactions that will enhance astrophysical processes like star formation. Thus, it would be interesting to further explore the relation of cluster richness with other quantities, such as low redshift total mass or stellar content.

In order to study the effects of star formation, stellar feedback and evolution, and AGN feedback in our (proto)cluster sample, we chose the Lagrangian region g1212639 and rerun it with two more subgrid prescriptions: one adding metals, stellar evolution, AGB yields and SNe feedback and another one adding also BH growth and AGN feedback. In non of the three different runs did we see any outstanding differences in the mass growth of the three clusters. In the temperature vs density diagrams the AGN run showed an earlier fading of the star formation branch, hinting to an earlier quenching of star-formation due to the energy injected into the gas by AGN feedback.

Next, we focused on the most massive cluster of the g1212639 Lagrangian region. Its temperature profile increasingly improved with the inclusion of SNe and AGN subgrid physics prescriptions, but still remained far away from observational results. It was previously unclear whether additional subgrid physics prescriptions for BHs and AGN feedback would change the SFR history in galaxy clusters. Our study has shown, that the peak of SFR is displaced to higher redshifts in the AGN run, which could be an indicator that AGN accelerate galaxy cluster evolution. Future studies will look at the combined effect of our AGN prescription and a resolution increase of the zoom Lagrangian region on the SFR peak of our clusters. The low redshift BCG SFR within a 30 kpc aperture is higher than observations in the simple and SN runs, but matches observations well for the AGN

run. However for the latter, the sSFR is lower than the values inferred by McDonald et al. (2018), which points towards a slightly higher stellar mass cluster content than what would be expected for the existing low redshift SFR.

We compared our simulated cluster (with a virial mass $M_{vir} = 1.3 \times 10^{13}$ $M_{\odot}$ at $z \sim 4.2$) with the observed cluster SPT2349-56 found at $z \sim 4.3$, which has a virial mass of $M_{vir} = 2 \times 10^{13}$ $M_{\odot}$. The gas mass profile is very similar between the observed protocluster and our three simulation runs, in fact any differences can be attributed to the total protocluster mass. However, the SFR profile is 4 times lower in all our simulations than that of SPT2349-56. In order to understand this discrepancy, we studied the galaxies conforming SPT2349-56 and compared their SFR-stellar mass relation with the one of our simulated clusters, showing that our galaxies follow the main sequence relation, while galaxies in SPT2349-56 are scattered around the main sequence with a few but strong starbursts. Moreover, galaxies in our cluster follow the SHMR reported by Gonzalez et al. (2013); Kravtsov et al. (2018); Niemiec et al. (2017), thus their final stellar content is in agreement with observations.

All the above results lead to the conclusion that our simulations are producing the right amount of stars, but more steadily than what seems to be the case in clusters like SPT2349-56, i.e. our simulations are unable to reproduce the starbursts observed in clusters at high redshifts. This problem, common to all simulations of protoclusters (Saro et al., 2008; Granato et al., 2015), could be a sign that we are missing some key physical process in our subgrid prescriptions that leads to the observed starbursts in protocluster galaxies at high redshifts. In order to establish if our problem is indeed physical and not a numerical artifact, it would be highly interesting to study the evolution of the SFRs in protoclusters when carrying out these simulations at the higher resolutions allowed by the Compass set.

Bibliography

Aguirre, A., L. Hernquist, N. Katz, J. Gardner, and D. Weinberg
2000. Enrichment of the intergalactic medium by radiation pressure driven dust efflux. *The Astrophysical Journal*, 556.

Aguirre, A., L. Hernquist, J. Schaye, D. H. Weinberg, N. Katz, and J. Gardner
2001. Metal enrichment of the intergalactic medium atz = 3 by galactic winds. 560(2):599–605.

Aguirre, A., J. Schaye, and E. Quataert
2001. Problems for Modified Newtonian Dynamics in Clusters and the Lyα Forest? , 561(2):550–558.

Allen, S. W., A. E. Evrard, and A. B. Mantz
2011. Cosmological parameters from observations of galaxy clusters. *Annual Review of Astronomy and Astrophysics*, 49:409–470.

Angulo, R. E., V. Springel, S. D. M. White, A. Jenkins, C. M. Baugh, and C. S. Frenk
2012. Scaling relations for galaxy clusters in the Millennium-XXL simulation. , 426(3):2046–2062.

Baldi, A., S. Ettori, P. Mazzotta, P. Tozzi, and S. Borgani
2007. A Chandra Archival Study of the Temperature and Metal Abundance Profiles in Hot Galaxy Clusters at 0.1 ¡~z ¡~0.3. , 666(2):835–845.

Baldi, A., S. Ettori, S. Molendi, and F. Gastaldello
2012. Self-similarity of temperature profiles in distant galaxy clusters: the quest for a universal law. , 545:A41.

Ball, R., J. O. Burns, and C. Loken
1993. The radio properties of cd galaxies in abell clusters. ii-the vla sample. *The Astronomical Journal*, 105:53–66.

Balogh, M. L., F. R. Pearce, R. G. Bower, and S. T. Kay
2001. Revisiting the cosmic cooling crisis. *Monthly Notices of the Royal Astronomical Society*, 326(4):1228–1234.

Barkana, R. and A. Loeb
2001. In the beginning: the first sources of light and the reionization of the universe. , 349(2):125–238.

Bassini, L., E. Rasia, S. Borgani, G. Granato, C. Ragone-Figueroa, V. Biffi, A. Ragagnin, K. Dolag, G. Murante, N. Napolitano, G. Taffoni, L. Tornatore, and Y. Wang
2020. The dianoga simulations of galaxy clusters: characterising star formation in protoclusters. *Astronomy Astrophysics*, 642.

Battaglia, N., J. Bond, C. Pfrommer, and J. Sievers
2013. On the cluster physics of sunyaev-zel'dovich and x-ray surveys. iii. measurement biases and cosmological evolution of gas and stellar mass fractions. *The Astrophysical Journal*, 777(2):123.

Baugh, C. M.
2006. A primer on hierarchical galaxy formation: the semi-analytical approach. *Reports on Progress in Physics*, 69(12):3101–3156.

Baugh, C. M., E. Gaztañaga, and G. Efstathiou
1995. A comparison of the evolution of density fields in perturbation theory and numerical simulations - II. Counts-in-cells analysis. *Monthly Notices of the Royal Astronomical Society*, 274(4):1049–1070.

Beck, A. M., G. Murante, A. Arth, R.-S. Remus, A. F. Teklu, J. M. F. Donnert, S. Planelles, M. C. Beck, P. Förster, M. Imgrund, K. Dolag, and S. Borgani
2015. An improved SPH scheme for cosmological simulations. *Monthly Notices of the Royal Astronomical Society*, 455(2):2110–2130.

Bellstedt, S., D. A. Forbes, A. J. Romanowsky, R.-S. Remus, A. R. H. Stevens, J. P. Brodie, A. Poci, R. McDermid, A. Alabi, L. Chevalier, C. Adams, A. Ferré-Mateu, A. Wasserman, and V. Pandya
2018. The SLUGGS survey: a comparison of total-mass profiles of early-type galaxies from observations and cosmological simulations, to ∼4 effective radii. , 476(4):4543–4564.

Benz, W.
1990. Smooth Particle Hydrodynamics - a Review. In *Numerical Modelling of Nonlinear Stellar Pulsations Problems and Prospects*, J. R. Buchler, ed., P. 269.

Berger, M. and P. Colella
1989. Local adaptive mesh refinement for shock hydrodynamics. *Journal of Computational Physics*, 82(1):64–84.

Bertschinger, E.
1985. Self-similar secondary infall and accretion in an einstein-de sitter universe. *The Astrophysical Journal Supplement Series*, 58:39–65.

Bertschinger, E.
1998. Simulations of structure formation in the universe. *Annual Review of Astronomy and Astrophysics*, 36(1):599–654.

Best, P., A. Von Der Linden, G. Kauffmann, T. Heckman, and C. Kaiser
2007. On the prevalence of radio-loud active galactic nuclei in brightest cluster galaxies: implications for agn heating of cooling flows. *Monthly Notices of the Royal Astronomical Society*, 379(3):894–908.

Biffi, V., K. Dolag, and H. Böhringer
2012. Investigating the velocity structure and X-ray observable properties of simulated galaxy clusters with PHOX. *Monthly Notices of the Royal Astronomical Society*, 428(2):1395–1409.

Biffi, V., K. Dolag, T. H. Reiprich, A. Veronica, M. E. Ramos-Ceja, E. Bulbul, N. Ota, and V. Ghirardini
2021. The eROSITA view of the Abell 3391/95 field: a case study from the Magneticum cosmological simulation. *arXiv e-prints*, P. arXiv:2106.14542.

Biffi, V., S. Planelles, S. Borgani, D. Fabjan, E. Rasia, G. Murante, L. Tornatore, K. Dolag, G. L. Granato, M. Gaspari, and A. M. Beck
2017. The history of chemical enrichment in the intracluster medium from cosmological simulations. *Monthly Notices of the Royal Astronomical Society*, 468(1):531–548.

Biffi, V., S. Planelles, S. Borgani, E. Rasia, G. Murante, D. Fabjan, and M. Gaspari
2018. The origin of ICM enrichment in the outskirts of present-day galaxy clusters from cosmological hydrodynamical simulations. , 476(2):2689–2703.

Bîrzan, L., D. A. Rafferty, B. McNamara, M. Wise, and P. E. Nulsen
2004. A systematic study of radio-induced x-ray cavities in clusters, groups, and galaxies. *The Astrophysical Journal*, 607(2):800.

Bland-Hawthorn, J.
1995. Multi-wavelength observations of galactic winds. *Publications of the Astronomical Society of Australia*, 12(2):190–196.

Bleem, L. E., B. Stalder, T. de Haan, K. A. Aird, S. W. Allen, D. E. Applegate, M. L. N. Ashby, M. Bautz, M. Bayliss, B. A. Benson, S. Bocquet, M. Brodwin, J. E. Carlstrom, C. L. Chang, I. Chiu, H. M. Cho, A. Clocchiatti, T. M. Crawford, A. T. Crites, S. Desai, J. P. Dietrich, M. A. Dobbs, R. J. Foley, W. R. Forman, E. M. George, M. D. Gladders, A. H. Gonzalez, N. W. Halverson, C. Hennig, H. Hoekstra, G. P. Holder, W. L. Holzapfel, J. D. Hrubes, C. Jones, R. Keisler, L. Knox, A. T. Lee, E. M. Leitch, J. Liu, M. Lueker, D. Luong-Van, A. Mantz, D. P. Marrone, M. McDonald, J. J. McMahon, S. S. Meyer, L. Mocanu, J. J. Mohr, S. S. Murray, S. Padin, C. Pryke, C. L. Reichardt, A. Rest, J. Ruel, J. E. Ruhl, B. R. Saliwanchik, A. Saro, J. T. Sayre, K. K. Schaffer,

T. Schrabback, E. Shirokoff, J. Song, H. G. Spieler, S. A. Stanford, Z. Staniszewski, A. A. Stark, K. T. Story, C. W. Stubbs, K. Vanderlinde, J. D. Vieira, A. Vikhlinin, R. Williamson, O. Zahn, and A. Zenteno
2015. Galaxy Clusters Discovered via the Sunyaev-Zel'dovich Effect in the 2500-Square-Degree SPT-SZ Survey. , 216(2):27.

Blumenthal, G. R., S. M. Faber, J. R. Primack, and M. J. Rees
1984. Formation of galaxies and large-scale structure with cold dark matter. , 311:517–525.

Bocquet, S., A. Saro, K. Dolag, and J. J. Mohr
2016. Halo mass function: baryon impact, fitting formulae, and implications for cluster cosmology. , 456(3):2361–2373.

Bonafede, A., G. Brunetti, F. Vazza, A. Simionescu, G. Giovannini, E. Bonnassieux, T. W. Shimwell, M. Brüggen, R. J. van Weeren, A. Botteon, M. Brienza, R. Cassano, A. Drabent, L. Feretti, F. de Gasperin, F. Gastaldello, G. di Gennaro, M. Rossetti, H. J. A. Rottgering, C. Stuardi, and T. Venturi
2021. The Coma Cluster at LOw Frequency ARray Frequencies. I. Insights into Particle Acceleration Mechanisms in the Radio Bridge. , 907(1):32.

Bonafede, A., K. Dolag, F. Stasyszyn, G. Murante, and S. Borgani
2011. A non-ideal magnetohydrodynamic GADGET: simulating massive galaxy clusters. , 418(4):2234–2250.

Bond, J. R., L. Kofman, and D. Pogosyan
1996. How filaments of galaxies are woven into the cosmic web. *Nature*, 380(6575):603–606.

Borgani, S., F. Governato, J. Wadsley, N. Menci, P. Tozzi, T. Quinn, J. Stadel, and G. Lake
2002. The effect of non-gravitational gas heating in groups and clusters of galaxies. *Monthly Notices of the Royal Astronomical Society*, 336(2):409–424.

Borgani, S. and L. Guzzo
2001. X-ray clusters of galaxies as tracers of structure in the universe. *Nature*, 409(6816):39–45.

Borgani, S. and A. Kravtsov
2011a. Cosmological simulations of galaxy clusters. *Advanced Science Letters*, 4(2):204–227.

Borgani, S. and A. Kravtsov
2011b. Cosmological simulations of galaxy clusters. *Advanced Science Letters*, 4(2):204–227.

Borgani, S., G. Murante, V. Springel, A. Diaferio, K. Dolag, L. Moscardini, G. Tormen, L. Tornatore, and P. Tozzi
2004. X-ray properties of galaxy clusters and groups from a cosmological hydrodynamical simulation. , 348(3):1078–1096.

Bower, R., I. Mccarthy, and A. Benson
2008. The flip side of galaxy formation: A combined model of galaxy formation and cluster heating. *Monthly Notices of the Royal Astronomical Society*, 390:1399 – 1410.

Bower, R. G., A. J. Benson, and R. A. Crain
2012. What shapes the galaxy mass function? Exploring the roles of supernova-driven winds and active galactic nuclei. , 422(4):2816–2840.

Bower, R. G., S. Morris, R. Bacon, R. Wilman, M. Sullivan, S. Chapman, R. Davies, P. De Zeeuw, and E. Emsellem
2004. Deep sauron spectral imaging of the diffuse lyman α halo lab1 in ssa 22. *Monthly Notices of the Royal Astronomical Society*, 351(1):63–69.

Braun, H. and W. Schmidt
2012. A semi-analytic model of the turbulent multi-phase interstellar medium. *Monthly Notices of the Royal Astronomical Society*, 421(3):1838–1860.

Bromm, V., P. S. Coppi, and R. B. Larson
2002. The formation of the first stars. i. the primordial star-forming cloud. 564(1):23–51.

Bryan, G. L. and M. L. Norman
1998. Statistical Properties of X-Ray Clusters: Analytic and Numerical Comparisons. , 495(1):80–99.

Brüggen, M. and E. Scannapieco
2009. Self-regulation of agn in galaxy clusters.

Burns, J. O.
1990. The radio properties of cd galaxies in abell clusters. i-an x-ray selected sample. *The Astronomical Journal*, 99:14–30.

Carlstrom, J. E., G. P. Holder, and E. D. Reese
2002. Cosmology with the Sunyaev-Zel'dovich Effect. , 40:643–680.

Casey, C. M., D. Narayanan, and A. Cooray
2014. Dusty star-forming galaxies at high redshift. *Physics Reports*, 541(2):45–161. Dusty star-forming galaxies at high-redshift.

Cavaliere, A., H. Gursky, and W. Tucker
1971. Extragalactic x-ray sources and associations of galaxies. *Nature*, 231(5303):437–438.

Chabrier, G.
2003. Galactic Stellar and Substellar Initial Mass Function. , 115(809):763–795.

Chandran, B. D. G., P. Sharma, and I. J. Parrish
2009. Plasma Physics in Clusters of Galaxies. In *astro2010: The Astronomy and Astrophysics Decadal Survey*, volume 2010, P. 41.

Chiang, Y.-K., R. Overzier, and K. Gebhardt
2013. Ancient light from young cosmic cities: Physical and observational signatures of galaxy proto-clusters. *The Astrophysical Journal*, 779(2):127.

Collet, C., N. Nesvadba, C. De Breuck, M. Lehnert, P. Best, J. Bryant, D. Dicken, H. Johnston, R. Hunstead, and D. Wylezalek
2015. Defying jet-gas alignment in two radio galaxies at z˜ 2 with extended light profiles: Similarities to brightest cluster galaxies. *Astronomy & Astrophysics*, 579:A89.

Cooray, A. and R. Sheth
2002. Halo models of large scale structure. , 372(1):1–129.

Cossins, P. J.
2010. *Smoothed Particle Hydrodynamics*. PhD thesis, -.

Crain, R. A., J. Schaye, R. G. Bower, M. Furlong, M. Schaller, T. Theuns, C. Dalla Vecchia, C. S. Frenk, I. G. McCarthy, J. C. Helly, A. Jenkins, Y. M. Rosas-Guevara, S. D. M. White, and J. W. Trayford
2015. The EAGLE simulations of galaxy formation: calibration of subgrid physics and model variations. , 450(2):1937–1961.

Croft, R. A. C., D. H. Weinberg, N. Katz, and L. Hernquist
1998. Cosmology from the structure of the lya forest. In *Large Scale Structure: Tracks and Traces*, V. Mueller, S. Gottloeber, J. P. Muecket, and J. Wambsganss, eds., Pp. 69–75.

Cuesta, A., F. Prada, A. Klypin, and M. Moles
2008. The virialized mass of dark matter haloes. *Monthly Notices of the Royal Astronomical Society*, 389(1):385–397.

Dave, R., N. Katz, and D. H. Weinberg
2002. X-ray scaling relations of galaxy groups in a hydrodynamic cosmological simulation. *The Astrophysical Journal*, 579(1):23.

Davé, R., R. Thompson, and P. F. Hopkins
2016. MUFASA: galaxy formation simulations with meshless hydrodynamics. , 462(3):3265–3284.

Davies, L. J. M., C. d. P. Lagos, A. Katsianis, A. S. G. Robotham, L. Cortese, S. P. Driver, M. N. Bremer, M. J. I. Brown, S. Brough, M. E. Cluver, M. W. Grootes, B. W. Holwerda, M. Owers, and S. Phillipps
2019. Galaxy And Mass Assembly (GAMA): The sSFR-M_* relation part I - σ_{sSFR}-M_* as a function of sample, SFR indicator, and environment. , 483(2):1881–1900.

Davis, M., G. Efstathiou, C. S. Frenk, and S. D. M. White
1985. The evolution of large-scale structure in a universe dominated by cold dark matter. *Astrophysical Journal*, 292:371–394.

Davis, M., J. Huchra, D. W. Latham, and J. Tonry
1982. A survey of galaxy redshifts. II. The large scale space distribution. , 253:423–445.

De Boni, C., H. Böhringer, G. Chon, and K. Dolag
2018. Evolution of the degree of substructures in simulated galaxy clusters. , 478(2):2086–2096.

De Lucia, G.
2007. How 'Heredity' and 'Environment' Shape Galaxy Properties. In *Cosmic Frontiers*, N. Metcalfe and T. Shanks, eds., volume 379 of *Astronomical Society of the Pacific Conference Series*, P. 257.

De Lucia, G. and J. Blaizot
2007. The hierarchical formation of the brightest cluster galaxies. *Monthly Notices of the Royal Astronomical Society*, 375(1):2–14.

De Lucia, G., G. Kauffmann, and S. D. White
2004. Chemical enrichment of the intracluster and intergalactic medium in a hierarchical galaxy formation model. *Monthly Notices of the Royal Astronomical Society*, 349(3):1101–1116.

Diaferio, A.
2004. *Outskirts of Galaxy Clusters (IAU C195): Intense Life in the Suburbs*, number 195. Cambridge University Press.

Dolag, K., S. Borgani, G. Murante, and V. Springel
2009. Substructures in hydrodynamical cluster simulations. , 399(2):497–514.

Dolag, K., S. Borgani, S. Schindler, A. Diaferio, and A. M. Bykov
2008. Simulation techniques for cosmological simulations. *Space science reviews*, 134(1):229–268.

Dolag, K., B. M. Gaensler, A. M. Beck, and M. C. Beck
2015. Constraints on the distribution and energetics of fast radio bursts using cosmological hydrodynamic simulations. *Monthly Notices of the Royal Astronomical Society*, 451(4):4277–4289.

Dolag, K., E. Komatsu, and R. Sunyaev
2016. SZ effects in the Magneticum Pathfinder simulation: comparison with the Planck, SPT, and ACT results. , 463(2):1797–1811.

Dolag, K., E. Mevius, and R.-S. Remus
2017. Distribution and Evolution of Metals in the Magneticum Simulations. *Galaxies*, 5(3):35.

Dolag, K., F. Vazza, G. Brunetti, and G. Tormen
2005. Turbulent gas motions in galaxy cluster simulations: the role of smoothed particle hydrodynamics viscosity. *Monthly Notices of the Royal Astronomical Society*, 364(3):753–772.

Dubois, Y., J. Devriendt, A. Slyz, and R. Teyssier
2012. Self-regulated growth of supermassive black holes by a dual jet–heating active galactic nucleus feedback mechanism: methods, tests and implications for cosmological simulations. *Monthly Notices of the Royal Astronomical Society*, 420(3):2662–2683.

Dubois, Y., S. Peirani, C. Pichon, J. Devriendt, R. Gavazzi, C. Welker, and M. Volonteri
2016. The HORIZON-AGN simulation: morphological diversity of galaxies promoted by AGN feedback. , 463(4):3948–3964.

Dubois, Y., C. Pichon, C. Welker, D. Le Borgne, J. Devriendt, C. Laigle, S. Codis, D. Pogosyan, S. Arnouts, K. Benabed, E. Bertin, J. Blaizot, F. Bouchet, J. F. Cardoso, S. Colombi, V. de Lapparent, V. Desjacques, R. Gavazzi, S. Kassin, T. Kimm, H. McCracken, B. Milliard, S. Peirani, S. Prunet, S. Rouberol, J. Silk, A. Slyz, T. Sousbie, R. Teyssier, L. Tresse, M. Treyer, D. Vibert, and M. Volonteri
2014. Dancing in the dark: galactic properties trace spin swings along the cosmic web. , 444(2):1453–1468.

Efstathiou, G.
2000. A model of supernova feedback in galaxy formation. , 317(3):697–719.

Efstathiou, G. and J. W. Eastwood
1981. On the clustering of particles in an expanding Universe. *Monthly Notices of the Royal Astronomical Society*, 194(3):503–525.

Einasto, J., A. Klypin, E. Saar, and S. Shandarin
1984. Structure of superclusters and supercluster formation - iii. quantitative study of the local supercluster. *Monthly Notices of the Royal Astronomical Society*, 206:529–558.

Einstein, A. and W. De Sitter
1932. On the relation between the expansion and the mean density of the universe. *Proceedings of the National Academy of Sciences of the United States of America*, 18(3):213.

Eke, V. R., J. F. Navarro, and M. Steinmetz
2001. The Power Spectrum Dependence of Dark Matter Halo Concentrations. , 554(1):114–125.

Fabjan, D., S. Borgani, L. Tornatore, A. Saro, G. Murante, and K. Dolag
2010a. Simulating the effect of active galactic nuclei feedback on the metal enrichment of galaxy clusters. *Monthly Notices of the Royal Astronomical Society*, 401(3):1670–1690.

Fabjan, D., S. Borgani, L. Tornatore, A. Saro, G. Murante, and K. Dolag
2010b. Simulating the effect of active galactic nuclei feedback on the metal enrichment of galaxy clusters. *Monthly Notices of the Royal Astronomical Society*, 401(3):1670–1690.

Fakhouri, O. and C.-P. Ma
2009. Environmental dependence of dark matter halo growth–i. halo merger rates. *Monthly Notices of the Royal Astronomical Society*, 394(4):1825–1840.

Ferland, G. J., K. T. Korista, D. A. Verner, J. W. Ferguson, J. B. Kingdon, and E. M. Verner
1998. CLOUDY 90: Numerical Simulation of Plasmas and Their Spectra. , 110(749):761–778.

Ferragamo, A., J. A. Rubiño-Martín, J. Betancort-Rijo, E. Munari, B. Sartoris, and R. Barrena
2020. Biases in galaxy cluster velocity dispersion and mass estimates in the small N_{gal} regime. , 641:A41.

Ferrarese, L., P. Côté, L. A. MacArthur, P. R. Durrell, S. D. J. Gwyn, P.-A. Duc, R. Sánchez-Janssen, M. Santos, J. P. Blakeslee, A. Boselli, F. Boyer, M. Cantiello, S. Courteau, J.-C. Cuillandre, E. Emsellem, T. Erben, G. Gavazzi, P. Guhathakurta, M. Huertas-Company, A. Jordán, A. Lançon, C. Liu, S. Mei, J. C. Mihos, E. W. Peng, T. H. Puzia, J. Roediger, D. Schade, J. E. Taylor, E. Toloba, and H. Zhang
2020. The next generation virgo cluster survey (NGVS). XIV. the discovery of low-mass galaxies and a new galaxy catalog in the core of the virgo cluster. 890(2):128.

Ferrarese, L. and D. Merritt
2000. A fundamental relation between supermassive black holes and their host galaxies. *The Astrophysical Journal Letters*, 539(1):L9.

Foley, R. J., K. Andersson, G. Bazin, T. de Haan, J. Ruel, P. A. R. Ade, K. A. Aird, R. Armstrong, M. L. N. Ashby, M. Bautz, B. A. Benson, L. E. Bleem, M. Bonamente, M. Brodwin, J. E. Carlstrom, C. L. Chang, A. Clocchiatti, T. M. Crawford, A. T. Crites, S. Desai, M. A. Dobbs, J. P. Dudley, G. G. Fazio, W. R. Forman, G. Garmire, E. M. George, M. D. Gladders, A. H. Gonzalez, N. W. Halverson, F. W. High, G. P. Holder, W. L. Holzapfel, S. Hoover, J. D. Hrubes, C. Jones, M. Joy, R. Keisler, L. Knox, A. T. Lee, E. M. Leitch, M. Lueker, D. Luong-Van, D. P. Marrone, J. J. McMahon, J. Mehl,

S. S. Meyer, J. J. Mohr, T. E. Montroy, S. S. Murray, S. Padin, T. Plagge, C. Pryke, C. L. Reichardt, A. Rest, J. E. Ruhl, B. R. Saliwanchik, A. Saro, K. K. Schaffer, L. Shaw, E. Shirokoff, J. Song, H. G. Spieler, B. Stalder, S. A. Stanford, Z. Staniszewski, A. A. Stark, K. Story, C. W. Stubbs, K. Vanderlinde, J. D. Vieira, A. Vikhlinin, R. Williamson, and A. Zenteno
2011. Discovery and Cosmological Implications of SPT-CL J2106-5844, the Most Massive Known Cluster at z¿1. , 731(2):86.

Forman, W., E. Kellogg, H. Gursky, H. Tananbaum, and R. Giacconi
1972. Observations of the extended x-ray sources in the perseus and coma clusters from uhuru. *The Astrophysical Journal*, 178:309–316.

Fraser-McKelvie, A., M. J. I. Brown, and K. A. Pimbblet
2014. The rarity of star formation in brightest cluster galaxies as measured by WISE. , 444:L63–L67.

Frye, B., T. Broadhurst, and N. Benítez
2002. Spectral evidence for widespread galaxy outflows at z¿ 4. *The Astrophysical Journal*, 568(2):558.

Galárraga-Espinosa, D., N. Aghanim, M. Langer, C. Gouin, and N. Malavasi
2020. Populations of filaments from the distribution of galaxies in numerical simulations. , 641:A173.

Gao, L., G. De Lucia, S. D. White, and A. Jenkins
2004. Galaxies and subhaloes in λcdm galaxy clusters. *Monthly Notices of the Royal Astronomical Society*, 352(2):L1–L5.

Gaspari, M., D. Eckert, S. Ettori, P. Tozzi, L. Bassini, E. Rasia, F. Brighenti, M. Sun, S. Borgani, S. D. Johnson, G. R. Tremblay, J. M. Stone, P. Temi, H.-Y. K. Yang, F. Tombesi, and M. Cappi
2019. The x-ray halo scaling relations of supermassive black holes. 884(2):169.

Geach, J., J. Dunlop, M. Halpern, I. Smail, P. Van der Werf, D. Alexander, O. Almaini, I. Aretxaga, V. Arumugam, V. Asboth, et al.
2017. The scuba-2 cosmology legacy survey: 850 μm maps, catalogues and number counts. *Monthly Notices of the Royal Astronomical Society*, 465(2):1789–1806.

Genel, S., M. Vogelsberger, V. Springel, D. Sijacki, D. Nelson, G. Snyder, V. Rodriguez-Gomez, P. Torrey, and L. Hernquist
2014. Introducing the Illustris project: the evolution of galaxy populations across cosmic time. , 445(1):175–200.

Gingold, R. A. and J. J. Monaghan
1977. Smoothed particle hydrodynamics: theory and application to non-spherical stars. , 181:375–389.

Giocoli, C., G. Tormen, and F. C. van den Bosch
2008. The population of dark matter subhaloes: mass functions and average mass-loss rates. , 386(4):2135–2144.

Gómez-Guijarro, C., G. E. Magdis, F. Valentino, S. Toft, A. W. S. Man, R. J. Ivison, K. Tisanić, D. van der Vlugt, M. Stockmann, S. Martin-Alvarez, and G. Brammer
2019. Compact Star-forming Galaxies as Old Starbursts Becoming Quiescent. , 886(2):88.

Gonzalez, A. H., S. Sivanandam, A. I. Zabludoff, and D. Zaritsky
2013. GALAXY CLUSTER BARYON FRACTIONS REVISITED. 778(1):14.

Gonzalez, A. H., D. Zaritsky, and A. I. Zabludoff
2007. A census of baryons in galaxy clusters and groups. *The Astrophysical Journal*, 666(1):147.

Gottlöber, S., A. Klypin, and A. V. Kravtsov
2001. Merging history as a function of halo environment. *The Astrophysical Journal*, 546(1):223.

Granato, G. L., C. Ragone-Figueroa, R. Domínguez-Tenreiro, A. Obreja, S. Borgani, G. De Lucia, and G. Murante
2015. The early phases of galaxy clusters formation in IR: coupling hydrodynamical simulations with GRASIL-3D. , 450(2):1320–1332.

Green, T. S., A. C. Edge, J. P. Stott, H. Ebeling, W. S. Burgett, K. C. Chambers, P. W. Draper, N. Metcalfe, N. Kaiser, R. J. Wainscoat, and C. Waters
2016. A multiwavelength photometric census of AGN and star formation activity in the brightest cluster galaxies of X-ray selected clusters. *Monthly Notices of the Royal Astronomical Society*, 461(1):560–577.

Gunn, J. E. and J. R. Gott III
1972. On the infall of matter into clusters of galaxies and some effects on their evolution. *The Astrophysical Journal*, 176:1.

Guo, Q., S. White, M. Boylan-Kolchin, G. De Lucia, G. Kauffmann, G. Lemson, C. Li, V. Springel, and S. Weinmann
2011. From dwarf spheroidals to cD galaxies: simulating the galaxy population in a ΛCDM cosmology. , 413(1):101–131.

Gursky, H., E. Kellogg, S. Murray, C. Leong, H. Tananbaum, and R. Giacconi
1971. A strong x-ray source in the coma cluster observed by uhuru. *The Astrophysical Journal*, 167:L81.

Guth, A. H. and S.-Y. Pi
1982. Fluctuations in the new inflationary universe. *Phys. Rev. Lett.*, 49:1110–1113.

Haiman, Z., J. J. Mohr, and G. P. Holder
2001. Constraints on Cosmological Parameters from Future Galaxy Cluster Surveys. , 553(2):545–561.

Hansen, S. H., A. V. Macció, E. Romano-Diaz, Y. Hoffman, M. Brüggen, E. Scannapieco, and G. S. Stinson
2011. THE TEMPERATURE OF HOT GAS IN GALAXIES AND CLUSTERS: BARYONS DANCING TO THE TUNE OF DARK MATTER. 734(1):62.

Hatch, N., R. Overzier, J. Kurk, G. Miley, H. Röttgering, and A. Zirm
2009. The growth and assembly of a massive galaxy at z 2. *Monthly Notices of the Royal Astronomical Society*, 395(1):114–125.

Heckman, T. M., K. R. Sembach, G. R. Meurer, C. Leitherer, D. Calzetti, and C. L. Martin
2001. On the escape of ionizing radiation from starbursts. 558(1):56–62.

Hill, R., S. Chapman, D. Scott, Y. Apostolovski, M. Aravena, M. Béthermin, C. M. Bradford, R. E. A. Canning, C. De Breuck, C. Dong, A. Gonzalez, T. R. Greve, C. C. Hayward, Y. Hezaveh, K. Litke, M. Malkan, D. P. Marrone, K. Phadke, C. Reuter, K. Rotermund, J. Spilker, J. D. Vieira, and A. Weiß
2020. Megaparsec-scale structure around the protocluster core SPT2349–56 at z = 4.3. *Monthly Notices of the Royal Astronomical Society*, 495(3):3124–3159.

Hirschmann, M., K. Dolag, A. Saro, L. Bachmann, S. Borgani, and A. Burkert
2014. Cosmological simulations of black hole growth: AGN luminosities and downsizing. , 442(3):2304–2324.

Hubble, E. P.
1925. Cepheids in spiral nebulae. *Popular Astronomy*, 33.

Hubble, E. P.
1926. Extragalactic nebulae. *The Astrophysical Journal*, 64.

Huchra, J. P. and M. J. Geller
1982. Groups of Galaxies. I. Nearby groups. , 257:423–437.

Hui, L. and N. Y. Gnedin
1997. Equation of state of the photoionized intergalactic medium. , 292(1):27–42.

Kaiser, N.
1986. Evolution and clustering of rich clusters. *Monthly Notices of the Royal Astronomical Society*, 222(2):323–345.

Karakas, A. and J. C. Lattanzio
2007. Stellar Models and Yields of Asymptotic Giant Branch Stars. , 24(3):103–117.

Kaviraj, S., C. Laigle, T. Kimm, J. E. G. Devriendt, Y. Dubois, C. Pichon, A. Slyz, E. Chisari, and S. Peirani
2017. The Horizon-AGN simulation: evolution of galaxy properties over cosmic time. , 467(4):4739–4752.

Kay, S. T., P. A. Thomas, A. Jenkins, and F. R. Pearce
2004. Cosmological simulations of the intracluster medium. *Monthly Notices of the Royal Astronomical Society*, 355(4):1091–1104.

Kennicutt, Robert C., J.
1998. Star Formation in Galaxies Along the Hubble Sequence. , 36:189–232.

Kereš, D., N. Katz, D. H. Weinberg, and R. Davé
2005. How do galaxies get their gas? *Monthly Notices of the Royal Astronomical Society*, 363(1):2–28.

Kim, W.-T., A. A. El-Zant, and M. Kamionkowski
2005. Dynamical friction and cooling flows in galaxy clusters. *The Astrophysical Journal*, 632(1):157.

Klypin, A. A. and S. F. Shandarin
1983. Three-dimensional numerical model of the formation of large-scale structure in the Universe. , 204:891–907.

Knebe, A., S. R. Knollmann, S. I. Muldrew, F. R. Pearce, M. A. Aragon-Calvo, Y. Ascasibar, P. S. Behroozi, D. Ceverino, S. Colombi, J. Diemand, K. Dolag, B. L. Falck, P. Fasel, J. Gardner, S. Gottlöber, C.-H. Hsu, F. Iannuzzi, A. Klypin, Z. Lukić, M. Maciejewski, C. McBride, M. C. Neyrinck, S. Planelles, D. Potter, V. Quilis, Y. Rasera, J. I. Read, P. M. Ricker, F. Roy, V. Springel, J. Stadel, G. Stinson, P. M. Sutter, V. Turchaninov, D. Tweed, G. Yepes, and M. Zemp
2011. Haloes gone MAD: The Halo-Finder Comparison Project. , 415(3):2293–2318.

Knebe, A., F. R. Pearce, H. Lux, Y. Ascasibar, P. Behroozi, J. Casado, C. C. Moran, J. Diemand, K. Dolag, R. Dominguez-Tenreiro, P. Elahi, B. Falck, S. Gottlöber, J. Han, A. Klypin, Z. Lukić, M. Maciejewski, C. K. McBride, M. E. Merchán, S. I. Muldrew, M. Neyrinck, J. Onions, S. Planelles, D. Potter, V. Quilis, Y. Rasera, P. M. Ricker, F. Roy, A. N. Ruiz, M. A. Sgró, V. Springel, J. Stadel, P. M. Sutter, D. Tweed, and M. Zemp
2013. Structure finding in cosmological simulations: the state of affairs. , 435(2):1618–1658.

Komatsu, E., K. M. Smith, J. Dunkley, C. L. Bennett, B. Gold, G. Hinshaw, N. Jarosik, D. Larson, M. R. Nolta, L. Page, D. N. Spergel, M. Halpern, R. S. Hill, A. Kogut, M. Limon, S. S. Meyer, N. Odegard, G. S. Tucker, J. L. Weiland, E. Wollack, and E. L.

Wright
2011. Seven-year Wilkinson Microwave Anisotropy Probe (WMAP) Observations: Cosmological Interpretation. , 192(2):18.

Kravtsov, A. V., A. A. Berlind, R. H. Wechsler, A. A. Klypin, S. Gottloeber, B. Allgood, and J. R. Primack
2004. The dark side of the halo occupation distribution. *The Astrophysical Journal*, 609(1):35.

Kravtsov, A. V. and S. Borgani
2012. Formation of galaxy clusters. *Annual Review of Astronomy and Astrophysics*, 50:353–409.

Kravtsov, A. V., A. A. Vikhlinin, and A. V. Meshcheryakov
2018. Stellar Mass—Halo Mass Relation and Star Formation Efficiency in High-Mass Halos. *Astronomy Letters*, 44(1):8–34.

Kurk, J., L. Pentericci, H. Röttgering, and G. Miley
2004. A search for clusters at high redshift-iii. candidate hα emitters and eros in the pks 1138–262 proto-cluster at z= 2.16. *Astronomy & Astrophysics*, 428(3):793–815.

Kurk, J., H. Röttgering, L. Pentericci, G. Miley, W. van Breugel, C. Carilli, H. Ford, T. Heckman, P. McCarthy, and A. Moorwood
2000. A search for clusters at high redshift. i. candidate lyalpha emitters near 1138-262 at z= 2.2. *Astronomy and Astrophysics*, 358:L1–L4.

Lacey, C.
2001. Semi-analytical models of galaxy formation. 222:273.

Lacey, C. and S. Cole
1994. Merger Rates in Hierarchical Models of Galaxy Formation - Part Two - Comparison with N-Body Simulations. , 271:676.

Laganá, T. F., Y.-Y. Zhang, T. H. Reiprich, and P. Schneider
2011. XMM-Newton/Sloan Digital Sky Survey: Star Formation Efficiency in Galaxy Clusters and Constraints on the Matter-density Parameter. , 743(1):13.

Lahav, O., P. B. Lilje, J. R. Primack, and M. J. Rees
1991. Dynamical effects of the cosmological constant. *Monthly Notices of the Royal Astronomical Society*, 251(1):128–136.

Le Brun, A. M. C., I. G. McCarthy, and J.-B. Melin
2015. Testing Sunyaev-Zel'dovich measurements of the hot gas content of dark matter haloes using synthetic skies. , 451(4):3868–3881.

Limousin, M., J. Richard, E. Jullo, J.-P. Kneib, B. Fort, G. Soucail, Á. Elíasdóttir, P. Natarajan, R. S. Ellis, I. Smail, O. Czoske, G. P. Smith, P. Hudelot, S. Bardeau, H. Ebeling, E. Egami, and K. K. Knudsen
2007. Combining Strong and Weak Gravitational Lensing in Abell 1689. , 668(2):643–666.

Lin, Y.-T., M. Brodwin, A. H. Gonzalez, P. Bode, P. R. Eisenhardt, S. Stanford, and A. Vikhlinin
2013. The stellar mass growth of brightest cluster galaxies in the irac shallow cluster survey. *The Astrophysical Journal*, 771(1):61.

Lin, Y.-T., B.-C. Hsieh, S.-C. Lin, M. Oguri, K.-F. Chen, M. Tanaka, I.-N. Chiu, S. Huang, T. Kodama, A. Leauthaud, S. More, A. J. Nishizawa, K. Bundy, L. Lin, and S. Miyazaki
2017. First results on the cluster galaxy population from the subaru hyper suprime-cam survey. III. brightest cluster galaxies, stellar mass distribution, and active galaxies. 851(2):139.

Lin, Y.-T., J. J. Mohr, and S. A. Stanford
2003. Near-infrared properties of galaxy clusters: luminosity as a binding mass predictor and the state of cluster baryons. *The Astrophysical Journal*, 591(2):749.

Lin, Y.-T., S. A. Stanford, P. R. M. Eisenhardt, A. Vikhlinin, B. J. Maughan, and A. Kravtsov
2012. Baryon Content of Massive Galaxy Clusters at z = 0-0.6. , 745(1):L3.

Loken, C., M. L. Norman, E. Nelson, J. Burns, G. L. Bryan, and P. Motl
2002. A Universal Temperature Profile for Galaxy Clusters. , 579(2):571–576.

Lucy, L. B.
1977. A numerical approach to the testing of the fission hypothesis. , 82:1013–1024.

Mac Low, M.-M. and A. Ferrara
1999. Starburst-driven Mass Loss from Dwarf Galaxies: Efficiency and Metal Ejection. , 513(1):142–155.

Macciò, A. V., B. Moore, and J. Stadel
2005. The origin of polar ring galaxies: Evidence for galaxy formation by cold accretion. 636(1):L25–L28.

Madau, P. and M. Dickinson
2014. Cosmic Star-Formation History. , 52:415–486.

Madau, P., A. Ferrara, and M. J. Rees
2001. Early metal enrichment of the intergalactic medium by pregalactic outflows. 555(1):92–105.

Magorrian, J., S. Tremaine, D. Richstone, R. Bender, G. Bower, A. Dressler, S. M. Faber, K. Gebhardt, R. Green, C. Grillmair, J. Kormendy, and T. Lauer
1998. The Demography of Massive Dark Objects in Galaxy Centers. , 115(6):2285–2305.

Marinacci, F., M. Vogelsberger, R. Pakmor, P. Torrey, V. Springel, L. Hernquist, D. Nelson, R. Weinberger, A. Pillepich, J. Naiman, and S. Genel
2018. First results from the IllustrisTNG simulations: radio haloes and magnetic fields. , 480(4):5113–5139.

Markevitch, M., W. R. Forman, C. L. Sarazin, and A. Vikhlinin
1998. The Temperature Structure of 30 Nearby Clusters Observed with ASCA: Similarity of Temperature Profiles. , 503(1):77–96.

Martin, C. L.
1999. Properties of galactic outflows: measurements of the feedback from star formation. *The Astrophysical Journal*, 513(1):156.

Martizzi, D., R. Teyssier, and B. Moore
2012. The formation of the brightest cluster galaxies in cosmological simulations: the case for active galactic nucleus feedback. *Monthly Notices of the Royal Astronomical Society*, 420(4):2859–2873.

Mawatari, K., T. Yamada, Y. Nakamura, T. Hayashino, and Y. Matsuda
2012. Characterization of the distribution of the lyα emitters in the 53w002 field at z= 2.4. *The Astrophysical Journal*, 759(2):133.

McCarthy, I. G., R. G. Bower, M. L. Balogh, G. M. Voit, F. R. Pearce, T. Theuns, A. Babul, C. G. Lacey, and C. S. Frenk
2007. Modelling shock heating in cluster mergers–i. moving beyond the spherical accretion model. *Monthly Notices of the Royal Astronomical Society*, 376(2):497–522.

McCarthy, I. G., J. Schaye, T. J. Ponman, R. G. Bower, C. M. Booth, C. D. Vecchia, R. A. Crain, V. Springel, T. Theuns, and R. P. Wiersma
2010. The case for agn feedback in galaxy groups. *Monthly Notices of the Royal Astronomical Society*, 406(2):822–839.

McConnell, N. J. and C.-P. Ma
2013. Revisiting the Scaling Relations of Black Hole Masses and Host Galaxy Properties. , 764(2):184.

McDonald, M., B. A. Benson, A. Vikhlinin, K. A. Aird, S. W. Allen, M. Bautz, M. Bayliss, L. E. Bleem, S. Bocquet, M. Brodwin, J. E. Carlstrom, C. L. Chang, H. M. Cho, A. Clocchiatti, T. M. Crawford, A. T. Crites, T. de Haan, M. A. Dobbs, R. J. Foley, W. R. Forman, E. M. George, M. D. Gladders, A. H. Gonzalez, N. W. Halverson, J. Hlavacek-Larrondo, G. P. Holder, W. L. Holzapfel, J. D. Hrubes, C. Jones, R. Keisler, L. Knox, A. T. Lee, E. M. Leitch, J. Liu, M. Lueker, D. Luong-Van, A. Mantz, D. P. Marrone,

J. J. McMahon, S. S. Meyer, E. D. Miller, L. Mocanu, J. J. Mohr, S. S. Murray, S. Padin, C. Pryke, C. L. Reichardt, A. Rest, J. E. Ruhl, B. R. Saliwanchik, A. Saro, J. T. Sayre, K. K. Schaffer, E. Shirokoff, H. G. Spieler, B. Stalder, S. A. Stanford, Z. Staniszewski, A. A. Stark, K. T. Story, C. W. Stubbs, K. Vanderlinde, J. D. Vieira, R. Williamson, O. Zahn, and A. Zenteno
2014. The Redshift Evolution of the Mean Temperature, Pressure, and Entropy Profiles in 80 SPT-Selected Galaxy Clusters. , 794(1):67.

McDonald, M., M. Gaspari, B. R. McNamara, and G. R. Tremblay
2018. Revisiting the Cooling Flow Problem in Galaxies, Groups, and Clusters of Galaxies. , 858(1):45.

McDonald, P., U. Seljak, R. Cen, D. Shih, D. H. Weinberg, S. Burles, D. P. Schneider, D. J. Schlegel, N. A. Bahcall, J. W. Briggs, J. Brinkmann, M. Fukugita, Ž. Ivezić, S. Kent, and D. E. V. Berk
2005. The linear theory power spectrum from the ly forest in the sloan digital sky survey. 635(2):761–783.

McNamara, B. and P. Nulsen
2007. Heating hot atmospheres with active galactic nuclei. *Annu. Rev. Astron. Astrophys.*, 45:117–175.

Meekins, J. F., G. Fritz, T. A. Chubb, H. Friedman, and R. C. Henry
1971. Physical sciences: X-rays from the coma cluster of galaxies. *Nature*, 231(5298):107–108.

Miley, G. and C. De Breuck
2008. Distant radio galaxies and their environments. *The Astronomy and Astrophysics Review*, 15(2):67–144.

Miller, T. B., S. C. Chapman, M. Aravena, M. L. N. Ashby, C. C. Hayward, J. D. Vieira, A. Weiß, A. Babul, M. Béthermin, C. M. Bradford, M. Brodwin, J. E. Carlstrom, C.-C. Chen, D. J. M. Cunningham, C. De Breuck, A. H. Gonzalez, T. R. Greve, J. Harnett, Y. Hezaveh, K. Lacaille, K. C. Litke, J. Ma, M. Malkan, D. P. Marrone, W. Morningstar, E. J. Murphy, D. Narayanan, E. Pass, R. Perry, K. A. Phadke, D. Rennehan, K. M. Rotermund, J. Simpson, J. S. Spilker, J. Sreevani, A. A. Stark, M. L. Strandet, and A. L. Strom
2018. A massive core for a cluster of galaxies at a redshift of 4.3. , 556(7702):469–472.

Miniati, F., D. Ryu, H. Kang, T. Jones, R. Cen, and J. P. Ostriker
2000. Properties of cosmic shock waves in large-scale structure formation. *The Astrophysical Journal*, 542(2):608.

Mohr, J. J., B. Mathiesen, and A. E. Evrard
1999. Properties of the Intracluster Medium in an Ensemble of Nearby Galaxy Clusters. , 517(2):627–649.

Monaghan, J. J.
1992. Smoothed particle hydrodynamics. , 30:543–574.

Moore, B., T. Quinn, F. Governato, J. Stadel, and G. Lake
1999. Cold collapse and the core catastrophe. *Monthly Notices of the Royal Astronomical Society*, 310(4):1147–1152.

More, S., A. V. Kravtsov, N. Dalal, and S. Gottlöber
2011. The Overdensity and Masses of the Friends-of-friends Halos and Universality of Halo Mass Function. , 195(1):4.

Muanwong, O., P. Thomas, S. Kay, F. Pearce, and H. Couchman
2001. The effect of radiative cooling on scaling laws of x-ray groups and clusters. *The Astrophysical Journal Letters*, 552(1):L27.

Muldrew, S. I., N. A. Hatch, and E. A. Cooke
2015. What are protoclusters?–defining high-redshift galaxy clusters and protoclusters. *Monthly Notices of the Royal Astronomical Society*, 452(3):2528–2539.

Murali, C., N. Katz, L. Hernquist, D. H. Weinberg, and R. Dave
2002. The growth of galaxies in cosmological simulations of structure formation. 571(1):1–14.

Muzzin, A., G. Wilson, R. Demarco, C. Lidman, J. Nantais, H. Hoekstra, H. Yee, and A. Rettura
2013. Discovery of a rich cluster at z= 1.63 using the rest-frame 1.6 μm "stellar bump sequence" method. *The Astrophysical Journal*, 767(1):39.

Nagai, D. and A. V. Kravtsov
2005. The Radial Distribution of Galaxies in Λ Cold Dark Matter Clusters. , 618(2):557–568.

Nagai, D., A. V. Kravtsov, and A. Kosowsky
2003. Effect of internal flows on sunyaev-zeldovich measurements of cluster peculiar velocities. *The Astrophysical Journal*, 587(2):524.

Nagai, D., A. Vikhlinin, and A. V. Kravtsov
2007. Testing x-ray measurements of galaxy clusters with cosmological simulations. *The Astrophysical Journal*, 655(1):98.

Naiman, J. P., A. Pillepich, V. Springel, E. Ramirez-Ruiz, P. Torrey, M. Vogelsberger, R. Pakmor, D. Nelson, F. Marinacci, L. Hernquist, R. Weinberger, and S. Genel
2018. First results from the IllustrisTNG simulations: a tale of two elements - chemical evolution of magnesium and europium. , 477(1):1206–1224.

Natarajan, P., J.-P. Kneib, I. Smail, T. Treu, R. Ellis, S. Moran, M. Limousin, and O. Czoske
2009. The Survival of Dark Matter Halos in the Cluster Cl 0024+16. , 693(1):970–983.

Navarro, J. F., C. S. Frenk, and S. D. White
1997. A universal density profile from hierarchical clustering. *The Astrophysical Journal*, 490(2):493.

Navarro, J. F., E. Hayashi, C. Power, A. R. Jenkins, C. S. Frenk, S. D. M. White, V. Springel, J. Stadel, and T. R. Quinn
2004. The inner structure of ΛCDM haloes - III. Universality and asymptotic slopes. , 349(3):1039–1051.

Nelson, D., A. Pillepich, V. Springel, R. Pakmor, R. Weinberger, S. Genel, P. Torrey, M. Vogelsberger, F. Marinacci, and L. Hernquist
2019a. First results from the TNG50 simulation: galactic outflows driven by supernovae and black hole feedback. , 490(3):3234–3261.

Nelson, D., V. Springel, A. Pillepich, V. Rodriguez-Gomez, P. Torrey, S. Genel, M. Vogelsberger, R. Pakmor, F. Marinacci, R. Weinberger, L. Kelley, M. Lovell, B. Diemer, and L. Hernquist
2019b. The IllustrisTNG simulations: public data release. *Computational Astrophysics and Cosmology*, 6(1):2.

Niemiec, A., E. Jullo, M. Limousin, C. Giocoli, T. Erben, H. Hildebrant, J.-P. Kneib, A. Leauthaud, M. Makler, B. Moraes, M. E. S. Pereira, H. Shan, E. Rozo, E. Rykoff, and L. Van Waerbeke
2017. Stellar-to-halo mass relation of cluster galaxies. , 471(1):1153–1166.

Nomoto, K., C. Kobayashi, and N. Tominaga
2013. Nucleosynthesis in Stars and the Chemical Enrichment of Galaxies. , 51(1):457–509.

Norman, G.
2010. Likert scales, levels of measurement and the "laws" of statistics. *Advances in health sciences education*, 15(5):625–632.

Onions, J., Y. Ascasibar, P. Behroozi, J. Casado, P. Elahi, J. Han, A. Knebe, H. Lux, M. E. Merchán, S. I. Muldrew, M. Neyrinck, L. Old, F. R. Pearce, D. Potter, A. N. Ruiz, M. A. Sgró, D. Tweed, and T. Yue
2013. Subhaloes gone Notts: spin across subhaloes and finders. *Monthly Notices of the Royal Astronomical Society*, 429(3):2739–2747.

Oteo, I., R. Ivison, L. Dunne, A. Manilla-Robles, S. Maddox, A. Lewis, G. De Zotti, M. Bremer, D. Clements, A. Cooray, et al.
2018. An extreme protocluster of luminous dusty starbursts in the early universe. *The Astrophysical Journal*, 856(1):72.

Overzier, R. A.
2016. The realm of the galaxy protoclusters. A review. , 24(1):14.

Overzier, R. A., T. M. Heckman, C. Tremonti, L. Armus, A. Basu-Zych, T. Gonçalves, R. M. Rich, D. C. Martin, A. Ptak, D. Schiminovich, et al.
2009. Local lyman break galaxy analogs: The impact of massive star-forming clumps on the interstellar medium and the global structure of young, forming galaxies. *The Astrophysical Journal*, 706(1):203.

Padovani, P. and F. Matteucci
1993. Stellar Mass Loss in Elliptical Galaxies and the Fueling of Active Galactic Nuclei. , 416:26.

Pearce, F., P. Thomas, H. Couchman, and A. Edge
2000. The effect of radiative cooling on the x-ray properties of galaxy clusters. *Monthly Notices of the Royal Astronomical Society*, 317(4):1029–1040.

Pettini, M., A. E. Shapley, C. C. Steidel, J.-G. Cuby, M. Dickinson, A. F. Moorwood, K. L. Adelberger, and M. Giavalisco
2001. The rest-frame optical spectra of lyman break galaxies: star formation, extinction, abundances, and kinematics. *The astrophysical journal*, 554(2):981.

Piffaretti, R., P. Jetzer, J. S. Kaastra, and T. Tamura
2005. Temperature and entropy profiles of nearby cooling flow clusters observed with XMM-Newton. , 433(1):101–111.

Pillepich, A., V. Springel, D. Nelson, S. Genel, J. Naiman, R. Pakmor, L. Hernquist, P. Torrey, M. Vogelsberger, R. Weinberger, and F. Marinacci
2018. Simulating galaxy formation with the IllustrisTNG model. , 473(3):4077–4106.

Pizzuti, L., B. Sartoris, S. Borgani, and A. Biviano
2020. Calibration of systematics in constraining modified gravity models with galaxy cluster mass profiles. , 2020(4):024.

Planck Collaboration, P. A. R. Ade, N. Aghanim, C. Armitage-Caplan, M. Arnaud, M. Ashdown, F. Atrio-Barandela, J. Aumont, C. Baccigalupi, A. J. Banday, R. B. Barreiro, J. G. Bartlett, E. Battaner, K. Benabed, A. Benoît, A. Benoit-Lévy, J. P. Bernard, M. Bersanelli, P. Bielewicz, J. Bobin, J. J. Bock, A. Bonaldi, J. R. Bond, J. Borrill, F. R. Bouchet, M. Bridges, M. Bucher, C. Burigana, R. C. Butler, E. Calabrese, B. Cappellini, J. F. Cardoso, A. Catalano, A. Challinor, A. Chamballu, R. R. Chary, X. Chen, H. C. Chiang, L. Y. Chiang, P. R. Christensen, S. Church, D. L. Clements, S. Colombi, L. P. L. Colombo, F. Couchot, A. Coulais, B. P. Crill, A. Curto, F. Cuttaia, L. Danese, R. D. Davies, R. J. Davis, P. de Bernardis, A. de Rosa, G. de Zotti, J. Delabrouille, J. M. Delouis, F. X. Désert, C. Dickinson, J. M. Diego, K. Dolag, H. Dole, S. Donzelli, O. Doré, M. Douspis, J. Dunkley, X. Dupac, G. Efstathiou, F. Elsner, T. A.

Enßlin, H. K. Eriksen, F. Finelli, O. Forni, M. Frailis, A. A. Fraisse, E. Franceschi, T. C. Gaier, S. Galeotta, S. Galli, K. Ganga, M. Giard, G. Giardino, Y. Giraud-Héraud, E. Gjerløw, J. González-Nuevo, K. M. Górski, S. Gratton, A. Gregorio, A. Gruppuso, J. E. Gudmundsson, J. Haissinski, J. Hamann, F. K. Hansen, D. Hanson, D. Harrison, S. Henrot-Versillé, C. Hernández-Monteagudo, D. Herranz, S. R. Hildebrandt, E. Hivon, M. Hobson, W. A. Holmes, A. Hornstrup, Z. Hou, W. Hovest, K. M. Huffenberger, A. H. Jaffe, T. R. Jaffe, J. Jewell, W. C. Jones, M. Juvela, E. Keihänen, R. Keskitalo, T. S. Kisner, R. Kneissl, J. Knoche, L. Knox, M. Kunz, H. Kurki-Suonio, G. Lagache, A. Lähteenmäki, J. M. Lamarre, A. Lasenby, M. Lattanzi, R. J. Laureijs, C. R. Lawrence, S. Leach, J. P. Leahy, R. Leonardi, J. León-Tavares, J. Lesgourgues, A. Lewis, M. Liguori, P. B. Lilje, M. Linden-Vørnle, M. López-Caniego, P. M. Lubin, J. F. Macías-Pérez, B. Maffei, D. Maino, N. Mandolesi, M. Maris, D. J. Marshall, P. G. Martin, E. Martínez-González, S. Masi, M. Massardi, S. Matarrese, F. Matthai, P. Mazzotta, P. R. Meinhold, A. Melchiorri, J. B. Melin, L. Mendes, E. Menegoni, A. Mennella, M. Migliaccio, M. Millea, S. Mitra, M. A. Miville-Deschênes, A. Moneti, L. Montier, G. Morgante, D. Mortlock, A. Moss, D. Munshi, J. A. Murphy, P. Naselsky, F. Nati, P. Natoli, C. B. Netterfield, H. U. Nørgaard-Nielsen, F. Noviello, D. Novikov, I. Novikov, I. J. O'Dwyer, S. Osborne, C. A. Oxborrow, F. Paci, L. Pagano, F. Pajot, R. Paladini, D. Paoletti, B. Partridge, F. Pasian, G. Patanchon, D. Pearson, T. J. Pearson, H. V. Peiris, O. Perdereau, L. Perotto, F. Perrotta, V. Pettorino, F. Piacentini, M. Piat, E. Pierpaoli, D. Pietrobon, S. Plaszczynski, P. Platania, E. Pointecouteau, G. Polenta, N. Ponthieu, L. Popa, T. Poutanen, G. W. Pratt, G. Prézeau, S. Prunet, J. L. Puget, J. P. Rachen, W. T. Reach, R. Rebolo, M. Reinecke, M. Remazeilles, C. Renault, S. Ricciardi, T. Riller, I. Ristorcelli, G. Rocha, C. Rosset, G. Roudier, M. Rowan-Robinson, J. A. Rubiño-Martín, B. Rusholme, M. Sandri, D. Santos, M. Savelainen, G. Savini, D. Scott, M. D. Seiffert, E. P. S. Shellard, L. D. Spencer, J. L. Starck, V. Stolyarov, R. Stompor, R. Sudiwala, R. Sunyaev, F. Sureau, D. Sutton, A. S. Suur-Uski, J. F. Sygnet, J. A. Tauber, D. Tavagnacco, L. Terenzi, L. Toffolatti, M. Tomasi, M. Tristram, M. Tucci, J. Tuovinen, M. Türler, G. Umana, L. Valenziano, J. Valiviita, B. Van Tent, P. Vielva, F. Villa, N. Vittorio, L. A. Wade, B. D. Wandelt, I. K. Wehus, M. White, S. D. M. White, A. Wilkinson, D. Yvon, A. Zacchei, and A. Zonca
2014. Planck 2013 results. XVI. Cosmological parameters. , 571:A16.

Planelles, S., S. Borgani, K. Dolag, S. Ettori, D. Fabjan, G. Murante, and L. Tornatore
2013. Baryon census in hydrodynamical simulations of galaxy clusters. *Monthly Notices of the Royal Astronomical Society*, 431(2):1487–1502.

Planelles, S., S. Borgani, D. Fabjan, M. Killedar, G. Murante, G. Granato, C. Ragone-Figueroa, and K. Dolag
2014. On the role of agn feedback on the thermal and chemodynamical properties of the hot intracluster medium. *Monthly Notices of the Royal Astronomical Society*, 438(1):195–216.

Planelles, S., D. Fabjan, S. Borgani, G. Murante, E. Rasia, V. Biffi, N. Truong, C. Ragone-

Figueroa, G. L. Granato, K. Dolag, E. Pierpaoli, A. M. Beck, L. K. Steinborn, and M. Gaspari
2017. Pressure of the hot gas in simulations of galaxy clusters. *Monthly Notices of the Royal Astronomical Society*, 467(4):3827–3847.

Pogosyan, D. Y., J. R. Bond, L. Kofman, J. Wadsley, S. Colombi, and Y. Mellier
1998. Cosmic web: Origin and observables. In *Wide Field Surveys in Cosmology (14th IAP meeting)*, Pp. 61–67. Editions Frontieres.

Prada, F., A. A. Klypin, E. Simonneau, J. Betancort-Rijo, S. Patiri, S. Gottlöber, and M. A. Sanchez-Conde
2006. How far do they go? the outer structure of galactic dark matter halos. *The Astrophysical Journal*, 645(2):1001.

Pratt, G. W., M. Arnaud, R. Piffaretti, H. Böhringer, T. J. Ponman, J. H. Croston, G. M. Voit, S. Borgani, and R. G. Bower
2010. Gas entropy in a representative sample of nearby X-ray galaxy clusters (REXCESS): relationship to gas mass fraction. , 511:A85.

Pratt, G. W., H. Böhringer, J. H. Croston, M. Arnaud, S. Borgani, A. Finoguenov, and R. F. Temple
2007. Temperature profiles of a representative sample of nearby X-ray galaxy clusters. , 461(1):71–80.

Press, W. H. and P. Schechter
1974. Formation of Galaxies and Clusters of Galaxies by Self-Similar Gravitational Condensation. , 187:425–438.

Price, D.
2005. *Smoothed Particle Hydrodynamics*. PhD thesis, -.

Puchwein, E., D. Sijacki, and V. Springel
2008. Simulations of agn feedback in galaxy clusters and groups: impact on gas fractions and the lx-t scaling relation. *The Astrophysical Journal Letters*, 687(2):L53.

Puchwein, E., V. Springel, D. Sijacki, and K. Dolag
2010. Intracluster stars in simulations with active galactic nucleus feedback. *Monthly Notices of the Royal Astronomical Society*, 406(2):936–951.

Quilis, V.
2004. Masclet: a new multidimensional amr cosmological code. *Proceedings of the International Astronomical Union*, 2004(IAUC195):293–295.

Quilis, V., M. José, D. Sáez, et al.
1998. On the role of shock waves in galaxy cluster evolution. *The Astrophysical Journal*, 502(2):518.

Ragagnin, A., K. Dolag, L. Moscardini, A. Biviano, and M. D'Onofrio
2019. Dependency of halo concentration on mass, redshift and fossilness in Magneticum hydrodynamic simulations. , 486(3):4001–4012.

Ragagnin, A., A. Fumagalli, T. Castro, K. Dolag, A. Saro, M. Costanzi, and S. Bocquet
2021. Satellite galaxy abundance dependency on cosmology in Magneticum simulations. *arXiv e-prints*, P. arXiv:2110.05498.

Ragone-Figueroa, C., G. L. Granato, M. E. Ferraro, G. Murante, V. Biffi, S. Borgani, S. Planelles, and E. Rasia
2018. BCG mass evolution in cosmological hydro-simulations. *Monthly Notices of the Royal Astronomical Society*, 479(1):1125–1136.

Ragone-Figueroa, C., G. L. Granato, G. Murante, S. Borgani, and W. Cui
2013. Brightest cluster galaxies in cosmological simulations: achievements and limitations of active galactic nuclei feedback models. *Monthly Notices of the Royal Astronomical Society*, 436(2):1750–1764.

Rasia, E., S. Borgani, G. Murante, S. Planelles, A. M. Beck, V. Biffi, C. Ragone-Figueroa, G. L. Granato, L. K. Steinborn, and K. Dolag
2015. Cool Core Clusters from Cosmological Simulations. , 813(1):L17.

Remus, R.-S., K. Dolag, T. Naab, A. Burkert, M. Hirschmann, T. L. Hoffmann, and P. H. Johansson
2017. The co-evolution of total density profiles and central dark matter fractions in simulated early-type galaxies. , 464(3):3742–3756.

Rhee, J., R. Smith, H. Choi, S. K. Yi, Y. Jaffé, G. Candlish, and R. Sánchez-Jánssen
2017. Phase-space Analysis in the Group and Cluster Environment: Time Since Infall and Tidal Mass Loss. , 843(2):128.

Ricker, P. M. and C. L. Sarazin
2001. Off-axis cluster mergers: effects of a strongly peaked dark matter profile. *The Astrophysical Journal*, 561(2):621.

Robertson, A., R. Massey, and V. Eke
2016. What does the bullet cluster tell us about self-interacting dark matter? *Monthly Notices of the Royal Astronomical Society*, P. stw2670.

Rodríguez-Puebla, A., J. R. Primack, V. Avila-Reese, and S. M. Faber
2017. Constraining the galaxy–halo connection over the last 13.3 Gyr: star formation histories, galaxy mergers and structural properties. *Monthly Notices of the Royal Astronomical Society*, 470(1):651–687.

Roncarelli, M., S. Ettori, K. Dolag, L. Moscardini, S. Borgani, and G. Murante
2006. Simulated X-ray galaxy clusters at the virial radius: Slopes of the gas density,

temperature and surface brightness profiles. *Monthly Notices of the Royal Astronomical Society*, 373(4):1339–1350.

Rosner, R. and W. Tucker
1989. On magnetic fields, heating and thermal conduction in halos, and the suppression of cooling flows. *The Astrophysical Journal*, 338:761–769.

Rozo, E., A. E. Evrard, E. S. Rykoff, and J. G. Bartlett
2013. A comparative study of local galaxy clusters – II. X-ray and SZ scaling relations. *Monthly Notices of the Royal Astronomical Society*, 438(1):62–77.

Sanderson, A. J., T. J. Ponman, and E. O'Sullivan
2006. A statistically selected chandra sample of 20 galaxy clusters–i. temperature and cooling time profiles. *Monthly Notices of the Royal Astronomical Society*, 372(4):1496–1508.

Sarazin, C. L.
1988. Book-Review - X-Ray Emissions from Clusters of Galaxies. , 76:639.

Saro, A., S. Borgani, L. Tornatore, G. De Lucia, K. Dolag, and G. Murante
2008. Simulating the formation of a protocluster at z 2. *Monthly Notices of the Royal Astronomical Society*, 392(2):795–800.

Scannapieco, C., M. Wadepuhl, O. H. Parry, J. F. Navarro, A. Jenkins, V. Springel, R. Teyssier, E. Carlson, H. M. P. Couchman, R. A. Crain, C. Dalla Vecchia, C. S. Frenk, C. Kobayashi, P. Monaco, G. Murante, T. Okamoto, T. Quinn, J. Schaye, G. S. Stinson, T. Theuns, J. Wadsley, S. D. M. White, and R. Woods
2012. The Aquila comparison project: the effects of feedback and numerical methods on simulations of galaxy formation. , 423(2):1726–1749.

Scannapieco, E. and T. Broadhurst
2001. Linking the metallicity distribution of galactic halo stars to the enrichment history of the universe. *The Astrophysical Journal Letters*, 550(1):L39.

Scannapieco, E., R. J. Thacker, and M. Davis
2001. High-redshift galaxy outflows and the formation of dwarf galaxies. 557(2):605–615.

Schaye, J., R. A. Crain, R. G. Bower, M. Furlong, M. Schaller, T. Theuns, C. Dalla Vecchia, C. S. Frenk, I. G. McCarthy, J. C. Helly, A. Jenkins, Y. M. Rosas-Guevara, S. D. M. White, M. Baes, C. M. Booth, P. Camps, J. F. Navarro, Y. Qu, A. Rahmati, T. Sawala, P. A. Thomas, and J. Trayford
2015. The EAGLE project: simulating the evolution and assembly of galaxies and their environments. , 446(1):521–554.

Schreiber, C., M. Pannella, D. Elbaz, M. Béthermin, H. Inami, M. Dickinson, B. Magnelli, T. Wang, H. Aussel, E. Daddi, S. Juneau, X. Shu, M. T. Sargent, V. Buat, S. M.

Faber, H. C. Ferguson, M. Giavalisco, A. M. Koekemoer, G. Magdis, G. E. Morrison, C. Papovich, P. Santini, and D. Scott
2015. The Herschel view of the dominant mode of galaxy growth from z = 4 to the present day. , 575:A74.

Schulze, F., R.-S. Remus, K. Dolag, A. Burkert, E. Emsellem, and G. van de Ven
2018. Kinematics of simulated galaxies - I. Connecting dynamical and morphological properties of early-type galaxies at different redshifts. , 480(4):4636–4658.

Sifón, C., M. Cacciato, H. Hoekstra, M. Brouwer, E. van Uitert, M. Viola, I. Baldry, S. Brough, M. J. I. Brown, A. Choi, S. P. Driver, T. Erben, A. Grado, C. Heymans, H. Hildebrandt, B. Joachimi, J. T. A. de Jong, K. Kuijken, J. McFarland, L. Miller, R. Nakajima, N. Napolitano, P. Norberg, A. S. G. Robotham, P. Schneider, and G. Verdoes Kleijn
2015. The masses of satellites in GAMA galaxy groups from 100 square degrees of KiDS weak lensing data. , 454(4):3938–3951.

Sifón, C., R. Herbonnet, H. Hoekstra, R. F. J. van der Burg, and M. Viola
2018. The galaxy–subhalo connection in low-redshift galaxy clusters from weak gravitational lensing. *Monthly Notices of the Royal Astronomical Society*, 478(1):1244–1264.

Sijacki, D., C. Pfrommer, V. Springel, and T. A. Enßlin
2008. Simulations of cosmic-ray feedback by active galactic nuclei in galaxy clusters. *Monthly Notices of the Royal Astronomical Society*, 387(4):1403–1415.

Sijacki, D., V. Springel, T. Di Matteo, and L. Hernquist
2007. A unified model for agn feedback in cosmological simulations of structure formation. *Monthly Notices of the Royal Astronomical Society*, 380(3):877–900.

Sijacki, D., M. Vogelsberger, S. Genel, V. Springel, P. Torrey, G. F. Snyder, D. Nelson, and L. Hernquist
2015. The Illustris simulation: the evolving population of black holes across cosmic time. , 452(1):575–596.

Silk, J. and G. A. Mamon
2012. The current status of galaxy formation. *Research in Astronomy and Astrophysics*, 12(8):917–946.

Singh, P., A. Saro, M. Costanzi, and K. Dolag
2020. Cosmology dependence of galaxy cluster scaling relations. , 494(3):3728–3740.

Smith, S.
1936. The mass of the virgo cluster. *The Astrophysical Journal*, 83:23.

Somerville, R., R. Gilmore, J. Primack, and A. Domínguez
2012. Galaxy properties from the ultraviolet to the far-infrared: cold dark matter models

confront observations. *Monthly Notices of the Royal Astronomical Society*, 423:1992–2015.

Somerville, R. S., P. F. Hopkins, T. J. Cox, B. E. Robertson, and L. Hernquist
2008. A semi-analytic model for the co-evolution of galaxies, black holes and active galactic nuclei. , 391(2):481–506.

Springel, V.
2005. The cosmological simulation code GADGET-2. , 364(4):1105–1134.

Springel, V.
2010. E pur si muove: Galilean-invariant cosmological hydrodynamical simulations on a moving mesh. , 401(2):791–851.

Springel, V., T. Di Matteo, and L. Hernquist
2005. Modelling feedback from stars and black holes in galaxy mergers. *Monthly Notices of the Royal Astronomical Society*, 361(3):776–794.

Springel, V. and L. Hernquist
2003. Cosmological smoothed particle hydrodynamics simulations: a hybrid multiphase model for star formation. , 339(2):289–311.

Springel, V., R. Pakmor, A. Pillepich, R. Weinberger, D. Nelson, L. Hernquist, M. Vogelsberger, S. Genel, P. Torrey, F. Marinacci, and J. Naiman
2018. First results from the IllustrisTNG simulations: matter and galaxy clustering. , 475(1):676–698.

Springel, V., S. D. White, G. Tormen, and G. Kauffmann
2001. Populating a cluster of galaxies–i. results at z= 0. *Monthly Notices of the Royal Astronomical Society*, 328(3):726–750.

Springel, V., S. D. M. White, A. Jenkins, C. S. Frenk, N. Yoshida, L. Gao, J. Navarro, R. Thacker, D. Croton, J. Helly, J. A. Peacock, S. Cole, P. Thomas, H. Couchman, A. Evrard, J. Colberg, and F. Pearce
2005a. Simulations of the formation, evolution and clustering of galaxies and quasars. , 435(7042):629–636.

Springel, V., S. D. M. White, A. Jenkins, C. S. Frenk, N. Yoshida, L. Gao, J. Navarro, R. Thacker, D. Croton, J. Helly, J. A. Peacock, S. Cole, P. Thomas, H. Couchman, A. Evrard, J. Colberg, and F. Pearce
2005b. Simulations of the formation, evolution and clustering of galaxies and quasars. , 435(7042):629–636.

Springel, V., S. D. M. White, G. Tormen, and G. Kauffmann
2001a. Populating a cluster of galaxies - I. Results at [formmu2]z=0. , 328(3):726–750.

Springel, V., N. Yoshida, and S. D. M. White
2001b. GADGET: a code for collisionless and gasdynamical cosmological simulations. , 6(2):79–117.

Stadel, J., D. Potter, B. Moore, J. Diemand, P. Madau, M. Zemp, M. Kuhlen, and V. Quilis
2009. Quantifying the heart of darkness with ghalo–a multibillion particle simulation of a galactic halo. *Monthly Notices of the Royal Astronomical Society: Letters*, 398(1):L21–L25.

Steidel, C. C., K. L. Adelberger, M. Dickinson, M. Giavalisco, M. Pettini, and M. Kellogg
1998. A large structure of galaxies at redshift z˜ 3 and its cosmological implications. *The Astrophysical Journal*, 492(2):428.

Steidel, C. C., K. L. Adelberger, A. E. Shapley, D. K. Erb, N. A. Reddy, and M. Pettini
2005. Spectroscopic identification of a protocluster at z= 2.300: Environmental dependence of galaxy properties at high redshift. *The Astrophysical Journal*, 626(1):44.

Steidel, C. C., K. L. Adelberger, A. E. Shapley, M. Pettini, M. Dickinson, and M. Giavalisco
2000. Lyα imaging of a proto-cluster region at¡ z¿= 3.09. *The Astrophysical Journal*, 532(1):170.

Steinborn, L. K., K. Dolag, J. M. Comerford, M. Hirschmann, R.-S. Remus, and A. F. Teklu
2016. Origin and properties of dual and offset active galactic nuclei in a cosmological simulation at $z = 2$. *Monthly Notices of the Royal Astronomical Society*, 458(1):1013–1028.

Steinhardt, C. L., J. S. Speagle, P. Capak, J. D. Silverman, M. Carollo, J. Dunlop, Y. Hashimoto, B.-C. Hsieh, O. Ilbert, O. Le Fevre, E. Le Floc'h, N. Lee, L. Lin, Y.-T. Lin, D. Masters, H. J. McCracken, T. Nagao, A. Petric, M. Salvato, D. Sanders, N. Scoville, K. Sheth, M. A. Strauss, and Y. Taniguchi
2014. Star Formation at 4 ¡ z ¡ 6 from the Spitzer Large Area Survey with Hyper-Suprime-Cam (SPLASH). , 791(2):L25.

Stone, J. M., D. Mihalas, and M. L. Norman
1992. ZEUS-2D: A Radiation Magnetohydrodynamics Code for Astrophysical Flows in Two Space Dimensions. III. The Radiation Hydrodynamic Algorithms and Tests. , 80:819.

Strazzullo, V., E. Daddi, R. Gobat, B. Garilli, M. Mignoli, F. Valentino, M. Onodera, A. Renzini, A. Cimatti, A. Finoguenov, et al.
2015. Passive galaxies as tracers of cluster environments at z˜ 2. *Astronomy & Astrophysics*, 576:L6.

Sunyaev, R. A. and Y. B. Zeldovich
1972. Formation of Clusters of Galaxies; Protocluster Fragmentation and Intergalactic Gas Heating. , 20:189.

Tegmark, M., J. Silk, M. J. Rees, A. Blanchard, T. Abel, and F. Palla
1997. How Small Were the First Cosmological Objects? , 474:1.

Teklu, A. F., R.-S. Remus, K. Dolag, A. M. Beck, A. Burkert, A. S. Schmidt, F. Schulze, and L. K. Steinborn
2015. Connecting Angular Momentum and Galactic Dynamics: The Complex Interplay between Spin, Mass, and Morphology. , 812(1):29.

Teyssier, R.
2002. Cosmological hydrodynamics with adaptive mesh refinement. A new high resolution code called RAMSES. , 385:337–364.

Thomas, D., C. Maraston, R. Bender, and C. M. De Oliveira
2005. The epochs of early-type galaxy formation as a function of environment. *The Astrophysical Journal*, 621(2):673.

Tinker, J., A. V. Kravtsov, A. Klypin, K. Abazajian, M. Warren, G. Yepes, S. Gottlöber, and D. E. Holz
2008. Toward a Halo Mass Function for Precision Cosmology: The Limits of Universality. , 688(2):709–728.

Tonry, J. L.
1987. Properties of cd galaxies. In *Symposium-International astronomical union*, volume 127, Pp. 89–98. Cambridge University Press.

Tormen, G., F. R. Bouchet, and S. D. M. White
1997. The structure and dynamical evolution of dark matter haloes. , 286(4):865–884.

Tornatore, L., S. Borgani, K. Dolag, and F. Matteucci
2007. Chemical enrichment of galaxy clusters from hydrodynamical simulations. , 382(3):1050–1072.

Torrey, P., G. F. Snyder, M. Vogelsberger, C. C. Hayward, S. Genel, D. Sijacki, V. Springel, L. Hernquist, D. Nelson, M. Kriek, A. Pillepich, L. V. Sales, and C. K. McBride
2015. Synthetic galaxy images and spectra from the Illustris simulation. , 447(3):2753–2771.

Torrey, P., M. Vogelsberger, S. Genel, D. Sijacki, V. Springel, and L. Hernquist
2014. A model for cosmological simulations of galaxy formation physics: multi-epoch validation. *Monthly Notices of the Royal Astronomical Society*, 438(3):1985–2004.

Toshikawa, J., N. Kashikawa, R. Overzier, M. A. Malkan, H. Furusawa, S. Ishikawa, M. Onoue, K. Ota, M. Tanaka, Y. Niino, et al.
2016. A systematic survey of protoclusters at z 3–6 in the cfhtls deep fields. *The Astrophysical Journal*, 826(2):114.

Truong, N., E. Rasia, P. Mazzotta, S. Planelles, V. Biffi, D. Fabjan, A. M. Beck, S. Borgani, K. Dolag, M. Gaspari, G. L. Granato, G. Murante, C. Ragone-Figueroa, and L. K. Steinborn
2018. Cosmological hydrodynamical simulations of galaxy clusters: X-ray scaling relations and their evolution. , 474(3):4089–4111.

Valdarnini, R.
2003. Iron abundances and heating of the intracluster medium in hydrodynamical simulations of galaxy clusters. , 339(4):1117–1134.

Vale, A. and J. P. Ostriker
2004. Linking halo mass to galaxy luminosity. , 353(1):189–200.

van de Sande, J., C. D. P. Lagos, C. Welker, J. Bland-Hawthorn, F. Schulze, R.-S. Remus, Y. Bahé, S. Brough, J. J. Bryant, L. Cortese, S. M. Croom, J. Devriendt, Y. Dubois, M. Goodwin, I. S. Konstantopoulos, J. S. Lawrence, A. M. Medling, C. Pichon, S. N. Richards, S. F. Sanchez, N. Scott, and S. M. Sweet
2018. The SAMI Galaxy Survey: comparing 3D spectroscopic observations with galaxies from cosmological hydrodynamical simulations. *Monthly Notices of the Royal Astronomical Society*, 484(1):869–891.

Viel, M., M. G. Haehnelt, and V. Springel
2004. Inferring the dark matter power spectrum from the Lyman α forest in high-resolution QSO absorption spectra. , 354(3):684–694.

Vikhlinin, A., M. Markevitch, S. S. Murray, C. Jones, W. Forman, and L. Van Speybroeck
2005. Chandra Temperature Profiles for a Sample of Nearby Relaxed Galaxy Clusters. , 628(2):655–672.

Vogelsberger, M., S. Genel, D. Sijacki, P. Torrey, V. Springel, and L. Hernquist
2013. A model for cosmological simulations of galaxy formation physics. , 436(4):3031–3067.

Vogelsberger, M., S. Genel, V. Springel, P. Torrey, D. Sijacki, D. Xu, G. Snyder, S. Bird, D. Nelson, and L. Hernquist
2014. Properties of galaxies reproduced by a hydrodynamic simulation. , 509(7499):177–182.

Voit, G. M.
2005. Tracing cosmic evolution with clusters of galaxies. *Reviews of Modern Physics*, 77(1):207.

Voit, G. M. and G. L. Bryan
2001. Regulation of the x-ray luminosity of clusters of galaxies by cooling and supernova feedback. *Nature*, 414(6862):425–427.

Von Der Linden, A., P. N. Best, G. Kauffmann, and S. D. White
2007. How special are brightest group and cluster galaxies? *Monthly Notices of the Royal Astronomical Society*, 379(3):867–893.

Wang, T., D. Elbaz, E. Daddi, D. Liu, T. Kodama, I. Tanaka, C. Schreiber, A. Zanella, F. Valentino, M. Sargent, K. Kohno, M. Xiao, M. Pannella, L. Ciesla, R. Gobat, and Y. Koyama
2018. Revealing the Environmental Dependence of Molecular Gas Content in a Distant X-Ray Cluster at z = 2.51. , 867(2):L29.

Weinberger, R., V. Springel, and R. Pakmor
2020. The AREPO Public Code Release. , 248(2):32.

Whitaker, K. E., M. Franx, J. Leja, P. G. van Dokkum, A. Henry, R. E. Skelton, M. Fumagalli, I. G. Momcheva, G. B. Brammer, I. Labbé, E. J. Nelson, and J. R. Rigby
2014. Constraining the Low-mass Slope of the Star Formation Sequence at 0.5 ¡ z ¡ 2.5. , 795(2):104.

White, S. D. M.
1994. Formation and Evolution of Galaxies: Les Houches Lectures. *arXiv e-prints*, Pp. astro–ph/9410043.

White, S. D. M. and M. J. Rees
1978. Core condensation in heavy halos: a two-stage theory for galaxy formation and clustering. , 183:341–358.

Wiersma, R. P. C., J. Schaye, and B. D. Smith
2009. The effect of photoionization on the cooling rates of enriched, astrophysical plasmas. , 393(1):99–107.

Wylezalek, D., A. Galametz, D. Stern, J. Vernet, C. De Breuck, N. Seymour, M. Brodwin, P. R. Eisenhardt, A. H. Gonzalez, N. Hatch, et al.
2013. Galaxy clusters around radio-loud active galactic nuclei at 1.3¡ z¡ 3.2 as seen by spitzer. *The Astrophysical Journal*, 769(1):79.

Xie, L., G. De Lucia, M. Hirschmann, F. Fontanot, and A. Zoldan
2017. H2-based star formation laws in hierarchical models of galaxy formation. *Monthly Notices of the Royal Astronomical Society*, 469(1):968–993.

Xie, L., Q. Guo, A. P. Cooper, C. S. Frenk, R. Li, and L. Gao
2015. The size evolution of elliptical galaxies. , 447(1):636–645.

Young, L. M., M. Bureau, T. A. Davis, F. Combes, R. M. McDermid, K. Alatalo, L. Blitz, M. Bois, F. Bournaud, M. Cappellari, R. L. Davies, P. T. de Zeeuw, E. Emsellem, S. Khochfar, D. Krajnović, H. Kuntschner, P.-Y. Lablanche, R. Morganti, T. Naab, T. Oosterloo, M. Sarzi, N. Scott, P. Serra, and A.-M. Weijmans
2011. The ATLAS3D project – IV. The molecular gas content of early-type galaxies*. *Monthly Notices of the Royal Astronomical Society*, 414(2):940–967.

Zakamska, N. L. and R. Narayan
2003. Models of galaxy clusters with thermal conduction. *The Astrophysical Journal*, 582(1):162.

Zhang, Y. Y., H. Andernach, C. A. Caretta, T. H. Reiprich, H. Böhringer, E. Puchwein, D. Sijacki, and M. Girardi
2011. HIFLUGCS: Galaxy cluster scaling relations between X-ray luminosity, gas mass, cluster radius, and velocity dispersion. , 526:A105.

Zhao, D., A. Aragón-Salamanca, and C. J. Conselice
2015. Evolution of the brightest cluster galaxies: the influence of morphology, stellar mass and environment. *Monthly Notices of the Royal Astronomical Society*, 453(4):4444–4455.

Zhu, Q., B. Smith, and L. Hernquist
2017. Gas cooling in hydrodynamic simulations with an exact time integration scheme. , 470(1):1017–1025.

Zirm, A. W., R. Overzier, G. Miley, J. Blakeslee, M. Clampin, C. De Breuck, R. Demarco, H. Ford, G. Hartig, N. Homeier, et al.
2005. Feedback and brightest cluster galaxy formation: Acs observations of the radio galaxy tn j1338–1942 at z= 4.1. *The Astrophysical Journal*, 630(1):68.

Zwicky, F.
1933. The redshift of extragalactic nebulae. *Helvetica Physica Acta*, 6:110–127.

Zwicky, F.
1937. On the masses of nebulae and of clusters of nebulae. *The Astrophysical Journal*, 86:217.

Zwicky, F.
1939. On the Formation of Clusters of Nebulae and the Cosmological Time Scale. *Proceedings of the National Academy of Science*, 25(12):604–609.

Appendix A

Derivation of Equation 2.2

We start by using the dirac-delta and the trivial identity:

$$f(\mathbf{r}) = \int_V f(\mathbf{r}')\delta(\mathbf{r} - \mathbf{r}')d\mathbf{r}', \tag{A.1}$$

where $f(\mathbf{r})$ is any scalar function defined on a three-dimensional co-ordinate system $\mathbf{r}$ ranging over a volume V and $\mathbf{r}$' is a dummy variable also ranging over V.

We can express the delta function $\delta(\mathbf{r})$ as the limit of a function, that we will call the kernel W, with a characteristic width that tends to 0:

$$\lim_{h\to 0} W(\mathbf{r}, h) = \delta(\mathbf{r}). \tag{A.2}$$

The function has closure volume, i.e is normalized as:

$$\int_V W(\mathbf{r}, h)d\mathbf{r}' = 1. \tag{A.3}$$

As any continuous function, $W(\mathbf{r} - \mathbf{r}', h)$ can be expanded as a Taylor series. In the case of symmetric kernels, i.e. $W(\mathbf{r} - \mathbf{r}', h) = W(\mathbf{r}' - \mathbf{r}, h)$, we can substitute $\delta(\mathbf{r})$ by its expression in terms of the Taylor expansion of the kernel function. Doing it so equation A.1 may be expressed with second order accuracy as:

$$f(\mathbf{r}) = \int_V f(\mathbf{r}')W(\mathbf{r} - \mathbf{r}', h)d\mathbf{r}' + \mathcal{O}(h^2). \tag{A.4}$$

The appearance of second order accuracy has to do with the vanishing of the kernel gradient at $\mathbf{r}' = \mathbf{r}$. More elaborated kernels with fourth order accuracy may also be constructed. However, the disadvantage is that these Kernels may become negative at some ranges, leading to unphysical results, like negative density evaluations (for further details see Benz, 1990; Monaghan, 1992; Price, 2005; Cossins, 2010).

Performing the trivial movement of multiplying and dividing by ρ_i inside the integral in equation A.4 (remember that we are considering a symmetric Kernel function) we get:

$$f(\mathbf{r}) = \int_V \frac{f(\mathbf{r}')}{\rho(\mathbf{r}')} W(\mathbf{r} - \mathbf{r}', h)\rho(\mathbf{r}')d\mathbf{r}' + \mathcal{O}(h^2). \tag{A.5}$$

We can now discretize this field on to a series of particles of variable mass $m = \rho(\mathbf{r}')d\mathbf{r}'$, so that the original trivial identity equation A.1 has now become:

$$f(\mathbf{r}) \approx \sum_i \frac{m_i}{\rho_i} f(\mathbf{r}_i) W(\mathbf{r} - \mathbf{r}', h). \tag{A.6}$$

Equation A.6 represents the discrete approximation of the continuous scalar field f at position $\mathbf{r}$ in the computational domain V. After discretization, $f(\mathbf{r}_i)$, m_i and $\rho_i = \rho(\mathbf{r}_i)$ are the scalar value, mass and density of the i^{th} particle, where i ranges over all particles within the smoothing kernel. We should note that mathematically, the original position $\mathbf{r}$ at which the function f is approximated during the discretization, is completely general and thus it is not restricted to particle positions, even if in practice we generally evaluate the values in the particle positions. This expression that we just derived in 6 simple steps is the bases of all SPH formalism.

]

Appendix B

Mathematical Description of Subgrid Physics in the Compass Set

The subgrid physics prescriptions we study during this work has to do with star formation, SN feedback, SN driven winds and AGN feedback. The first three are inspired by the prescription presented by Springel and Hernquist (2003), while the latter is inspired by the scheme developed by Springel et al. (2005b) and is implemented according to the prescription presented in the paper by Ragone-Figueroa et al. (2013) with some modifications. The details of these models will be explored below.

B.1 Star Formation

In our model each SPH particle samples a complete region of the ISM and has an associated density ρ. This is similar to the N-body representation of collisioneless fluids, but with an unersolved matter with a more complex structure. We picture the ISM as a fluid comprised by condensed clouds in pressure equilibrium with a hot ambient gas in thermal equilibrium with each other. Thus, whenever the denstity in one of these regions gets higher than a certain threshold ρ_{thr}, the SPH particles have the ability to become multiphase, so that their total density can be expressed in terms of a cold and a hot density fraction, $\rho = \rho_c + \rho_h$. The clouds, i.e. ρ_c, supply the material available for star formation and is decoupled form the hydrodynamic equations, while the hot phase of the keeps following them. Even if decoupled from hydrodynamic equations, cold clouds are subject to grvity and inertia. Moreover, they exchange mass and energy with the hot ambient gas. A numerical instantaneous SFR related to the cold fraction is associated to each multiphase particle:

$$\frac{d\rho_\star}{dt} = \dot{\rho}_\star = (1-\beta)\frac{\rho_c}{t_\star}, \tag{B.1}$$

where $t_\star$ is the characteristic timescale for star formation and β the fraction of massive stars that are expected to instantly explode as supernovae, which depends on the chosen

IMF (we chose the Chabrier IMF Chabrier, 2003). The timescale for star formation follows also the relation:

$$t_\star(\rho) = t_0^\star \left(\frac{\rho}{\rho_{thr}}\right)^{-1/2} \tag{B.2}$$

where $t_0^\star$ is a constant set to 1.5 Gyr in order to match the observed Kennicutt relation (Kennicutt, 1998). Combining equations B.1 and B.2 becomes obvious that this parameter is deeply related to the SFE:

$$SFE = \frac{\dot{\rho_\star}}{\rho_c} = \frac{1-\beta}{t_0^\star}\left(\frac{\rho}{\rho_{thr}}\right)^{1/2} \tag{B.3}$$

Due to the supernova feedback part of the cold clouds gets evaporated, which we can expressed through the following equation:

$$\frac{d\rho_c}{dt} = -A\beta\frac{\rho_c}{t_\star} \tag{B.4}$$

Here A is the efficiency of evaporation and depends on the local gas density as $A \sim \rho^{-\frac{4}{5}}$. This relations construct a self-regulated cycle of star formation: high density in cold clouds lead to a high SFR, that in turn means more feedback and thus cloud evaporation through heating. When clouds evaporate material is returned to the hot phase and thus the SFR decreases, as well as the stellar feedback. As a consequence of the missing feedback, the gas cools again in cold clouds, so that the cycle restarts (see Springel and Hernquist, 2003).

B.2 Supernova Driven Winds

The multiphase model for star formation summarized above leads to a self-regulated star formation cycle. However, it offers no route for baryons to climb out of galactic potential wells after having collapsed into them and thus it is not able to account for the phenomenology associated with galactic outflows observed at low (e.g. Bland-Hawthorn, 1995; Heckman et al., 2001) and high (e.g. Pettini et al., 2001; Frye et al., 2002) redshifts. Galactic outflows play a crucial role in the heating of the IGM and the enrichment of both the IGM (Aguirre et al., 2000; Aguirre et al., 2001; Aguirre et al., 2001; Madau et al., 2001) and the ICM (Scannapieco and Broadhurst, 2001; Scannapieco et al., 2001). Moreover, as they reheat the surrounding medium they are believed to reduce star formation to levels more consistent with observations. In order to extend our feedback model to account for galactic winds driven by star formation, we first assume that the galaxy disc mass-loss rate that goes into the wind is proportional to the star formation rate itself (as stated by the observational evidence presented by Martin, 1999):

$$\dot{M}_w = \eta\dot{M}_\star. \tag{B.5}$$

$\dot{M}_\star$ is the formation rate of long-lived stars and η a coefficient of the order of unity that can be tuned to control the stregth of winds in our simulation. Whether the material lost

from the disc will be able to scape the halo, will depend on several factors, namely: the velocity to which the gas is accelerated, the amount of intervening and entrained gas, and the depth of the potential well of the halo. Depending of these three factors, a wind may escape the halo and pollute a large volume or it may fall get ejected but fall back to the halo creating a galactic 'fountain'.

To calculate the velocity of the wind, we assume that the wind carries a fraction χ of the supernova energy. If we equate the wind kinetic energy with the energy input by supernovae,

$$\frac{1}{2}\dot{M}_w v_w^2 = \eta\epsilon\dot{M}_\star. \tag{B.6}$$

and solve for the wind velocity v_w, we obtain the following expression:

$$v_w = \sqrt{\frac{2\beta\chi}{\eta(1-\beta)}}. \tag{B.7}$$

which, given a value for the fraction of supernova energy χ carried by the particle, for the SFR coefficient η and for the fraction β of massive stars that are expected to instantly explode as supernovae, provides the associated wind particle velocity.

B.3 AGN Feedback

The most important changes introduced in our AGN prescription with respect to Springel et al. (2005b) and Ragone-Figueroa et al. (2013) are that we do not impose any artificial temperature threshold to define multiphase gas particles and the energy injected by AGNs is not used to evaporate the cold phase in gas particles. This implementation results in a better concordance between the galaxy stellar mass function in simulations (GSMF) and the observed one. Another difference between our model and the original one is that we differentiate between hot and cold accretion as will be further explained in the next sections.

B.3.1 BH Seeding

BHs are seeded in the position of the most bound particle, which is consider the center of each FoF group. To be seeded the target FoF groups must have a total stellar mass higher than $2.8\times10^9 M_\odot$, a stellar to DM mass ratio higher than 0.05, a gas content equal or larger to 10% of the stellar mass and no other BH inside them. The seeding mass is $5.5\times10^5 M_\odot$, which means that it is from the order of the gas and dm particles in the simulations, with the difference that the BH particle represents just one BH and not a population of them.

From a simulation point of view this poses the challenge of avoiding any displacement of the BH particle due to the force exerted by our SPH and DM particles, so that the BH remains at the center of the halo. Instead of repositioning the BH at each timestep back

to the center of the halo as suggested by Ragone-Figueroa et al. (2018), we chose to try a less aritificial prescription. We assigned the BH a large dynamical mass and low values of star and BH particles softening leghts. The BH dynamical mass is enforced to be equal to the DM particle mass until it grows beyond that value and the softening values are four times smaller than before. These numerical prescription is enough to produce a dynamical friction wihtout having to add it artificially Steinborn et al. (2016).

Even though this prescription performs overall very well, BH centering remains a major challenge, as it is for all numerical BH prescriptions. Even with the use of a dynamical mass, it can happen that a BH moves from the center of a structure, which is problematic, specially in cluster simulations, where the absence of AGN feedback at the centers of BCGs leads to catastrophic cooling and thus to too high star formation rates and masses.

B.3.2 AGN Accretion and Feedback

The growth of BH happens through two channels, BH-BH mergers and accretion of the surrounding gas. The accretion follows the formula:

$$\dot{M}_{Bondi,\alpha} = \alpha \frac{4\pi G^2 M_{BH}^2 \rho}{(c_s^2 + v_{BH}^2)^{3/2}} \tag{B.8}$$

where α is equal to 10 for hot gas ($T > 5 \times 10^5 K$) and 100 for cold gas ($T < 5 \times 10^5 K$; Steinborn et al. (2016). The velocities and the densities inside the expression are smoothed over 200 gas particles with a kernel function centered at the position of the BH. The expression of the BH feedback is as follows:

$$\dot{E} = \epsilon_r \epsilon_f \dot{M} c^2 \tag{B.9}$$

The accretion is capped by the Eddington limit, so $\dot{M}$ will be the minimum between equation A.5 and the Eddington accretion rate. ϵ_r is the fraction of energy transformed in radiation energy and ϵ_f the fraction of energy distributed and thermally coupled to the nearest 200 gas particles.

In the original version of the model the energy was used to evaporate the cold fraction of multiphase gas particles (Springel and Hernquist, 2003), but in our set up we modified this so that the feedback energy couples only to the hot phase of each gas particle, which allows for more massive galaxies as with the original implementation.

The growth of BH though BH-BH mergers may occur if the relative velocities and positions of the BH particles are small enough, $v_{rel} > 0.5 \times c_s$; $r_{rel} < 3.5 h^{-1} pkpc$, and if the differences between the gravitational potentials fulfill: $|V_{pot,rel}| + v_{rel}^2 < 0.5 \times c_s^2$.

B.3.3 AGN Feedback Calibration

In order to mimick real AGNs it is necessary to calibrate quantities like ϵ_r and ϵ_f, so that we get the right BH mass, galaxy stellar mass relations (Magorrian et al., 1998) and other observational quantities reported mainly by McConnell and Ma (2013); Gaspari et al. (2019). To mimic current observations we fix the value of $\epsilon_r = 0.07$ and $\epsilon_f < 1$ in quasar-mode. The results are shown in Figure B.1.

Simulations reproduce the correlation arising in observations. Note however, that our scatter ($\sigma = 0.2$) is noticeably lower than the scatter observed in Gaspari et al. (2019) ($\sigma = 0.4 + -0.03$). This may partly have to do with uncertainties arising in observations. Nevertheless, we should not neglect the possibility that our subgrid model adopted is not capturing all the diversity of BH accretion conditions and AGN feedback at small scales, which is another aspect to consider when adding improvements to our AGN prescription.

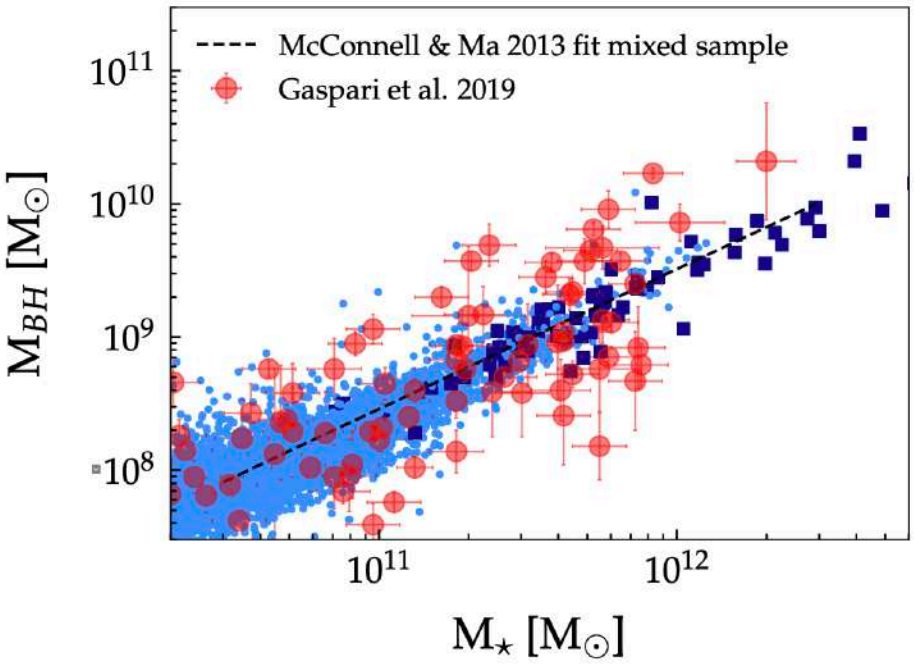

Figure B.1: Correlation between the galaxies stellar mass and its central BH taken from Bassini et al. (2020). Simulated stellar masses for satellite galaxies in the Dianoga simulation plotted as cyan points are obtained considering the star particles bound to the substructure and within 50 pkpc from the galaxy center. Stellar mass of central galaxies in Dianoga are plotted as dark-blue squares is obtained by summing over all stellar particles within an aperture of $0.15 \times R_{500}$. Observational data are taken from McConnell and Ma (2013) (dashed black line) and from Gaspari et al. (2019) (red circles).

]

Appendix C

Compass Clusters Details

Table C.1: Virial masses and radii of the most massive clusters in the Lagrangian regions of the COMPASS set at $z = 0$ and $z = 5$.

Name	$M_{vir,z=0}$ [$M_\odot/h$]	$R_{vir,z=0}$ [cMpc/h]	$M_{vir,z=5}$ [$M_\odot/h$]	$R_{vir,z=5}$ [cMpc/h]
g0016649	1.754e+15	2.5334	2.387e+12	0.36286
g0272097	1.491e+15	2.3996	2.854e+12	0.38512
g1212639	1.447e+15	2.3759	4.552e+12	0.44997
g1483463	1.366e+15	2.3304	1.828e+12	0.33194
g1657050	1.367e+15	2.3315	4.059e+12	0.43308
g1680241	1.216e+15	2.2422	1.393e+12	0.30323
g1987669	1.771e+15	2.5413	2.261e+12	0.35634
g2980844	1.886e+15	2.5952	2.448e+12	0.36592
g3327821	1.641e+15	2.4773	2.751e+12	0.38046
g3346905	1.695e+15	2.5042	6.966e+12	0.51854
g3888703	3.099e+15	3.0622	3.977e+12	0.43016
g4425770	1.629e+15	2.4718	1.715e+12	0.32500
g4606589	1.072e+15	2.1498	6.503e+12	0.50678
g4915399	1.509e+15	2.4093	1.253e+12	0.29273
g5265133	1.782e+15	2.5464	4.812e+12	0.45839
g5503149	1.409e+15	2.3546	4.857e+12	0.45980
g5699754	1.501e+15	2.3342	5.908e+12	0.49084
g6287794	1.291e+15	2.2871	4.022e+12	0.43181
g6348555	1.303e+15	2.2946	3.445e+12	0.41006
g6802296	9.997e+14	2.1002	2.459e+12	0.36647
g7263961	1.647e+15	2.4804	1.471e+12	0.30876
g7358274	1.622e+15	2.4676	4.683e+12	0.45425
g7570066	1.850e+15	2.5782	3.493e+12	0.41195
g7577931	1.507e+15	2.4081	2.076e+12	0.34637

Acknowledgments

This work would not have been possible if it wasn't for all the people that have supported me during this long journey. First, I want to thank Klaus Dolag for offering me the opportunity to work with him and his team and for his joyful spirit and his personal sense of humor. I hope I will collect many 'Witzig stämpeln' during the upcoming years! I also want to thank Rhea-Silvia Remus for her attentive supervision and her positive and dedicated spirit during this complicated year. It was a stroke of luck to find a supervisor like you.

Thanks to my colleagues at the CAST group, for being so supportive and making me feel part of the group since the first day. Special mention to Tadziu, who is always ready to help by asking the most interesting questions or by sharing some laughs. And of course, special thanks to Tirso, ¡te debo tantos pintxos que ya no se como voy a pagarlos!

Gracias Mikel por tu heroica aparición en los últimos dias de preparación de la tesis. No se como hubiese podido sobrevivir sin tus comentarios, precisos y acertados, y tu disposición a ayudar. ¡Espero que podamos celebrarlo muy pronto con unos ricos bocadillos del Juantxo en la Zurriola!

Por supuesto, no me olvido de mis amigos. Haberos encontrado es uno de los mayores regalos que me ha hecho esta vida. No tengo palabras para agradeceros todo lo que haceis por mi. Espero poder cuidaros igual de bien que me cuidais vosotros. Gracias. Os quiero.

Gracias familia por todo lo que me dais. Y especial gracias a mi tia Oliva, a mis primos Feli y Juan, y a mis primitos Jon y Mikel. Vuetsro cariño es lo que más me hace sentir en casa en este mundo. Sois parte indispensable de mi hogar.

Papá, mamá. Gracias. Vosotros sois lo que más quiero en esta vida y no estaría aquí si no fuese por vuestro sacrificio y vuestro amor. A lo largo de mi vida, espero ser capaz de compensaros todo el tiempo que mis estudios nos han robado, y sobre todo, espero que podais sentiros muy orgullosos de mi.

Y finalmente, quiero darles las gracias a mis abuelas que ya no están, pero a las que sigo recordando y queriendo con locura. Estos éxitos también son vuestros.

Declaration:

I hereby declare that this thesis is my own work, and that I have not used any sources and aids other than those stated in the thesis.

München, 02.11.2021

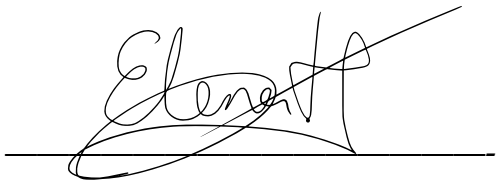

Elena Hernández Martínez